

THERMAL IMPLICATIONS OF HYDROPEAKING ACTIVITY IN
REGULATED ARCTIC RIVERS

BY

Tyler King

B.S., University of New Hampshire (2010)

THESIS

Submitted to the University of New Hampshire
in Partial Fulfillment of
the Requirements for the Degree of

Master of Science

in

Hydrology

December, 2012

This thesis has been examined and approved.

Thesis Director, J. Matthew Davis
Associate Professor of Earth Sciences and Environmental
Sciences

Anne Lightbody
Assistant Professor of Earth Sciences and Environmental
Sciences

Knut A. Alfredsen
Associate Professor Department of Hydraulic and
Environmental Engineering, NTNU

Date

DEDICATION

To Mom and Dad, whose encouragement and support have guided me to become the person that I am, and whose examples inspire me to become the person I wish to be.

ACKNOWLEDGEMENTS

A number of people have made this thesis work possible. In particular I wish to thank my advisers Knut Alfredsen and Matt Davis for seeing the potential for collaboration, and for being flexible enough to let me pursue a non-orthodox masters project: my colleagues, Roser for unmatched friendship and support, Markus for the opportunity to work in Norway: my friends Pat, Rachael, Bruno, Andrew, and Caitlin for their mental, physical, and editorial contributions to the project: and my parents without whom this would not have been possible.

Data for this project were provided by Stat Kraft, SINTEF, The Norwegian University of Science and Technology, and the Norwegian Meteorologic Institute. Field work was performed in collaboration with staff from NTNU.

This research has been made possible in part through funding provided by: The United States Department of State in the form of a Fulbright Academic Student Grant to Norway, 2010 academic year: SINTEF Energi in the form of a Student Internship, Summer 2011: and The Earth Science Department at the University of New Hampshire in the form of a Teaching Assistant Fellowship, 2011 academic year.

Table of Contents

DEDICATION	iii
ACKNOWLEDGEMENTS	iv
LIST OF TABLES	viii
LIST OF FIGURES	xi
LIST OF SYMBOLS	xii
ABSTRACT	xiii
1 BACKGROUND	1
1.1 Norwegian Wind Power and Hydropower	1
1.2 Potential Thermal Impacts of Future Wind Power Development	3
1.2.1 Description of Hydropeaking and Thermopeaking	5
1.2.2 Description of Seasonal Shift	6
1.3 Importance of River Temperature	7
1.4 Current Thermopeaking Conditions	8
1.5 Thesis Objective	9
1.5.1 Observing Current Thermopeaking	9
1.5.2 Construction of Hydropeaking and Thermopeaking Models	9
1.5.3 Modelling Thermal Impacts of Future Discharge Scenarios	10
2 METHODS	11
2.1 Site Description	11
2.1.1 Nea-Nidelva Watershed	11
2.1.2 Nidelva River	11
2.1.3 Study Reach	14
2.2 Data Collection	19
2.2.1 Bathymetric Data	19
2.2.2 Discharge Data	21

2.2.3	Temperature Data	22
2.2.4	Meteorological Data	24
2.3	Peaking Identification	26
2.3.1	Identification of Hydropeaking Events	26
2.3.2	Identification of Thermopeaking Events	30
2.4	Model Construction	30
2.4.1	Hydrodynamic Model	30
2.4.2	Energy Balance Model	34
2.4.3	Parameter Sensitivity	39
2.4.4	Salmon Growth Modelling	40
2.4.5	Ice Development Potential	42
2.5	Modelling Impacts of Future Discharge Scenarios	42
2.5.1	Generating Discharge Records	43
2.5.2	Generating Temperature Records	46
2.6	Simulating a Deepwater Intake	50
3	RESULTS	52
3.1	Observed Conditions	52
3.1.1	Observations of Hydropeaking	52
3.1.2	Observations of Thermopeaking	55
3.2	HEC-RAS Model Development	60
3.2.1	Hydrodynamic Calibration	60
3.2.2	Energy Balance Calibration	64
3.2.3	HEC-RAS Model Verification	66
3.2.4	Parameter Sensitivity	68
3.3	Transport of Thermopeaks	69
3.4	Future Discharge Scenarios	71
3.4.1	HEC-RAS Model Results	71
3.4.2	Potential Impacts	73
3.5	Simulating a Deepwater Intake	76

3.5.1	Crisp Model Results: Deepwater	79
3.5.2	Ice Formation Potential: Deepwater	80
4	CONCLUSION	82
4.1	Observations of Hydropeaking and Thermopeaking	82
4.2	Modeling Thermopeaking	82
4.3	Influence of Discharge Scenarios	83
4.3.1	Potential Biological Impacts	83
4.3.2	Potential Ice Formation Impacts	84
4.4	Influence of Intake Depth	84
4.4.1	Deepwater: Potential Biological Impacts	85
4.4.2	Deepwater: Potential Ice Development	86
4.5	Recommendations	86
	LIST OF REFERENCES	88
A	APPENDIX	93
A.1	Heat Flux Equations: Adapted from Brunner (2010)	93
A.1.1	Solar Radiation	93
A.1.2	Atmospheric Longwave Radiation	93
A.1.3	Back Longwave Radiation	94
A.1.4	Sensible Heat	94
A.1.5	Latent Heat	94
A.1.6	Wind Function	95
A.2	Representative Heat Fluxes	96
A.3	Observed Meteorologic Parameters	98
A.4	Cross Sections	98

List of Tables

2.1	Discharge Ranges at Rathe	17
2.2	Extent of Temperature Data Collection	23
2.3	Energy Balance Model Parameters	38
2.4	Crisp Model Parameters	41
3.1	Seasonality of Hydropeaking Potency	58
3.2	Roughness Scaling	62
3.3	Energy Balance Model Parameters	64
3.4	Model Residuals	64
3.5	Relative Parameter Sensitivity	68
3.6	Crisp Model Results	74
3.7	Ice Formation Potential	76
3.8	Crisp Model Results: Deepwater Scenario	79
3.9	Ice Formation Potential: Deepwater Scenario	81

List of Figures

1-1	Map of Norwegian Hydro and Wind Power Facilities	2
1-2	Norwegian Reservoir Storage Levels	3
1-3	Power Transmission System: Northern Europe	4
1-4	Pathways for Species Elimination	6
1-5	Thermopeaking Mitigation Techniques	8
2-1	Map of Nea-Nidelva Watershed	12
2-2	Map of River Nidelva	13
2-3	Schematic of Study Region	14
2-4	Map of Study Reach	16
2-5	Histogram of Annual Discharge at Rathe Gauge	17
2-6	Representative Hydropeaking Schedule	18
2-7	Map of Model Cross Sections	20
2-8	Cross Section Temperatures at Rathe	23
2-9	Temperature Profile: Selbusjøen Reservoir	25
2-10	Observed Meteorologic Data	26
2-11	Distribution of Discharge Deviations: Bratsberg and Bypass	28
2-12	Histogram of Observed Discharge Deviations: Rathe Gage	28
2-13	Hydrograph of Rathe and Bratsberg: May 2011	29
2-14	Hydrograph of Rathe and Bratsberg: August 2011	29
2-15	Map of Local Surficial Geology	31
2-16	Open Channel Flow Headloss Diagram	32
2-17	Potential Wind Power Production	43
2-18	Simulated Discharge	45
2-19	Calculated Reservoir Temperature	47
2-20	Calculated Bypass Temperature	48

2-21 Recreated Temperature Boundary Condition	48
2-22 Recreated Temperature: Bratsberg	49
2-23 Recreated Temperature: Headwater	49
2-24 Recreated Temperature: Rathe	50
2-25 Scatterplot of Rathe Recreated Temperatures	50
3-1 Observed Discharge and Temperature	53
3-2 Discharge at Bratsberg and Rathe	53
3-3 Discharge Histogram	54
3-4 Price and Discharge: November	54
3-5 Price and Discharge: May	54
3-6 Histogram of Bratsberg Hydropeaking Amplitudes	56
3-7 Distribution of Hydropeaks Throughout the Day	56
3-8 Histogram of Temperature Responses to Hydropeaks	57
3-9 Seasonal Histogram of Temperature Responses to Hydropeaks	57
3-10 Seasonal Thermopeaking	59
3-11 Histogram of Observed Temperatures	59
3-12 Calibrated Waterlines	60
3-13 Scatterplot of Observed and Modeled Water Levels	61
3-14 Manning Roughness	62
3-15 Map of Manning Roughness Coefficients	63
3-16 Calibration Results	65
3-17 Temperature Calibration Scatter Plot	65
3-18 Model Residuals: Calibration	66
3-19 Verification Results	67
3-20 Temperature Verification Scatter Plot	67
3-21 Model Residuals: Calibration	68
3-22 Energy Balance Parameter Sensitivities	69
3-23 Calibrated Model Results	70
3-24 Futures Scenarios: Modeled River Temperatures	72

3-25	Future Scenarios: Alteration in River Temperature	73
3-26	Crisp Model Results	74
3-27	Deepwater Intake Simulation Results	77
3-28	Thermal Impact of Deepwater Intake	78
3-29	Deepwater Intake Future Scenarios: Alteration in River Temperature	78
3-30	Crisp Model Results: Deepwater Scenario	79
A-1	Heat Flux Constituents	97
A-2	Meteorologic Duration Curves	99
A-3	Average Monthly Meteorologic Data	100
A-4	HEC-RAS Cross Sections	103

List of Symbols

α	Velocity weighting coefficient
α_{us}	Local Peclet number
a_t	Atmospheric attenuation
A	Cross-sectional area
A_s	Surface area of water quality cell
C_l	Percent cloud cover
C_p	Specific heat capacity
C_{us}	Local Courant number
D	Crisp salmon development degree index
e	Vapor pressure
ϵ	Emissivity
g	Gravitational constant
Γ	Dispersion coefficient
h_e	Energy head loss
K_h/K_w	Diffusivity ratio
L	Discharge weighted reach length
L_{vap}	Latent heat of vaporization
P_{atm}	Atmospheric pressure
ρ	Density
ϕ	Temperature per unit volume
ϕ^*	QUICKEST temperature per unit volume
$\frac{\delta\phi}{\delta t}SS$	Cell energy budget terms
Q	Volumetric discharge
q	Heat flux at air/water interface
R_m	Richardson multiplier
R_ω	Reflectivity of water
\bar{S}_f	Friction slope
\bar{S}_r	Average relative sensitivity
σ	Stephan Boltzman constant
t	Time
T	Temperature
θ	Latitude
u	Wind speed
u^*	Friction velocity
V	Cross-section averaged water velocity
\forall	Volume of water quality cell
w	Average channel width
x	Stream-wise length
Y	Water depth
Z	Elevation

ABSTRACT

THERMAL IMPLICATIONS OF HYDROPEAKING ACTIVITY IN REGULATED
ARCTIC RIVERS

by

Tyler King
University of New Hampshire, December, 2012

River temperature is an influential variable for biologic activity in arctic rivers. Regulated discharge regimes can have significant impacts on water temperature on both short and long time scales as water discharged through subterranean power stations is often a significantly different temperature than water flowing in the bypass reach. As a result, river temperatures downstream of a hydropower station's discharge point are influenced by the power station's electric production schedule and the relative temperatures of bypass flows. The discharge strategies for the Norwegian hydropower network are likely to shift in the future, as wind power potential is harnessed in northern Europe. A seasonal shift in hydropower production could, in turn, affect aquatic ecology through thermal alteration. This work aims to investigate the current effects of regulated discharge on river temperature in Norway and to estimate the influences that alterations in discharge patterns would have on river temperature in the future.

CHAPTER 1

BACKGROUND

1.1 Norwegian Wind Power and Hydropower

Norway is world renowned for producing over 99% of the nation's electricity consumption through hydropower. Over 60% of the nation's potential hydropower resources have been developed into 128 terawatt-hours (TWh) of annual power production through a system with 30,000 megawatts of installed capacity. The remaining 40% of Norwegian hydropower production potential is held in national protection or falls outside the range of economically feasible development. In comparison, the United States, a nation with over 60 times the population of Norway, has developed less than 20% of available hydropower resources, producing 282 TWh of hydropower in 2008. Norwegian hydropower development is an astounding feat, with extensive networks of high mountain reservoirs, tunnels, and subterranean powerhouses that blanket the mountainous landscape (Figure 1-1). This leader in renewable energy presses forward to also develop formerly untapped windpower resources and rethink the very nature of hydropower. The impetus for these developments lies in the increasing connectivity with continental Europe through sub-sea powerlines, development of off-shore wind projects, and an increasing deregulation of the European energy market.

Windpower has been identified as the most feasible renewable energy source for Northern Europe, and development is under way to realize the 126,000 megawatts of development expected by 2030 (Jan De Decker, 2011). Windpower alone, however, will not be sufficient as production from wind farms relies on fluctuating environmental conditions to produce electricity and, as such, will produce power on a schedule that bears no reflection of energy demand. A linking of wind and water power is commonly proposed, where hydropower reservoirs are used as large batteries, being "charged" through pump storage and "drained" via discharge during periods of high and low windpower production respectively. This act of balancing production and demand is feasible as electricity prices fluctuate greatly hourly,



Figure 1-1: Left: Developed hydropower stations. Middle: Developed wind power sites. Right: Proposed wind power sites. Image source: NVE Atlas www.altas.nve.no

with excess energy production driving prices down and insufficient production driving electricity prices up. When there is excess energy production from wind farms, the price of electricity is expected to drop, making it feasible for hydropower plants to reverse production by purchasing electricity to pump water back into higher reservoirs (Holland and Mansur, 2008). Some hydropower production stations are able to convert production turbines into pumps by running them in reverse, while other pump storage facilities utilize a dedicated system of pumps for this task (Ramos and Borga, 1999; Anagnostopoulos and Papantonis, 2007). The hydropower sector is well suited for the role of balancing energy production, as output can be altered quickly, unlike its thermal counterparts such as coal or nuclear (Locher, 2004). There is, however, not enough storage capacity in continental Europe to accommodate the volume of water required to realize full energy storage from the development of Northern Europe’s massive wind power potential (Leonhard and Grobe, 2004). This is where Norway comes into the picture. With a nation covered with reservoirs (84.3 terawatt hours total reservoir capacity), Norway has the potential to act as Europe’s “Green Battery” through conversion of its hydropower reservoirs to pump storage facilities. A majority of Norwegian hydropower systems utilize reservoir storage where spring meltwater is stored for energy production later in the year. However, these reservoirs can dry out seasonally, indicating that there is capacity to store water through pump storage (Figure 1-2). The Norwegian government is acting on this potential with investment in both on-

and offshore windpower projects (Figure 1-1) as well as investigations into the feasibility of pump storage conversion. The power transmission system is already in place, with energy being traded intra- and internationally (Figure 1-3). If these developments comes to fruition, Norway could easily see a dramatic increase in its hydropower production, no small feat for a nation that has already developed its hydropower to conventional capacity.

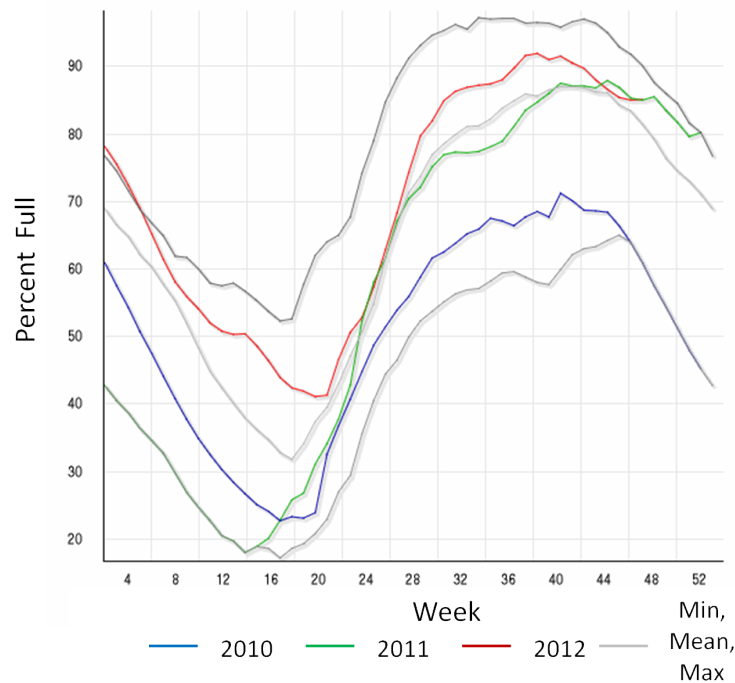


Figure 1-2: Storage levels in Norwegian reservoirs. Minimum, Mean, and Maximum values: 1990-2007. Image source: StatNett.no

1.2 Potential Thermal Impacts of Future Wind Power Development

There are two specific pathways through which wind power development may impact river temperature. The first is in the increased incidence of hydropeaking events, while the second is in the seasonal displacement of reservoir discharge.

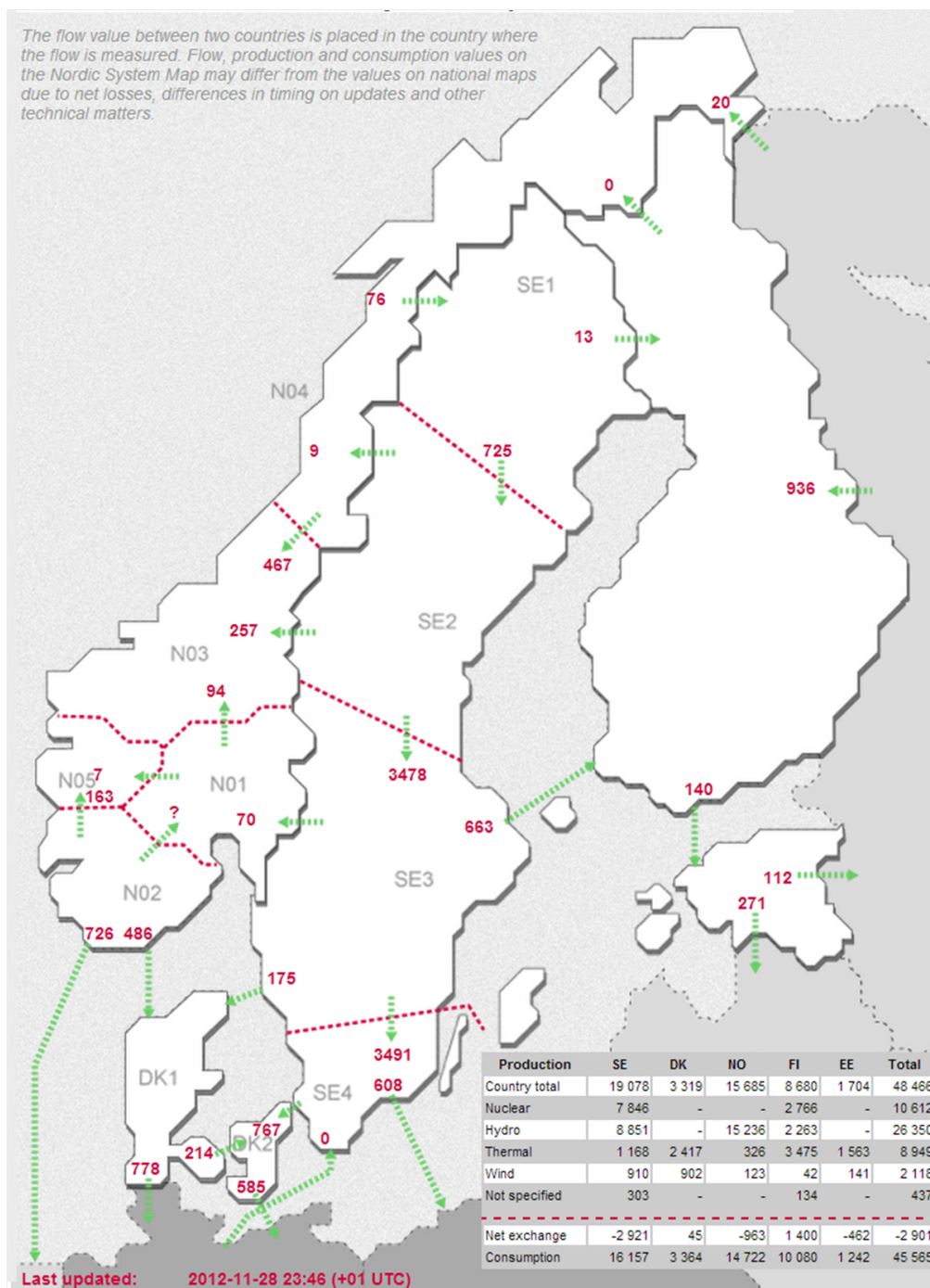


Figure 1-3: Map of power fluxes between electricity market areas. Data valid for 28-11-2012 23:46 +01 UTC (Universal Coordinated Time). Power transfers in megawatts (MW) shown in red. Image Source: StatNett.no

1.2.1 Description of Hydropeaking and Thermopeaking

Hydropeaking is a term to describe rapid changes in discharge through hydropower facilities and often occurs as hydropower is used to balance the energy markets with short term releases of water from reservoirs at times of high electricity cost and reduced discharge when prices fall. It is usually applied with the intent of minimizing excess production to keep reservoirs as full as possible, waiting for periods of high energy price to release water, thus maximizing profits. Reaches of rivers located downstream of hydropower plant outlets are subjected to rapid changes in stage and discharge when there is an alteration in facility operation. The environmental impacts of hydropeaking in Norwegian rivers have come under investigation as energy markets deregulate, the European grid becomes ever more connected, and the incidence of hydropeaking increases. Hydropeaking can directly and indirectly reduce the abundance, diversity, and productivity of riverine organisms (Cushman, 1985). There is a large body of literature focusing on the biological implications of hydropeaking, including habitat availability (Petts and Gurnell, 2005; Richmond and Perkins, 2009; Valentin et al., 1996; Vehanen et al., 2000), fish stranding (Bradford, 1997; Hunter, 1992; Higgins, 1996; Casas-Mulet et al., 2010; Bunt et al., 1999; Berland et al., 2004) and thermal modification (Coutant, 1999; Sherman, 2000).

Thermopeaking, the unnaturally rapid alteration in river temperature as a result of reservoir releases, is used to describe the thermal impact of hydropeaking. Tailwater from reservoir-fed hydropower stations often exhibit unseasonal temperatures, leading Ward and Stanford (1979) to identify numerous pathways for negative metabolic impacts on aquatic ecosystems downstream from reservoirs with deep water intakes (Figure 1-4). The term “thermopeaking” has a similar connotation as hydropeaking, in that it is an alteration of greater magnitude and rate than is seen naturally (Higgins, 1996; Hunter, 1992).

The implications of thermopeaking have not received as much attention as other effects from hydropeaking, even though hydropeaking is known to affect river temperature and river temperature is known to affect ecosystem productivity (Carolli et al., 2012). A majority of the work that has been done on thermopeaking focuses on physical description and modelling of thermopeaking events (see e.g. Siviglia and Toro (2009); Steel and Lange

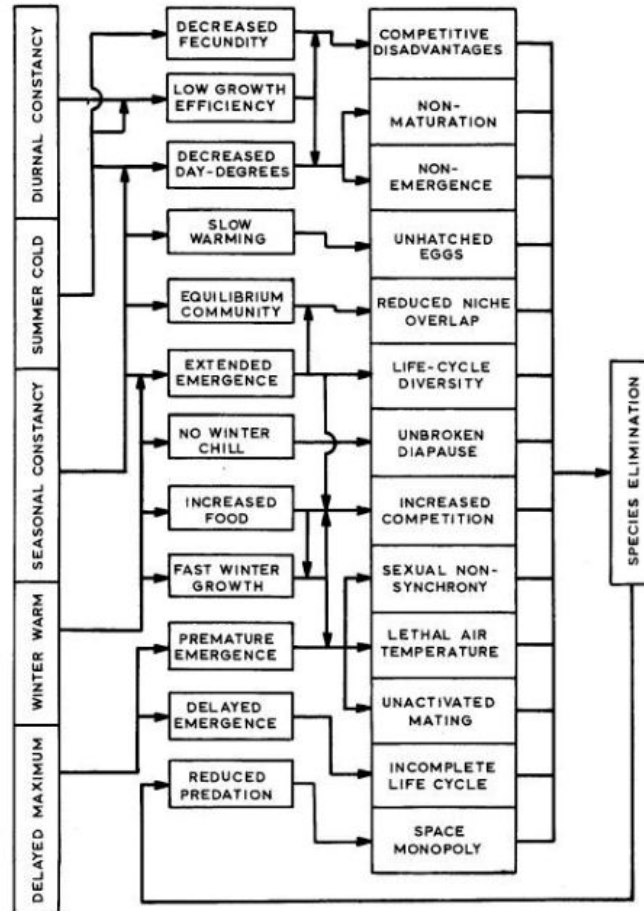


Figure 1-4: Pathways of zoobenthic species selective elimination as a result of thermal modification below deep-release dams. Adapted from Ward and Stanford (1979).

(2007); Toffolon et al. (2010), and Zolezzi et al. (2011)), and on thermopeak effects on benthic invertebrate drift (see e.g. Cristina Bruno et al. (2010); Bruno et al. (2012); Carolli et al. (2012)) while there is a noticeable lack of research on the physiological impacts for rapid temperature change on biotic health or development.

1.2.2 Description of Seasonal Shift

Hydropower production decisions are optimized for profit based on the price of electricity, which is in turn a reflection of consumer demand and power currently available on the grid. In northern Europe, the current system produces the highest energy prices in the

wintertime, as reservoirs are depleted and energy demands rise. There is currently a large incentive for hydropower operators to produce during the winter, provided that they have the capacity to do so, while there is less incentive to produce hydropower in the summer months due to lower energy consumption and lower prices. This dynamic may shift in the future, as wind production comes online and produces power more during the winter than the summer. The optimization of hydropower operation may experience a seasonal shift that will result in a focus to produce electricity from hydropower in the summer, rather than in the winter. There are potential thermal implications of this seasonal shift, as discharge from reservoirs tends to warm rivers in the winter, and cool them in the summer. One possibility would be for the system to become colder overall.

1.3 Importance of River Temperature

Water temperature is intrinsically connected to every facet of biotic health in river systems. A great deal of research has been conducted to identify water temperature as a primary factor in the presence, productivity, and metabolism of riverine micro-organisms, invertebrates, and fish populations through its influence on dissolved oxygen and metabolic processes (Armstrong et al., 2003; Caissie, 2006; Carpenter et al., 1992; Neuheimer, 2007; Schlosser et al., 2000; Vinson, 2001; Ward and Stanford, 1979). The health of all organisms are dependent on temperature ranges dictated by species, life-stage, and season and deviations from these ranges can disrupt life cycles, create ecosystem imbalance and, eventually, collapse (Coutant, 1999; Ward and Stanford, 1979). The sensitive relationship between temperature and biological processes has led to increased research into how human activities influence river temperature as well as the increased practice of including river temperature in determining environmentally sound flows (Hannah et al., 2008; Olden and Naiman, 2010). Sherman (2000) compiled a series of methods to mitigate the impacts of regulated flow has on river temperature (Figure 1-5).

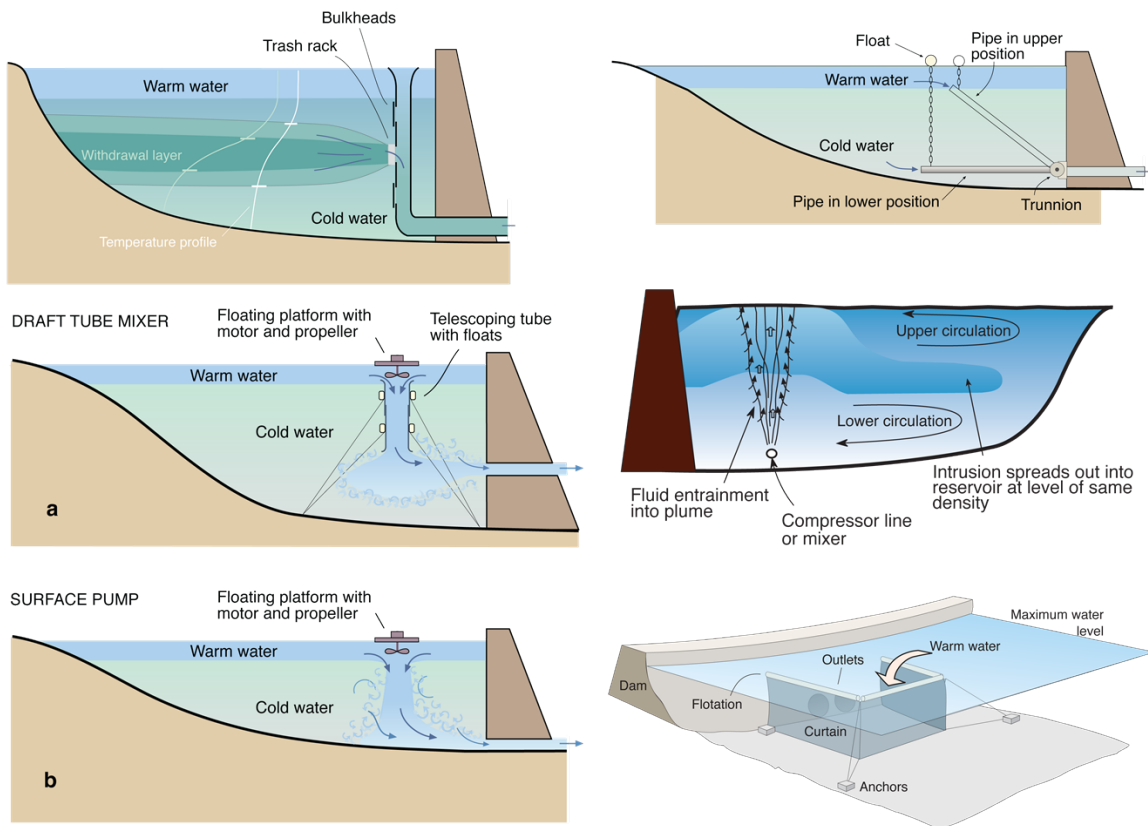


Figure 1-5: Intake variations designed to mitigate thermopeaking and other temperature pollution. Reprinted with permission from Sherman (2000)

1.4 Current Thermopeaking Conditions

Hydropeaking is utilized by hydropower operators in several regulated rivers in Norway and the practice is anticipated to increase in frequency, severity, and pervasiveness as electricity infrastructure is developed, sustainable energy requirements are imposed, and the European energy market deregulates (Killingtveit, 2012). Hydropower will be used to augment meteorologically dependent renewable energy sources, such as wind power stations, leading to a shift in thermopeaking frequency and severity.

There is significant research into the relationship between hydropower operation and river temperature in the Pacific Northwestern U.S. (Coutant, 1999; McCullough, 1999) and in the alpine rivers of Italy and Switzerland (Bruno et al., 2012; Carolli et al., 2012; Frutiger, 2004; Siviglia and Toro, 2009; Toffolon et al., 2010; Zolezzi et al., 2011). While Norway has a highly developed hydropower sector, comprised of deep water intakes, and

exhibiting hydropeaking behavior, there have been no reported studies on thermopeaking in Norwegian rivers. The biota that reside in Norwegian rivers are known to be susceptible to the impacts of thermopeaking (Berland et al., 2004; Bunt et al., 1999; Hvidsten, 1985; Scruton et al., 2008) suggesting that anthropogenic hydropeaking activity in Norway may have impacts on riverine biotic health.

1.5 Thesis Objective

The work presented here has three main focal points, all centered on Norwegian river temperature:

- Observe and document temperature response to hydropeaking activity under current discharge regimes
- Construct and calibrate hydropeaking and thermopeaking models
- Model impacts future discharge scenarios will have on river temperature

1.5.1 Observing Current Thermopeaking

Observations documented in this thesis are the first accounts of thermopeaking in a Norwegian river. These observations are used to evaluate the need for further research. By observing thermopeaking activity in a biologically productive river in mid-Norway, these observations will provide some insight into physiologically significant thresholds for thermopeaking.

1.5.2 Construction of Hydropeaking and Thermopeaking Models

In systems with long reaches downstream of the hydropeaked power plant discharge, the advection, dispersion, and diffusion of thermopeaks may be substantial, giving rise to the need to model the downstream transport of thermopeaks. The methods developed in this thesis are designed to provide examples of how hydropeaking and thermopeaking can be modeled in Norwegian systems.

1.5.3 Modelling Thermal Impacts of Future Discharge Scenarios

Hydropeaking and thermopeaking are likely to change as hydropower production schemes are altered to accommodate meteorological-dependent renewable energy sources. Modifications in frequency and duration of power hydropeaking events are modeled, as well as seasonal shifts in hydropower production. In an attempt to provide some significance to these model results the relative potential for ice development in the winter and juvenile fish development through the spring are estimated for the various potential discharge scenarios.

CHAPTER 2

METHODS

2.1 Site Description

In this section, the study site is described at the watershed, river, and reach scale.

2.1.1 Nea-Nidelva Watershed

The Nea-Nidelva watershed, shown in Figure 2-1, lies in Sør-Trøndelag commune in central Norway (circa 63° North). It is a 3,118 km² watershed with an annual run-off of approximately 2.9 billion cubic meters (average discharge of approximately 91 cubic meters per second, m³/sec). The drainage extends from the fjord-side city of Trondheim eastward to the Swedish border and includes a series of seventeen hydropower production units producing an annual average of 2,550 GWh in electricity market “NO3” in Figure 1-3 (Trondheim Energiverk, 2001). The 58 square-kilometer Selbusjøen Reservoir is the final reservoir in the ladder of hydropower production facilities in the Nea-Nidelva watershed, and is also the transition point between the two rivers with the Nea flowing in from the east, and Nidelva flow out to the north-west. Selbusjøen is the largest lake in Sør-Trøndelag commune and is the 17th largest lake in Norway.

2.1.2 Nidelva River

The River Nidelva, shown in Figure 2-2, drains the Selbusjøen reservoir in the lower extent of the Nea-Nidelva watershed. The River Nidelva was chosen as the subject of this study because it has the typical pairing of bypass and tunneled pathways leading to a discharge reach; the hydropower production is known to be currently hydropeaked; the receiving reach produces a significant amount of salmon (4-10 tons annually); and there are numerous stakeholders in the forms of recreational fishermen, paddle sport enthusiasts, the local

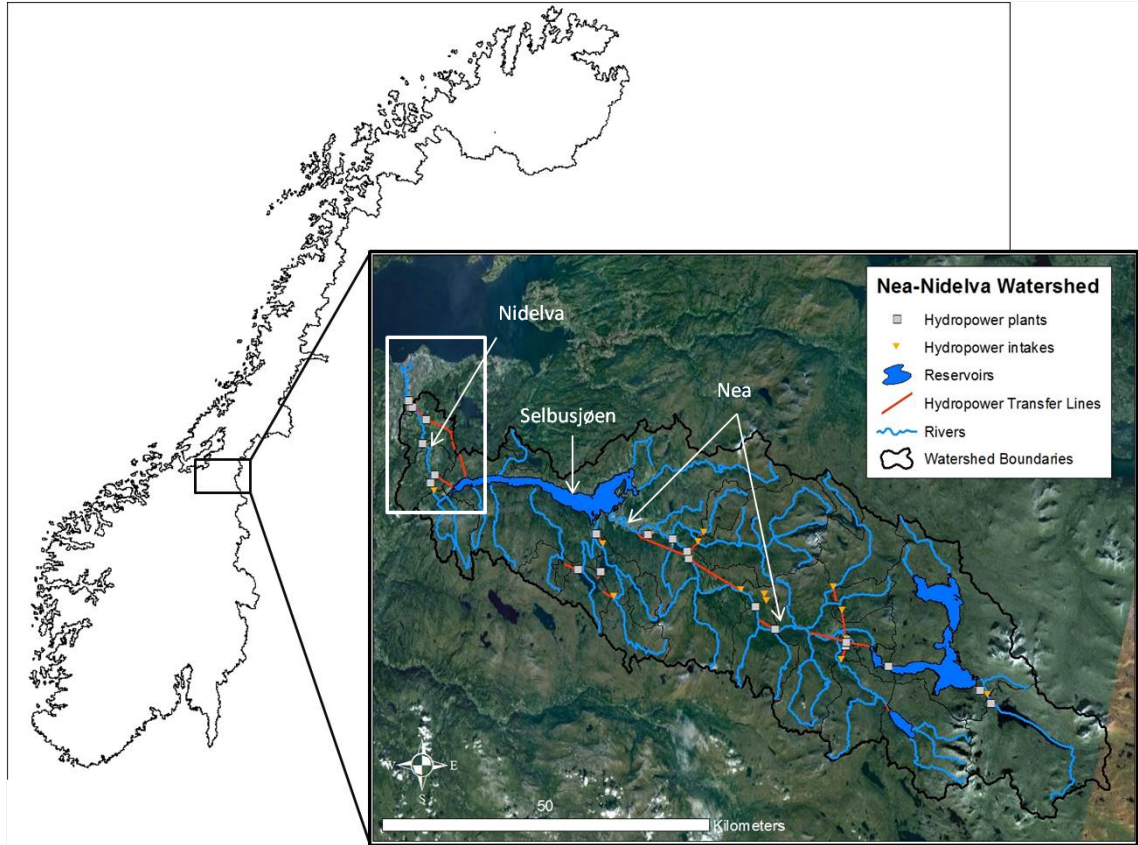


Figure 2-1: Overview of the Nea-Nidelva watershed showing tunnels, hydropower plants, reservoirs, and rivers. Note that the white box refers to the extent of Figure 2-2.

hydropower company, and the 180,000 inhabitants of Trondheim (Fremstad and Thingstad, 2007).

Water that flows down the bypass reach from Selbusjøen encounters a series of hydropower stations (Figure 2-2). The final series of these short intake run-of-river type hydropower facilities, located just upstream of the study reach, are developed around two natural water falls: Øvre- and Nedre-Leirfossene. Each waterfall has an associated dam, intake, penstock, and above ground power plant. In addition, a newer subterranean station spans both dams taking water from above Øvre Leirfoss directly to the bottom of Nedre Leirfoss (Figure 2-3). The three power stations and bypass reach comprise an area termed the Leirfoss complex in this work. There are a few pathways for water to pass through the Leirfoss complex. At the upstream end of the Leirfoss complex, water is channeled into the intake for Øvre Leirfoss powerstaion, into the intake for Leirfossene, or over the Øvre



Figure 2-2: Map of the River Nidelva, flowing from Selbusjøen reservoir to Trondheimsfjord. The bypass (red) and tunneled (black) pathways feed into the receiving reach (blue). Note that the tunnel from Jonsvatnet to Bratsberg is not in use.

Leirfoss dam. At Nedre Leirfoss, water either flows over the dam or is directed into the intake for Nedre Leirfoss powerstation. Just downstream of the dam at Nedre Leirfoss, the

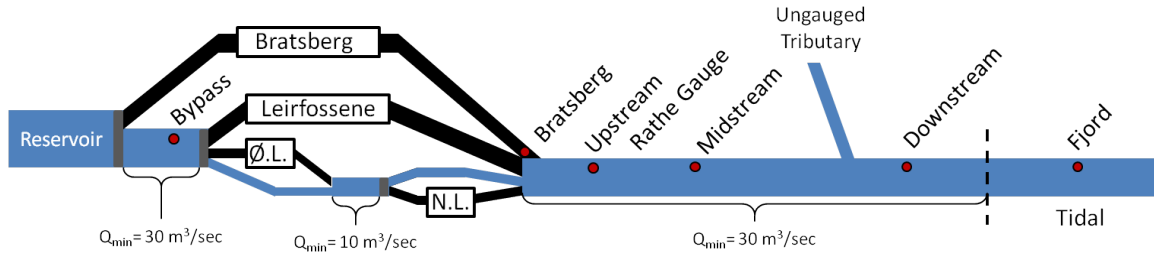


Figure 2-3: Schematic of study region from Selbusjøen reservoir to the Trondheims Fjord. Black lines represent tunnels, blue lines are surface flow. The Bratsberg, Leirfossene, Øvre-Leirfoss (Ø.L.), and Nedre-Leirfoss hydropower plants are represented as white boxes. Red dots represent temperature loggers. Minimum flow requirements are listed for the various reaches. Dams are represented with grey lines. Schematic is not to scale.

discharges from Leirfossene, Nedre-Leirfoss, and Bratsberg power stations join any flow over the Nedre Leirfoss dam and enter the upstream boundary of the study reach.

There are various minimum flow requirements in the river Nidelva: $30 \text{ m}^3/\text{s}$ from Selbusjøen to the Lierfoss complex, $10 \text{ m}^3/\text{sec}$ between Øvre-Leirfossen and Nedre-Leirfossen, and $30 \text{ m}^3/\text{sec}$ in the study reach downstream of the Leirfossen and Bratsberg outlets (Fremstad and Thingstad, 2007).

2.1.3 Study Reach

The work in this thesis is applied to the 10 kilometers of the river from the confluence of the lowermost hydroelectric powerplant outlets and the bypass reach to the mouth of the river in the Trondheimsfjord (Figure 2-4). The river bottom elevation ranges from 9.46 meters below sea level at the mouth of the river (downstream boundary) to 8.27 meters above sea level at the discharge of the Bratsberg and Leirfoss hydroelectric power plants (upstream boundary). This rise occurs over 10.26 river kilometers, producing an average slope of 0.017. There are two sections in the study reach that experience super critical flow with rapids being produced, even at minimum flow of $40 \text{ m}^3/\text{sec}$. The legal minimum flow requirement of $30 \text{ m}^3/\text{sec}$, however, discharge did not drop below $40 \text{ m}^3/\text{sec}$ for the duration of the study. The study reach is characterized by open channel flow with average surface widths of 83 and 89 meters and average depths of 2.7 and 2.9 meters at low ($40 \text{ m}^3/\text{sec}$) and high ($140 \text{ m}^3/\text{sec}$) flows respectively. The banks of the river are vegetated with

mature deciduous trees and leafed shrubbery on sloping banks for the top 6 river kilometers, followed by a section of bare sloping banks approximately two river kilometers long, and ending with the final two river kilometers flowing through the city of Trondheim in highly channelized cross sections with banks consisting of building foundations, and metal sheet-pilings. Bank shading is not considered to have significant impacts on the energy balance of the study reach as the river is wide, and the axis has a north-south orientation (Webb et al., 2008).

Water entering the study reach arrives from the Selbusjøen reservoir by one of two pathways: as direct flow through the Bratsberg hydroelectric power plant (16 kilometers of tunnel) or as surface flow along an 18 kilometer long bypass reach (Figure 2-3). The upstream boundary of the study reach is located at the confluence of these two pathways.

The Bratsberg subterranean hydroelectric power plant, drawing water from the Selbusjøen reservoir, makes use of two identical turbines, each with an operational discharge of 40-50 m³/sec while the new Leirfossene hydroelectric power plant has two turbines with discharge ranges of 30-40 m³/sec. The production ranges for these two hydropower plants produces discrete discharge ranges based on the power production mix and Table 2.1 indicates the expected discharge at Rathe for various production levels from the various turbines. These discharge thresholds have been observed with some deviation, showing the impact of meteorological variation (Figure 2-5). The minimum flow requirements downstream of Rathe are met with flow over Nedre Leirfoss, and through Lierfossene and Nedre-Leirfoss power plants. The minimum flow requirements above the Leirfoss complex is met with instream flow. This discharge contributes to the flow in the study reach. Bratsberg can be operated as a peaking facility, draining Selbusjøen only when power prices are high. Discharge through Bratsberg is not necessary for minimum flow requirements in the study reach and anytime Bratsberg is in operation the flow in the study reach is above minimum flow requirements.

The hydroelectric power production system feeding directly into the study reach is hydropeaked, with rapid alteration to the discharge mixture to meet the demands of the energy market. This generally produces elevated discharge for the entire day on weekdays, with peaks around 09:00 and 20:00 that last a few hours. Flows on weekends tend to rise

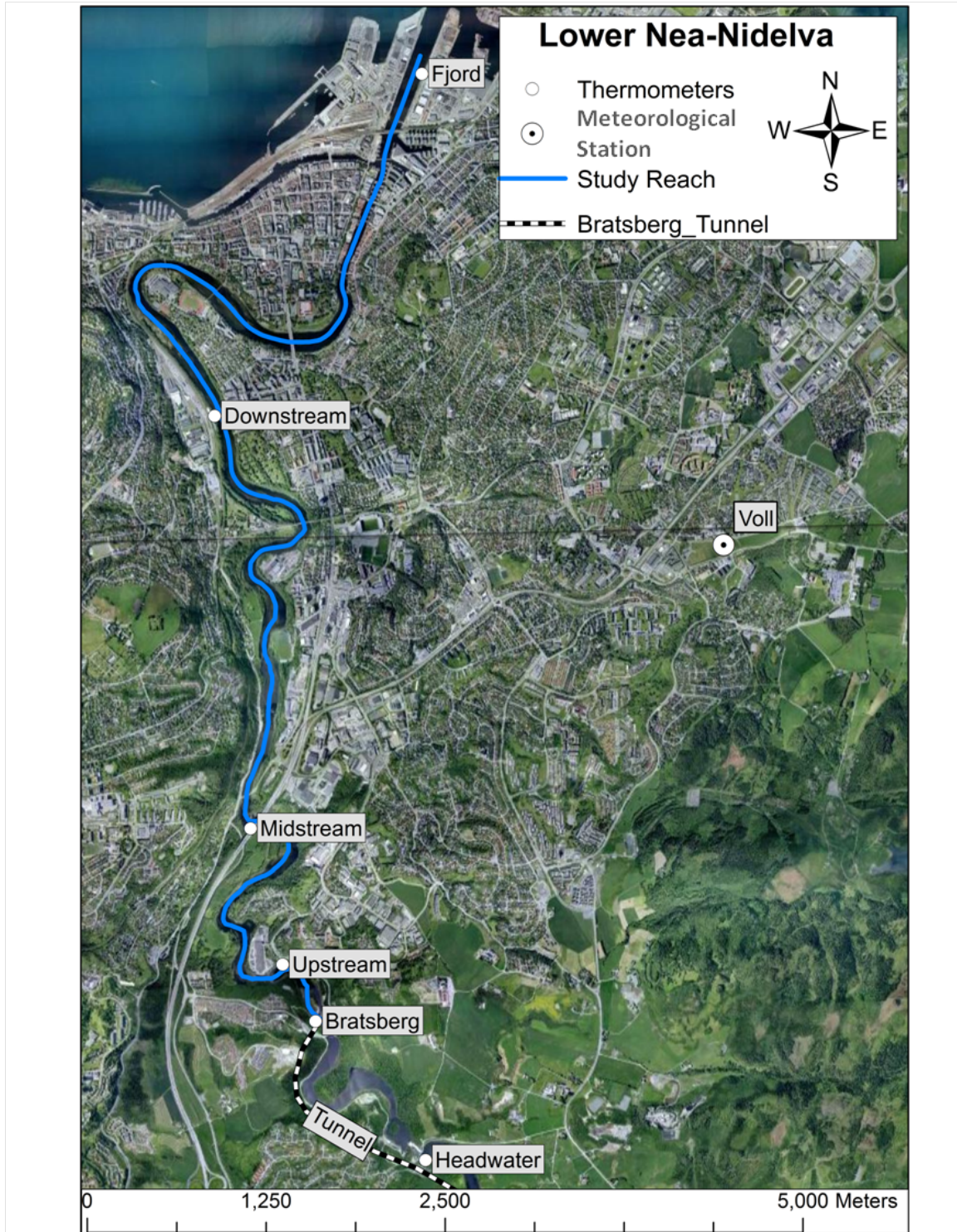


Figure 2-4: Ten kilometer long study reach of lower Nidelva from the outlets of Nedre-Leirfoss, Leirfossene, and Bratsberg power stations to the mouth of Trondheims Fjord.

Table 2.1: Discharge ranges produced from various hydroelectric power production mixtures and the corresponding hydropeaking ratio that would occur when discharge varies from minimum flow to the proposed mixture.

Mix #	Bypass Leirfossene m ³ /sec	Bratsberg 1 m ³ /sec	Bratsberg 2 m ³ /sec	Leirfossene 1 m ³ /sec	Leirfossene 2 m ³ /sec	Rathe m ³ /sec	Peaking Ratio
0	30	0	0	0	0	30	-
1	10	0	0	30-40	0	40-50	-
2	10	40-50	0	30-40	0	70-90	1.75-2.25
3	10	40-50	0	30-40	30-40	100-130	2.5-3.25
4	10	40-50	40-50	30-40	0	110-140	2.75-3.5
5	10	40-50	40-50	30-40	30-40	140-180	3.5-4.5

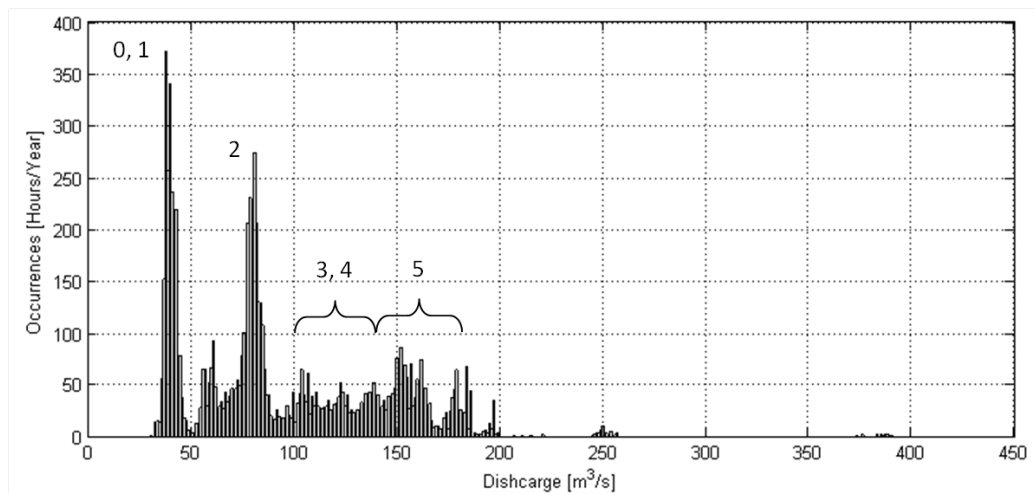


Figure 2-5: Distribution of discharge in Nidelva as measured at the Rathe gauge for the 2010 hydrologic year. Labels correspond with discharge mixes presented in Table 2.1.

above minimum flow only to meet peak demand around 12:00 and 20:00 Figure 2-6. With the given arrangement of turbines, maximum productive hydropeaking would exist when going from full stop at minimum flow to full production on all four turbines resulting in a jump from 40 m³/sec to 180 m³/sec, producing a hydropeaking ratio (discharge before divided by discharge after change) of 4.5:1. The maximum hydropeaking ratio within the observation period of this study (October 2010 through October 2011) was 4:1 and occurred on the 23rd of September 2010.

The study reach is a spawning ground for Atlantic salmon (*Salmo salar*) and seatrout (*Cynoscion nebulosus*): two species known to be sensitive to alterations in river temperature (Johnsen et al., 2010; Hvidsten, 1985; Berland et al., 2004), and also of great importance to the local community (Fremstad and Thingstad, 2007). Salmon fishing has a long history in Nidelva, with the first accounts of fly fishing in Norway emanating from this river in 1820,

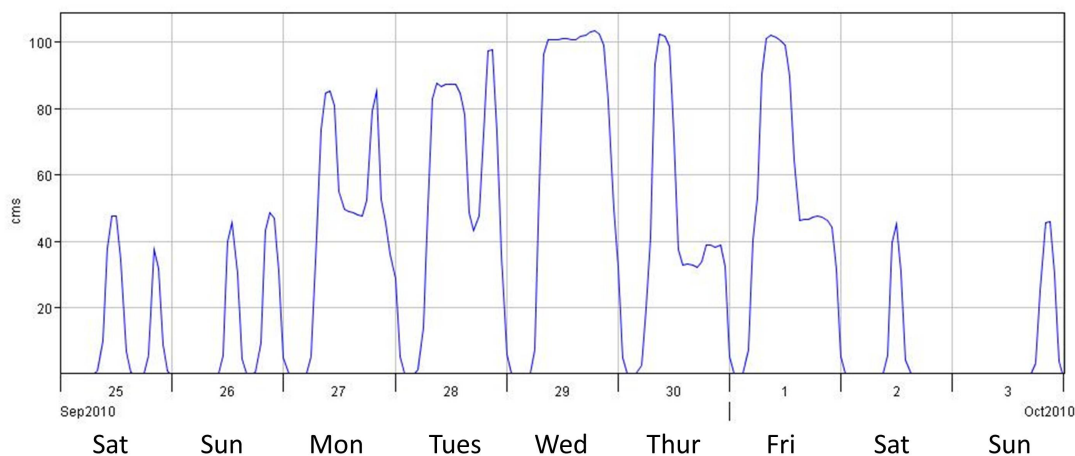


Figure 2-6: Typical nine days of discharge through Bratsberg power station from the end of September and beginning of October 2010. Bratsberg operates within the ranges of 40-50 m^3/sec , and 80-100 m^3/sec , indicating its use of one and two turbines running at 40-50 m^3/sec each.

several years before this practice was introduced in other Norwegian rivers. Commercial salmon fishing was permitted in the river until the mid 1970's, but since then fishing activity has been restricted to sport fishing with rods. In a productive year (2007 for example) the nine kilometer long salmon bearing reach of Nidelva can produce over a ton of salmon per kilometer from a series of world renowned fishing beats including: Lerifosshølen, Stryket, Kroppanhølen, Renna, Trekanten, Vanvikhølen, Nydalsdammen, Valøya, and Tilfredshet (Fremstad and Thingstad, 2007). The two kilometer stretch below Nedre-Leirfoss is the most important spawning ground for both salmon and seatrout, however spawning has been observed as far downstream as the "Downstream" observation position shown in Figure 2-4. Local seatrout stocks are in decline in many of the large rivers around Trondheims fjord, a trend that is the focus of ongoing research (Winther and Olafsen, 2007).

Water that enters the study reach through hydropeaking activity passes through the Bratsberg power station, which has its intake in the Selbusjøen reservoir at 151.9 meters above sea level. The reservoir is regulated to maintain a water surface elevation between 151.9 and 158.2 meters above sea level, placing the Bratsberg intake within the top 6.3 meters of the reservoir year round (Engebretsen, 2010). Selbusjøen is known to stratify

seasonally, however this occurs well below the Bratsberg intake at a depth of approximately 15 meters. With Bratsberg's intake drawing water from the epilimnion, it is drawing water from the same stratigraphic region as the water that enters the bypass reach. The classic view of thermopeaking lies in drawing water from multiple sources with different temperatures, but this system illustrates the impact that pathways have on temperature by exposing one pathway to atmospheric and the other to subterranean heat fluxes. The difference in water temperature between Bratsberg and Nidelva was acknowledged by the state run power company, StatKraft, in a report released in 2010, which focused on the development of the Svean power plant (Engebretsen, 2010). Thermopeaking events in this system are anticipated to have smaller amplitude than systems with deepwater intakes, and yet the social impacts of subdued thermopeaks in this socially important river could have more significant impacts than the impressive thermal swings seen in remote alpine systems with deepwater intakes (Fremstad and Thingstad, 2007). To this end, the system was also modeled as if Bratsberg were a deepwater intake facility. The potential thermal impacts of Bratsberg as a deepwater intake shed light on the degree of protection that Nidelva already receives from thermopeaking due to its construction style.

2.2 Data Collection

Data for the current condition analysis were collected for the hydrologic year 2010 (October 2010 through October 2011). As hydropeaking and thermopeaking were the focus of this work, discharge and river temperature records were assembled from various sources. Because Norway observes daylight saving time, the field site was located at UTC +2h during the summer, and UTC +1h during the winter. The adjustment days were the 28th of March 2010, 31st of October 2010, 27th March 2011, and 30th October 2011. Data were adjusted so that all records were in UTC +1h.

2.2.1 Bathymetric Data

River bathymetry was collected as a compilation of data from previous projects, and original surveys. All bathymetric data were collected using Acoustic Doppler Current Profilers

(ADCP) from a variety of platforms including motor boat, kayak, and an unmanned vessel drawn across the river on a cable-way. The unpublished “Hull i alluvier elva” project from the Department of Geology at NTNU in 2008, the masters thesis for Peter Borsanyi (Borsanyi, 1998), and modelling efforts of Håkon Sundt in 2009 (Sundt, 1984) all contributed bathymetric data for this thesis work. The results of these efforts is a series of 58 measured cross sections with minimum, average and maximum spacing of 25, 200, and 1200 meters (Figure 2-7, left). These observed cross sections were the basis for the interpolation of 77 more cross sections, ensuring that the maximum distance between cross sections was less than 100 meters (Figure 2-7, right). This linear 3-dimensional interpolation was performed to allow the water quality modelling to be performed on a finer scale than would be permitted with only the observed cross sections.

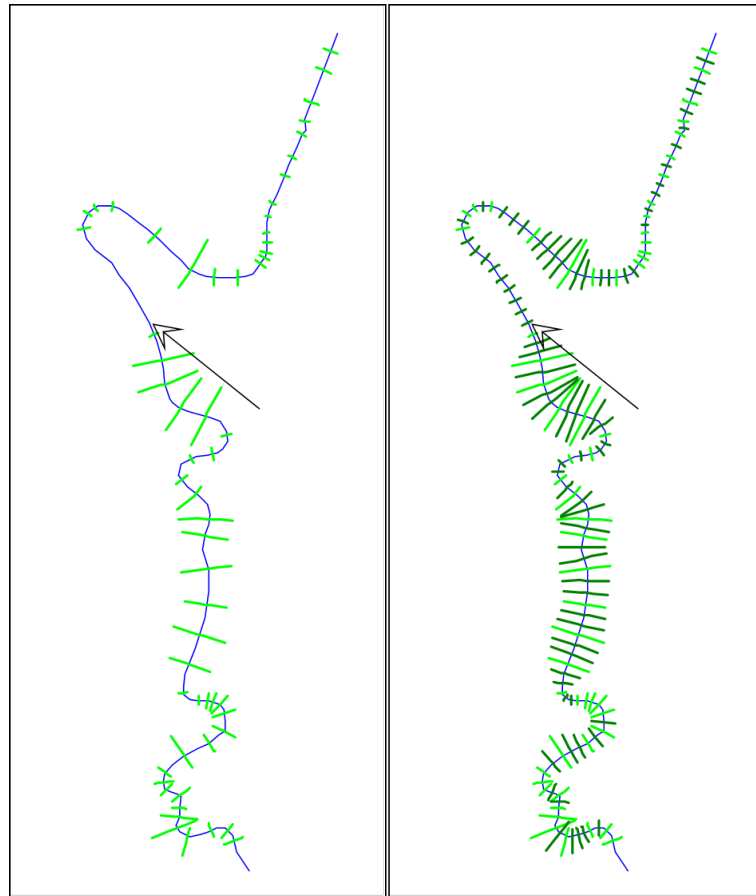


Figure 2-7: Measured (left) and interpolated (right) cross-sections.

2.2.2 Discharge Data

Total river discharge was reported at the Rathe gauge station shown in Figure 2-3. This gauge station, operated by the Norwegian Water and Energy Directorate (NVE), utilizes a rating curve to convert observed hydrostatic pressure to discharge, and reports on hourly time steps. Discharge data provided by StatKraft, the Norwegian state-run power company responsible for the Bratsberg power station, allowed total discharge values to be decomposed into two constituents: tunneled and instream flow from the Selbusjøen reservoir (Equation 2.1).

$$Q_{Rathe} = Q_{Tunneled} + Q_{Instream} \quad (2.1)$$

Q_{Rathe}	=	Discharge at the upstream boundary of the study reach	[m ³ /sec]
$Q_{Tunneled}$	=	Discharge through the Bratsberg power station	[m ³ /sec]
$Q_{Instream}$	=	Discharge through the Leirfossen complex	[m ³ /sec]

Tunneled flow in this case represents water that is routed from the reservoir directly to the study reach with no interaction with the atmosphere, and is comprised entirely of discharge through the Bratsberg power station.

Bypass discharge from from the Selbusjøen reservoir is divided into three components when it arrives in the Leirfoss complex as shown in Figure 2-3: flow through the Leirfossene power station, flow through the Nedre-Leirfoss power station, and flow that bypasses both of these and spills over the waterfall known as “Leirfoss”. Nedre-Leirfoss has a penstock approximately 150 meters in length and discharges directly into the river just below the Leirfoss waterfall. Leirfossene power station is a subterranean installation with a 200 meter penstock and a 1,400 meter tailrace that discharges just below the Leirfoss waterfall. Water that is not directed through Leirfossene flows over Øver-Leirfoss dam or through the Øvre-Leirfoss power station and is then routed either through the Nedre-Leirfoss power station, or is spilled over the Leirfoss waterfall. The Lerifossene, Øvre-Lerifoss, and Nedre-Leirfoss power stations have virtually zero storage capacity, drawing water from near the surface,

and are operated almost indistinguishably from “run of the river” plants. For these reasons, the water through the power stations in the Leirfoss complex are considered to have the same temperature as water flowing in the main river channel, and total instream discharge is calculated as the sum of discharge through these three distinct pathways.

The upstream boundary for the study reach is located at the confluence of the Bratsberg, Nedre-Leirfoss and Leirfossene tailrace outlets, just below the Leirfoss waterfall. The Rathe gauge provides a record of total discharge through these four pathways, and the discharge record reported for Bratsberg allows the discharge signal to be decomposed into flow through Bratsberg and instream flow. This distinction is important for analysis of water temperature as the tunneled and instream flows may display different temperature signals.

2.2.3 Temperature Data

River temperature data were collected using a series of six VEMCO Minilog-II-T submersible temperature loggers placed at four locations along the study reach to observe evolution of temperature signals as they are transported downstream. Three loggers were placed along the study reach during the study period at the Rathe stage gauge (upstream), the Trekanten rapids (midstream), the St. Olav’s hospital bridge (downstream) (Figure 2-4). The temperature logger at upstream site has remained in place since its initial deployment, and the loggers at the midstream and downstream locations were redeployed for the verification period. Three additional loggers were deployed during the verification period as well: at the mouth of the river (fjord), the outlet of the Bratsberg tunnel (Bratsberg), and the intake to Leirfossene (headwater) (Figure 2-4). These three additional loggers were used to demonstrate that the downstream location is above tidal flow and to verify the mixing models used for the future discharge scenarios. All temperature data were collected with 0.01° Celsius resolution (VEMCO, 2011) in 1 minute intervals; however, the loggers were installed for varying periods as described in Table 2.2.

The temperature loggers were anchored to stones, tied to the shore and cast a few meters into the river to ensure that the logger would remain submerged at low flows. The use of point measurements to represent temperature across an entire river cross section is based on the fundamental assumption that river temperature is fully mixed across width and depth.

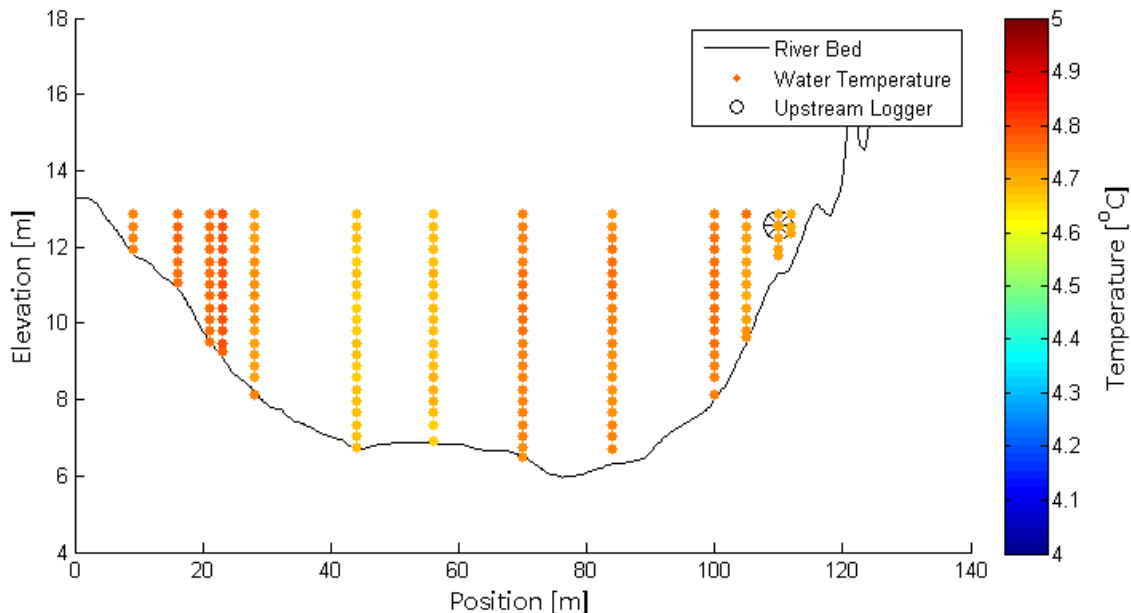


Figure 2-8: Cross section of water temperatures [°C] at the upstream logger location. Note that all observations fall within 0.1 degrees Centigrade of each other.

Table 2.2: Extent of temperature data collection.

Station	2010		2012	
	Start	End	Start	End
Fjord	-	-	17 Aug	4 Nov
Downstream	7 Oct	27 May	15 Aug	4 Nov
Midstream	7 Oct	27 May	15 Aug	4 Nov
Upstream	7 Oct	-	-	4 Nov
Bratsberg	-	-	1 Sep	4 Nov
Headwater	-	-	1 Sep	4 Nov

This assumption is substantiated by a series of temperature profiles measured across the river at the upstream temperature logger (Figure 2-8). These soundings show that there is very little distribution in temperature across width and depth as all measurements fall between 4.68°C and 4.78°C.

Reservoir Temperature Profiles

Two temperature profiles were collected for the Selbusjøen reservoir within 100 meters of the intake shaft to the Bratsberg power station to investigate the significance of intake depth on intake water temperature (Figure 2-9). They were collected on August 31st and October

31st of 2012 and show that the epilimnion decreased significantly in temperature over the 2 month period, in good agreement with the accepted schedule for fall turnover (Fremstad and Thingstad, 2007). The profile collected at the end of October (using a YSI Castaway profiler) was limited by equipment to the top 12 meters of the reservoir, while the sounding from the end of August (done with a SAIV A/S SD204 conductivity, temperature, depth profiler) reached all the way to the reservoir bottom at 28 meters below the water surface.

2.2.4 Meteorological Data

Heat fluxes into and out of each water quality model cell were driven by meteorological data that were collected from the Trondheim Voll Meteorological station (Figure 2-4) through the e-klima on-line database. Parameters collected from the Voll meteorological station were: atmospheric pressure, air temperature, relative humidity, air temperature, wind speed, and cloud cover estimates (Figure 2-10). Data were reported with six hour time steps (0000, 0600, 1200, and 1800), and linear interpolations were applied to extract values for intervening periods. Meteorologic data from 2010 are similar to data reported for 2005 though 2011 (Figure A.4). Cumulative distribution curves for 2010 meteorological parameters are presented in Figure A.4 in the appendix.

As the meteorologic station is located at 127 meters over sealevel, a full 120 meters higher than the average elevation of Nidelva's water surface, air temperature observations were adjusted to account for the station's elevation using adiabatic lapse rates. For unsaturated air, a dry adiabatic lapse rate of $-9.8\text{ }^{\circ}\text{C}/1,000\text{ meters}$ was applied, resulting in an adjustment of $+1.2\text{ }^{\circ}\text{C}$. A wet adiabatic lapse rate of $-6\text{ }^{\circ}\text{C}/1,000\text{ meters}$ was applied for periods with relative humidity above 90%, producing a change of $+0.72^{\circ}\text{C}$.

Cloud cover was reported in an octet scheme, where the sky is divided into eight quadrants that are independently evaluated for cloud cover. The resulting score was converted into a scale ranging from 0.1 to 0.9, where 0.1 represents clear skies and 0.9 represents complete cloud cover in all sectors. Solar insolation was calculated from latitude, time of year, cloud cover, and a "dust coefficient" following Equation A.1 in Appendix A. The dust coefficient is an attempt to account for atmospheric attenuation and is used as a free parameter in the calibration process. It is expected to range from zero in rural areas to 0.2 in

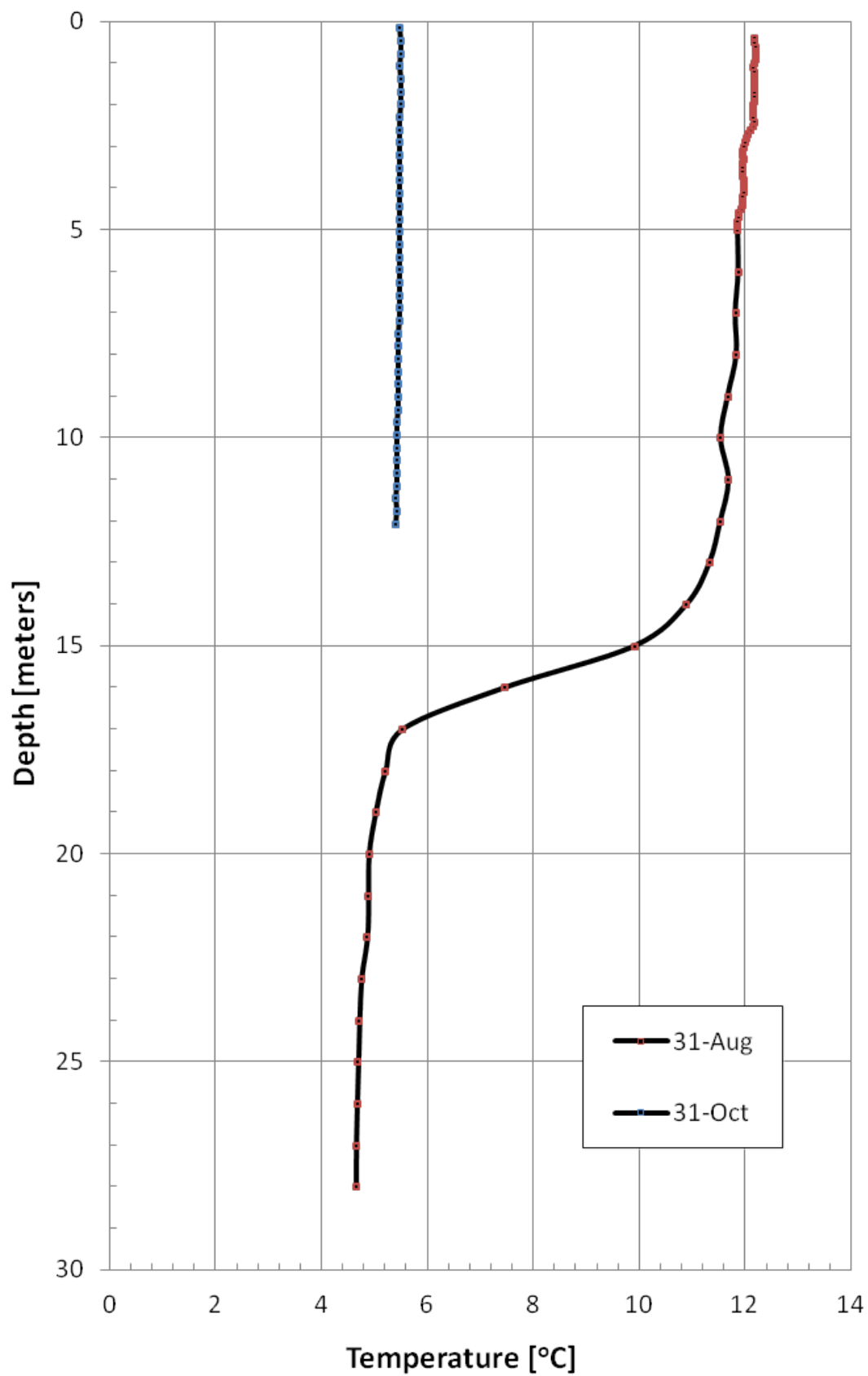


Figure 2-9: Thermal profile of Selbusjøen Reservoir.

urban environments (Brunner, 2010).

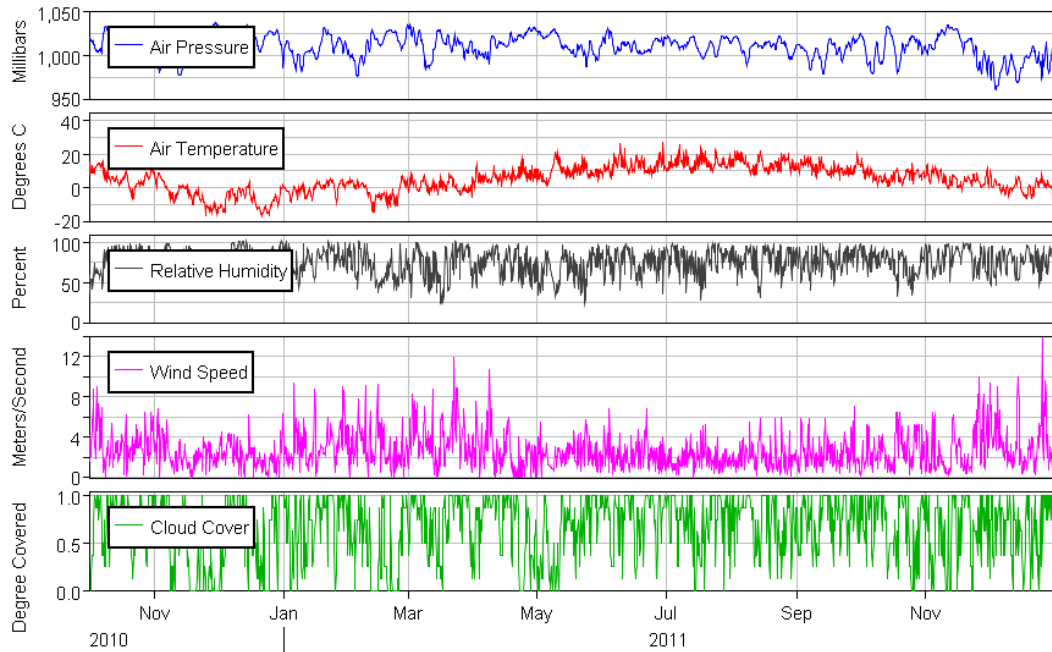


Figure 2-10: Data observed at Voll meteorological station.

2.3 Peaking Identification

Observed discharge and river temperature data were analyzed to determine the presence of hydropeaking and thermopeaking in the study reach of the River Nidelva.

2.3.1 Identification of Hydropeaking Events

In order to quantify the observations of hydropeaking, a threshold was set to separate natural discharge fluctuations from anthropogenic hydropeaking activity. Rate of change in discharge was calculated as a consecutive difference on hourly discharge data for the Bratsberg and instream discharge records. The distribution of the rates of change in discharge for Bratsberg and the bypass reach are shown in Figure 2-11. There is a break in the coincidence of discharge changes through Bratsberg and the bypass pathway at 20 m³/sec/hr. Discharge changes in the Bratsberg and bypass pathways are indistinguishable

below $20 \text{ m}^3/\text{sec}/\text{hr}$ while above this point the incidence becomes dominated by anthropogenic hydropeaks through Bratsberg (Figure 2-11). Figure 2-12 shows the distribution of all discharge deviation magnitudes in Nidelva at Rathe over the study period. The distribution of discharge deviations is bottom heavy with 93.4% of the deviations represented by magnitudes below the $20 \text{ m}^3/\text{s}/\text{hr}$ threshold. There were two distinct events where this threshold does not hold: a snowmelt event in mid May (Figure 2-13), and a rain storm in mid-August (Figure 2-14). During these events, discharge through Bratsberg was held at maximum capacity, while the discharge at the Rathe gauge rose rapidly. These peaking events are attributed to spilling of water through the Leirfoss complex, and are therefore dismissed from the thermopeaking response analysis.

The ability to report rate of change in discharge is limited by the hourly time step of the discharge record. A lower limit of ramping rates was constructed by a linear interpolation between reported discharge values. The river temperature changes at the upstream boundary (200 meters downstream of the Bratsberg discharge point) over much shorter periods giving an indication that the modification in flow occurs over sub-hourly time scales.

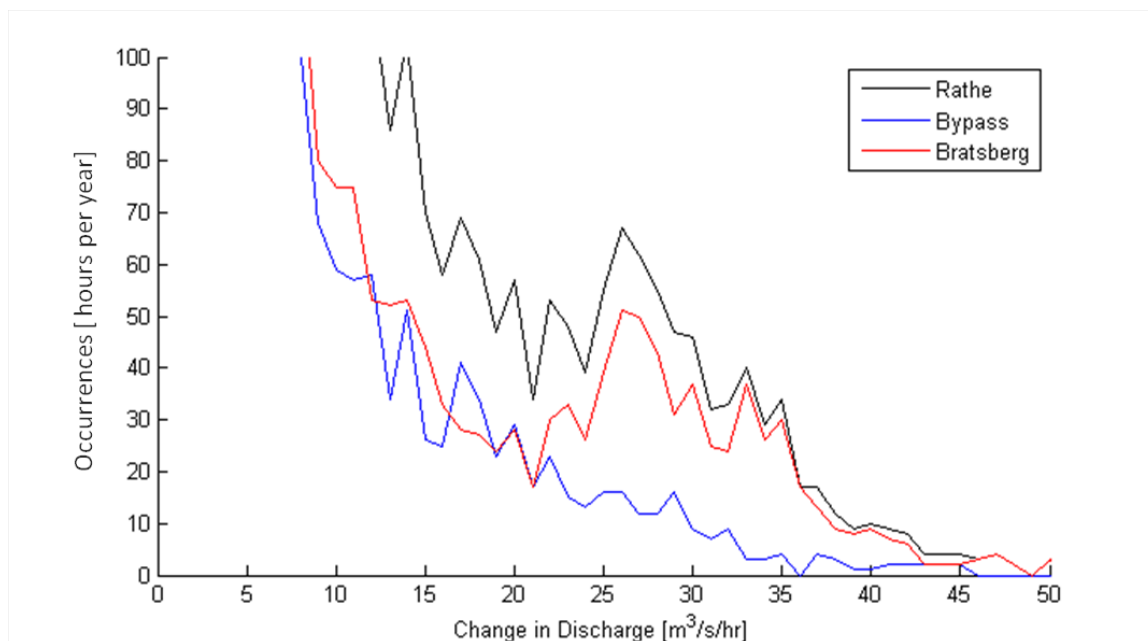


Figure 2-11: Annual histogram of hourly discharge deviations for the Bratsberg (blue) instream (red) flow pathways as well as at Rathe (black).

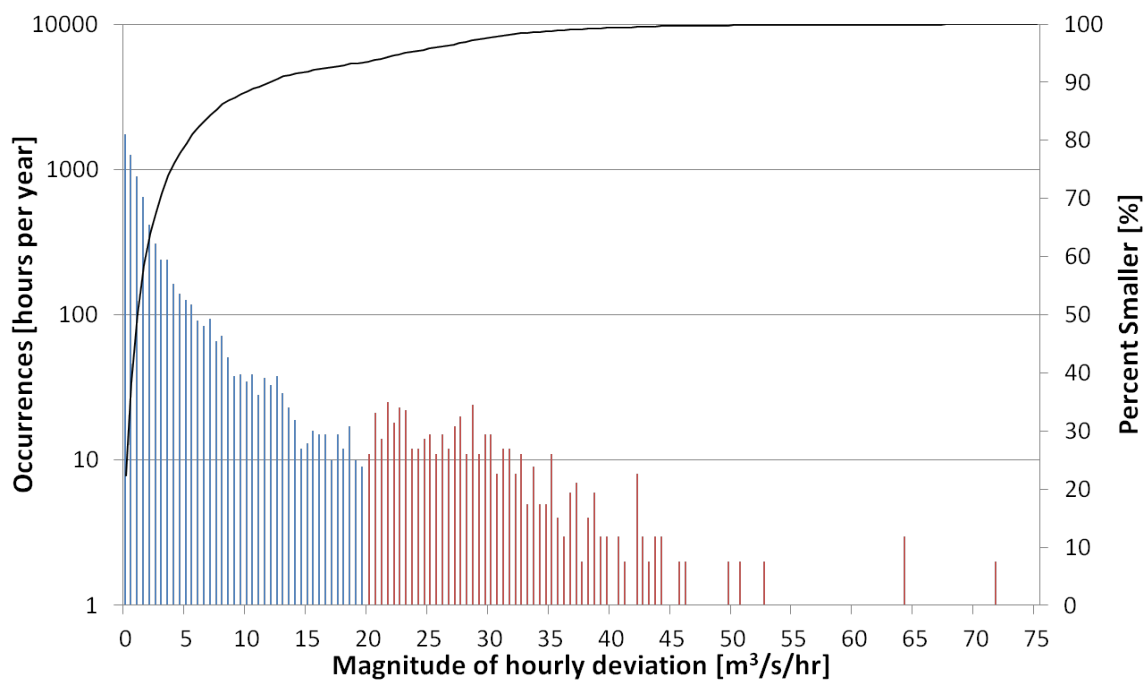


Figure 2-12: Distribution of changes in discharge reported in hourly time-steps at the Rathe gauging station. Note the log scale on the primary y-axis

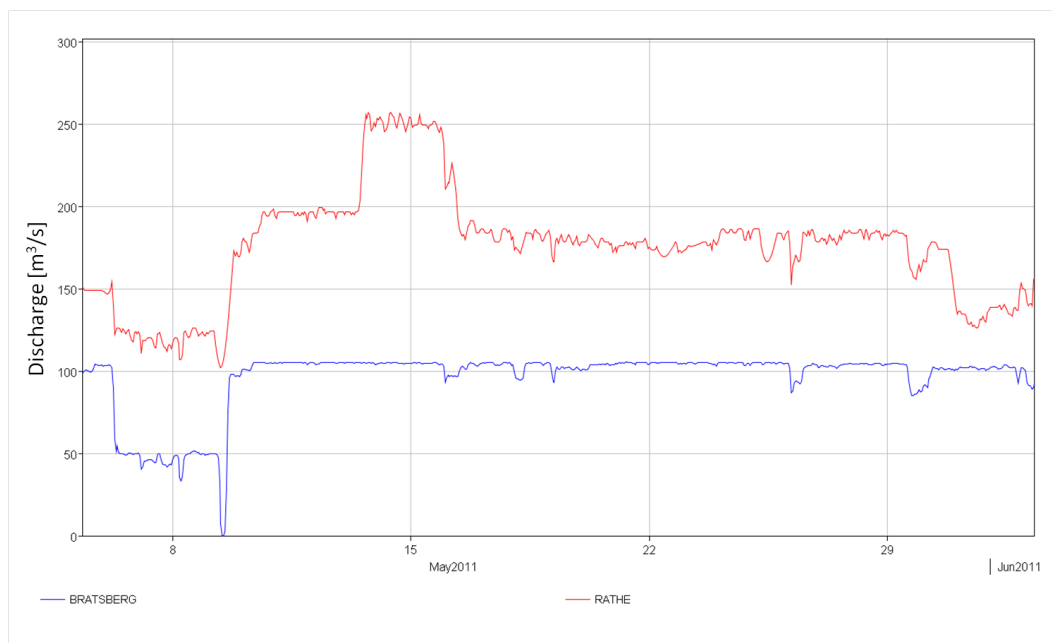


Figure 2-13: Time series of discharge at Rathe (red line) and through Bratsberg (blue line). Note that on the 15th of May discharge at Rathe increased rapidly, while discharge through Bratsberg remained constant. This event in mid-May is associated with snowmelt and subsequent spilling of water through the Lerifoss complex.

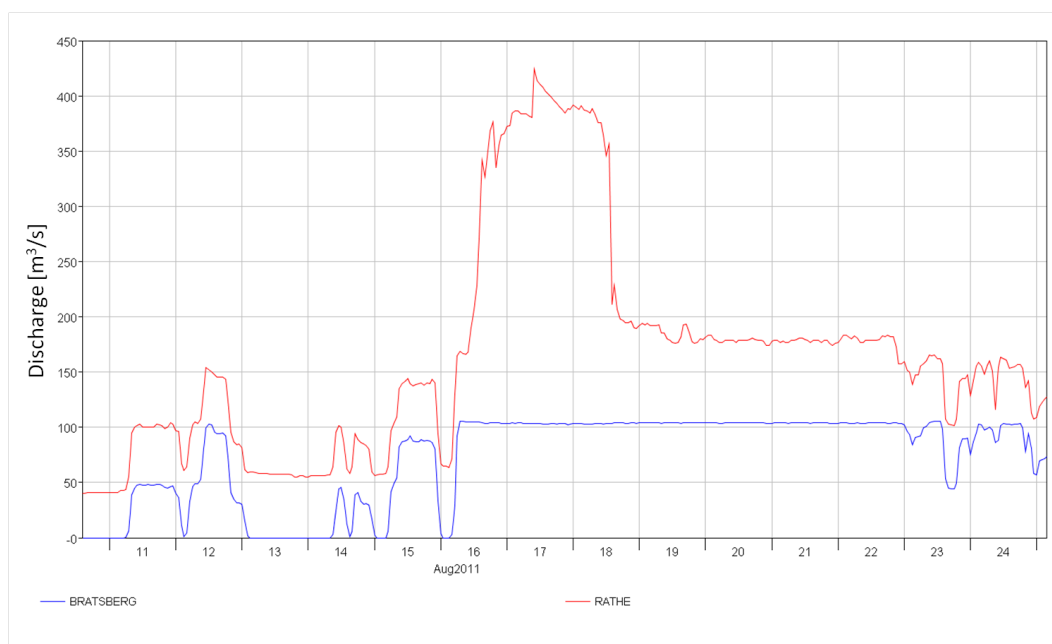


Figure 2-14: Time series of discharge at Rathe (red line) and through Bratsberg (blue line). Note that on the 16th of August the discharge at Rathe increased rapidly, while discharge through Bratsberg remained constant. This event in mid-August is associated with a heavy precipitation event and subsequent spilling of water through the Lerifoss complex.

2.3.2 Identification of Thermopeaking Events

Thermopeaking events were identified as a change in temperature coincident with hydropeaking events. The upstream location was used for this analysis as it is collocated with the Rathe gauge, the same location used for the identification of hydropeaking events. Thermopeaking observations were event based, with the maximum change in temperature over the duration of the hydropeaking event being considered as the magnitude of the event. With temperature data on one minute intervals, rates of change in temperature were far more refined than for hydropeaks that were limited to one hour intervals.

2.4 Model Construction

The construction and calibration of numerical models is a focus of this thesis work. A one-dimensional hydrodynamic model was constructed to calculate dynamic physical river attributes, such as water depth and surface width, along the study reach. Subsequently, a deterministic energy balance model was applied to the hydrodynamic output to determine dynamic water temperatures along the study reach. This pair of models was calibrated against observations of water surface elevations and water temperature before being used to model theoretical discharge regimes. Potential biological impacts from various discharge schemes were analyzed using a pre-fry development model to calculate the median date for two developmentally important thresholds: egg hatching and swim-up. Relative ice development potential was estimated with a simple threshold model.

2.4.1 Hydrodynamic Model

The model HEC-RAS 4.1 was chosen for the hydrodynamic and energy balance component of this thesis as it has been designed specifically to model systems with riverine pulse flow phenomena (Brunner, 2002, 2010; Randle and Samad, 2008), much like those expected to exist with hydropeaking operations. One limitation to the HEC-RAS modelling platform is the inherent assumption of no groundwater/surfacewater interaction. The local surficial geology is dominated by deposits of marine clay over half a meter thick, with a sizable deposit of fluvial material in the middle of the study reach (Figure 2-15). Minimal groundwater

interaction is supported for the study reach through the presence of marine clay with very low hydraulic conductivity ($0.2 - 1.1 \times 10^{-9} \text{m/s}$ (Song et al., 1999)), and highly channelized river banks through the fluvial deposit.

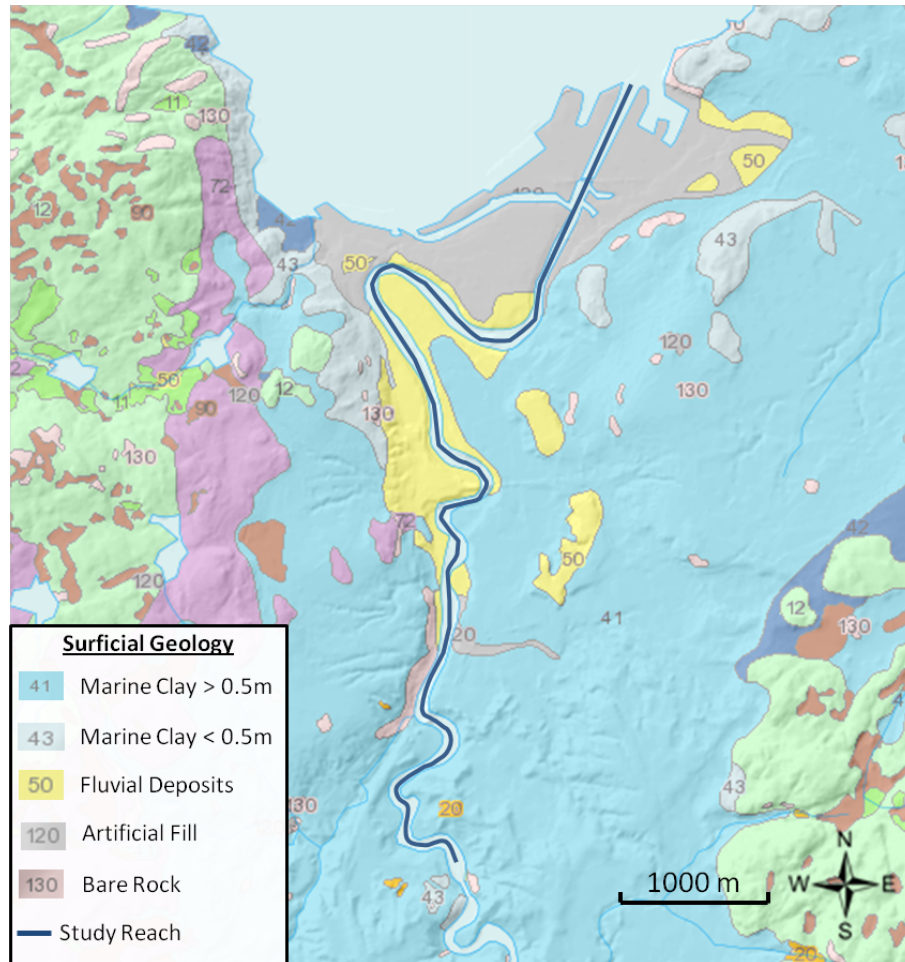


Figure 2-15: Map of overlying geologic units for the study reach. Image Source: NGU.no

Water surface elevations are computed along the length of the study reach using a standard step method to solve the energy equation (Equation 2.2). Subscripts 1 and 2 refer to the downstream, and upstream components in a pair of longitudinally consecutive locations.

$$Y_2 + Z_2 + \frac{\alpha_2 V_2^2}{2g} = Y_1 + Z_1 + \frac{\alpha_1 V_1^2}{2g} + h_e \quad (2.2)$$

Y = depth of water at cross sections

Z = elevation of the main channel inverts

V = cross-sectioned average velocity

α = velocity weighing coefficients

g = gravitational acceleration

h_e = energy head loss

Energy head loss between cross sections is calculated as:

$$h_e = L\bar{S}_f + C \left| \frac{[\alpha_2 V_2^2]}{2g} - \frac{\alpha_1 V_1^2}{2g} \right| \quad (2.3)$$

h_e = energy head loss

L = discharge-weighted reach length

\bar{S}_f = representative friction slope between two cross-sections

C = expansion or contraction loss coefficient

α = velocity weighing coefficients

V = cross-sectioned average velocity

g = gravitational acceleration

The user provides an initial water surface elevation for the upstream (or downstream in the case of supercritical flow) boundary, from which the total conveyance and velocity head are calculated. The representative friction slope between two sections is then calculated based on the roughness of the channel section, allowing head loss to be calculated. With the values

of head loss and velocities, the water surface at the given boundary is recalculated and the

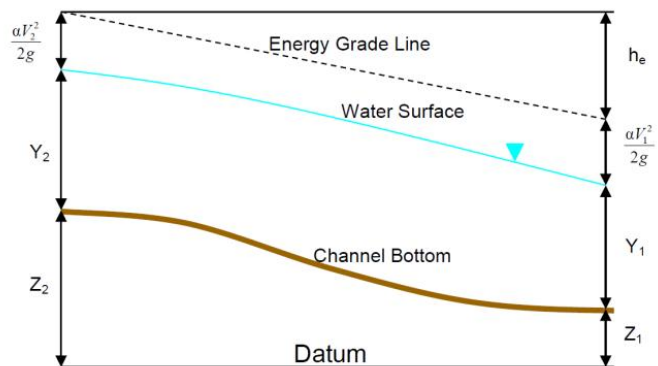


Figure 2-16: Schematic of head loss between cross sections. Image Source: Brunner (2002).

process is iterated until the difference in model between iterations is within a user specified tolerance. The user is required to specify initial conditions as well as discharge time series for both the up- and down-stream boundaries. The hydrodynamic model is calibrated through cross section specific bed roughness values (Manning's n). The reader is referred to Chapter 2 of the Hydraulic Reference Manual for more information on hydraulic routing in HEC-RAS (Brunner, 2002).

Ultimately, the hydrodynamic component takes a time series of stage or discharge measurements and routes that flow through a river geometry to compute the temporally and spatially discrete water volumes and surface areas for use in the water quality module. The basic data requirements are river geometry and stage or discharge. The model was run with five minute time steps, a time step suitable for the dynamics of the system where hydropeaking is seen to occur over 15 to 20 minute periods.

Hydrodynamic Boundary Conditions

Observations of river discharge from the Rathe gauging station (hourly interval) were applied to the upstream boundary of the hydrodynamic model reach, while observations of water level in Trondheimsfjord (ten minute intervals) were used to account for diurnal tidal fluctuations and storm surges in the elevation of the downstream boundary. Data on water level in Trondheimsfjord were sourced from a sensor maintained by Trondheim Havn and made publicly available through the Vannstand project under StatKart, Norway's federal cartographic agency. Linear interpolations were applied to the stage and discharge records for model runs with shorter computational time-steps than the reporting intervals. Streamwise water level observations were used to calibrate the hydrodynamic model through adjustments in Manning roughness coefficients.

Hydrodynamic Calibration and Verification

The hydrodynamic component of the HEC-RAS model of Nidelva was calibrated against observed waterlines at steady flows. Point elevations were measured along the length of the study reach using a Leica CS15 differential GPS using an RTK data link to a local fixed point over the cell phone network. Each set of points was collected in surveys lasting

less than two hours, over periods of stable discharge in the month of September 2012. Observations were taken on falling limbs of natural hydrographs, after a minimum of 5 days with no precipitation. Discharge in the study reach was reported at the Rathe gauging station to change by less than 5 m³/sec during each survey. Steady state simulations of discharges that corresponded to observed water lines were used to calibrate bed roughness coefficients (Manning's n) for each cross-section. An initial value of 0.04 was applied to the entire study reach, and adjustments were made manually working from the downstream boundary up the study reach one cross-section at a time. The arrival timing of thermopeaks at the midstream and downstream locations throughout the model period and was used to validate the hydrodynamic model.

2.4.2 Energy Balance Model

River temperatures are modeled with the spatially discrete deterministic water quality module of HEC-RAS. Heat is transported through the system following the advective dispersive equations (Equation 2.4), and solved using a backwards difference QUICKEST-ULTIMATE time explicit numerical scheme (Jensen, 2004).

$$\forall^{n+1}\phi^{n+1} = \forall^n\phi^n + \Delta t \left[Q_{up}\phi_{up}^* - Q_{dn}\phi_{dn}^* + \Gamma_{dn}A_{dn}\frac{\delta\phi_{dn}^*}{\delta x_{dn}} - \Gamma_{up}A_{up}\frac{\delta\phi_{up}^*}{\delta x_{up}} \right] + \Delta t\frac{\delta\phi}{\delta t}SS \quad (2.4)$$

ϕ^{n+1}	= Thermal energy at the present time step	[°C/m ³]
ϕ^n	= Thermal energy at the previous time step	[°C/m ³]
ϕ_{up}^*	= QUICKEST thermal energy at the upstream face	[°C/m ³]
$\frac{\delta\phi_{up}^*}{\delta x_{up}}$	= QUICKEST derivative of thermal energy at the upstream face	[°C/m ⁴]
Γ_{up}	= Upstream face dispersion coefficient	[m ² /s]
\forall^{n+1}	= Volume of the water quality cell at next time step	[m ³]
\forall^n	= Volume of the water quality cell at current time step	[m ³]
Q_{up}	= Upstream face flow	[m ³ /s]
A_{up}	= Cross sectional area of the upstream face	[m ²]
$\frac{\delta\phi}{\delta t}SS$	= Cell energy budget terms	[°C/m ² s ⁻¹]

The dispersion coefficient of the water quality module allows for modeled contaminants to experience longitudinal dispersion based on the water velocity, depth, channel width, and shear velocity. The dispersion coefficient was computed for each water quality cell face for each time step, using Equation 2.5.

$$\Gamma = 0.011 \frac{V_{up}^2 w^2}{Y u^*} \quad (2.5)$$

V_{up}	=	Velocity of water at upstream face	[m/s]
w	=	Average channel width	[m]
Y	=	Average channel depth	[m]
u^*	=	Shear velocity	[m/s]

with friction velocity u^* calculated as:

$$u^* = \sqrt{gY S_f} \quad (2.6)$$

g	=	Gravitational constant	[9.81 m/s ²]
Y	=	Average channel depth	[m]
S_f	=	Friction slope	[unitless]

Minimum and maximum bounds were placed on the dispersion coefficient with Equation 2.7 based on criteria outlined by Drake et al. (2010).

$$\Gamma_{max,min} = 0.6 \cdot Y_{max,min} \sqrt{gY_{max,min} S_{f,max,min}} \quad (2.7)$$

$\Gamma_{max,min}$	=	Maximum or Minimum dispersion coefficient	[m ² /s]
$Y_{max,min}$	=	Maximum or Minimum channel depth	[m]
g	=	gravitational constant	[9.81 m/s ²]
$S_{f,max,min}$	=	Maximum or Minimum friction slope	[unitless]

Simulations of the minimum and maximum observed discharges were used to calculate the minimum and maximum dispersion coefficient limits. Cross section average depths ranged from 0.83 to 8.59 meters, and the friction slope values ranged from 0.000018 to 0.007462 over the non-tidal segment of the study reach. These values result in dispersion coefficient boundaries of 0.01 and 4.1 m²/s.

Unlike the hydrodynamic component of the HEC-RAS model where timesteps are fixed to a user-specified constant, the water quality component dynamically calculates time steps to meet Courant and Peclet number requirements, as well as a user-specified maximum allowable timestep. To expedite model runs, the dynamic time steps were set to the longest possible lengths - up to the user-specified maximum - that maintain a Courant condition less than 0.9 (Equation 2.8) and a Peclet number of less than 0.4 (Equation 2.9). The maximum allowable time step was set to five minutes to ensure that thermopeaking events, observed to occur over 15 to 20 minute periods, were modeled with at least three points.

$$C_{us} = V_{up} \frac{\Delta t}{\Delta x} \leq 0.9 \quad (2.8)$$

C_{us}	=	Local Courant number	[unitless]
V_{up}	=	Velocity of water at upstream face	[m/s]
Δx	=	Length of water quality cell	[m]
Δt	=	Time step	[s]

$$\alpha_{us} = \Gamma_{us} \frac{\Delta t}{\Delta x^2} \leq 0.4 \quad (2.9)$$

α_{us}	=	Local Peclet number	[unitless]
Γ_{us}	=	Dispersion coefficient at upstream face	[m ² /s]
Δx	=	Length of water quality cell	[m]
Δt	=	Time step	[s]

Cell energy budget terms ($\frac{\delta\phi}{\delta t}SS$ in Equation 2.4) are calculated for each water quality cell for each time step based on meteorological conditions, the surface area, and the volume of the water quality cell, as described in Equation 2.10. Note that heat fluxes are limited to atmospheric exchange, assuming no conduction from the bed, and no convection from groundwater interaction.

$$\frac{\delta\phi}{\delta t}SS = \frac{q_{net}}{\rho_w C_{pw}} \frac{A_s}{\forall} \quad (2.10)$$

Volume and surface areas of the water quality cells are calculated by the hydrodynamic

q_{net}	=	Net heat flux at the air water interface	$[\text{W m}^{-2}]$
ρ_w	=	Density of water	$[\text{kg m}^{-3}]$
C_{pw}	=	Specific heat of water	$[\text{J kg}^{-1} \text{C}^{-1}]$
A_s	=	Surface area of water quality cell	$[\text{m}^2]$
\forall	=	Volume of water quality cell	$[\text{m}^3]$

model while the net heat fluxes are calculated for each time step as the sum of heat fluxes from five sources as described in described in Appendix A and presented in Equation 2.11.

$$q_{net} = q_{sw} + q_{atm} - q_b + q_h - q_t \quad (2.11)$$

q_{net}	=	Total heat flux	$[\text{W m}^{-2}]$
q_{sw}	=	Solar radiation	$[\text{W m}^{-2}]$
q_{atm}	=	Atmospheric longwave radiation	$[\text{W m}^{-2}]$
q_b	=	Back longwave radiation	$[\text{W m}^{-2}]$
q_h	=	Sensible heat	$[\text{W m}^{-2}]$
q_t	=	Latent heat	$[\text{W m}^{-2}]$

As with the hydrodynamic component of HEC-RAS, the water quality component disregards interaction with groundwater. Hyporheic exchange and thermal storage in the bed material are assumed to be negligible. These are all shortcoming with this particular modelling approach, however, the impacts of these oversights are minimized in this system through limited groundwater interaction.

Energy Balance Boundary Conditions

Modelling of temperature along the length of the study reach is highly dependent on the temperature of water flowing into the model across the upstream boundary. The temperature record collected at the Rathe gauging station (Upstream in Figure 2-4) was used for this boundary condition for cases of modelling observed thermopeaking.

Energy Balance Calibration and Verification

The energy balance component of the model was run with upstream discharge and temperature as inputs and calibrated against observations taken at the Midstream and Downstream logger locations from October 7th 2010 through May 27th 2011. The variables available for calibration, as well as their applicable equations, and typical values are outlined in Table 2.3.

Table 2.3: Energy balance model parameters. Ranges provided by HEC-RAS user manual.

Parameter	Applicable Equation	Suggested Range
Dust Coefficient	A.1	0.0 - 0.2
Diffusivity Ratio	A.5	0.9 - 1.1
	<i>a</i>	$\sim 10^{-6}$
Wind Function	<i>b</i>	$\sim 10^{-6}$
	<i>c</i>	~ 1

The free parameters were adjusted manually to fit modeled temperatures to observed temperatures. Each parameter was first changed to the computational limits one at a time, and the resulting coefficient of determination was calculated for observed and modeled temperature records at the midstream and downstream locations. Model residuals for the calibration process were calculated with Equation 2.12. A “degree day” accumulation approach was used to quantify the accumulated deviation between observed and modeled temperature records. A degree day difference is the integral of difference in temperature over time, where a difference of plus one degree day is equivalent to a difference of the model producing water that was one degree warmer than that which was observed for a duration of one day.

The energy balance model was verified using two month long data series of observed temperatures at the midstream and downstream locations from September 1st through November 4th 2012. These data were not used in the calibration procedure.

$$R_{i,j} = T_{i,j,model} - T_{i,j,obs} \quad (2.12)$$

Where:

$$\begin{aligned} R_{i,j} &= \text{Residual at time step } i, \text{ for location } j && [^{\circ}\text{C}] \\ T_{i,j,model} &= \text{Modeled temperature for timestep } i \text{ at location } j && [^{\circ}\text{C}] \\ T_{i,j,obs} &= \text{Observed temperature for timestep } i \text{ at location } j && [^{\circ}\text{C}] \end{aligned}$$

2.4.3 Parameter Sensitivity

Parameter sensitivity was calculated for each free parameter as well as for each model input by running quasi-steady-state model runs, altering one model parameter at a time while keeping the other model parameters at mean values (Deas, 2000). Five different values were tested for each model parameter. For the model drivers with distribution of observed parameter values, the minimum, mean minus one standard deviation, mean, mean plus one standard deviation, and maximum values were used to calculate model sensitivity. For the model calibration parameters, the minimum, 25%, mean, 75%, and maximum suggested values were used to calculate parameter sensitivity. In all model runs, the average boundary conditions temperature of 2.27 °C was applied, and the model runs were compared to a base case model run using the average values for all parameters where river temperature rose to 2.31 °C by the end of the study reach. All model runs were performed to simulate 12 hours to remove the influence of initial conditions. The sensitivity of the energy balance model to each model parameter was calculated as:

$$\overline{S_{r,j}} = \sum_{i=min}^{i=max} \left[\frac{\Delta T_i}{\Delta P_{i,j}} * \frac{\bar{P}_j}{\bar{T}} \right] \quad (2.13)$$

Where:

$\overline{S_{r,j}}$	=	Mean relative sensitivity for the jth parameter	[unitless]
ΔT_i	=	Change in Temperature for model run i	[°C]
$\Delta P_{i,j}$	=	Change in value of parameter j for the ith model run	[parameter j units]
\overline{P}_j	=	Mean value for parameter j	[parameter j units]
\overline{T}	=	Temperature from base case model run: 2.31	[°C]

2.4.4 Salmon Growth Modelling

Salmonid species have evolved to exist in coincidence with natural river processes, with eggs and alevin development timed for optimal survival rates in natural systems (Aas et al., 2010). Alterations to the natural environment, especially to water temperature, can cause evolved development rates to fall out of synch with a whole host of natural processes, thus impacting growth and survival rates (Johnsen et al., 2010). The potential biological impacts of future discharge scenarios on salmon stocks are analyzed by modelling egg and alevin swim-up development from the HED-RAS energy balance model results. The egg development model was first presented by D.T. Crisp in 1981 as a statistical analysis to relate water temperature to egg development of five salmonids: brown trout (*Salmo trutta*), brook trout (*Salvelinus fontinalis Mitchell*), rainbow trout (*Salmo gairdneri Richardson*), Chinook salmon, [*Oncorhynchus tshawytscha* (Walbaum)], and Atlantic salmon (*Salmo salar*) (Crisp, 1981). This preliminary model is based on a curve fitting of a power equation (Equation 2.14) to observed data on egg hatching. Heat is accumulated from the time of spawning until the egg development reaches unity and 50% of the population is considered to have hatched. The variable D_{egg} represents the percentage progression towards the accumulation of the total heat required.

$$D_{egg} = \sum_{i=SpawningDate}^{i=HatchingDate} \left(\frac{1}{10^{a \cdot \log_{10}(T_i - t_o) + b}} \right) \quad (2.14)$$

D_{egg}	=	Progression towards hatch date	[%]
a	=	Fitting parameter	[°C ⁻¹]
T_i	=	Water temperature at timestep i	[°C]
t_o	=	Fitting parameters	[°C]
b	=	Fitting parameter	[unitless]

Crisp further developed the model to include calculations for the date of alevin swim-up (Crisp, 1988). Heat is accumulated from the time of hatching until the degree of alevin development reaches 100%, at which point 50% of the population is considered to have emerged and graduated to become “parr,” the subsequent stage in salmonid development. The equation for swim-up development is similar to egg development, with the exception of the temporal limits (Equation 2.15). Alevin development takes less time than egg-development, and the fitting parameter “a” is subsequently smaller in the alevin development stage than in the egg development stage.

$$D_{alevin} = \sum_{i=HatchingDate}^{i=Swim-upDate} \left(\frac{1}{(10^{a \cdot \log_{10}(T_i - t_o) + b})} \right) \quad (2.15)$$

D_{alevin}	=	Progression towards swim-up date	[%]
a	=	Fitting parameter	[°C ⁻¹]
T_i	=	Water temperature at timestep i	[°C]
t_o	=	Fitting parameter	[°C]
b	=	Fitting parameters	[unitless]

Values for the fitting parameters were published for Atlantic salmon development by Crisp, and have been utilized in studies of salmon emergence in the Norwegian river Orkla (Crisp, 1988). The river Orkla empties into Trondheims fjord 30 kilometers west-

south-west of Nidelva. The drivers of pre-fry development are assumed to be similar in these two rivers and the same parameter values are used in a simulation of hatching and swim-up dates for Nidelva (Table 2.4). The accuracy of the Crisp model is no doubt limited for the proposed application with river temperature modeled as homogeneous over the entire water quality cell, and thermal refugia completely ignored. The impact of the limitation in model design is minimized for salmon development, as egg nests (redds) are developed

Table 2.4: Parameters used in Crisp model.

Life Stage	a	t_o	b
Egg	-2.6562	-11	5.1908
Alevin	-2.5013	-11	5.1908

in loose gravel with high through-flow (Aas et al., 2010). Seasonal trends in model values for the temperature of mainstream flow should therefore reasonably approximate the temperature regimes experienced by salmon eggs and alevin.

2.4.5 Ice Development Potential

Ice formation is problematic for Nidelva as ice breakup could cause damage to boats and docks anchored in the lowest few kilometers of the river (Fremstad and Thingstad, 2007). The water quality component of HEC-RAS is limited to positive water temperatures and does not simulate ice formation due to the stratified nature of ice formation, coupled with HEC-RAS's assumption of homogeneity within a water quality cell (Brunner, 2010). The potential for ice formation was estimated with a simple criteria of super cooled water (0°C), air temperatures less than -5°C , and a heat flux less than -100 Watts/m^2 (Daly, 1991). Ice production potential was estimated at the downstream location to avoid the interaction with tidal water. Simulations farther downstream would need to take a lower freezing point into account to address the lower point of solidification for sea water.

2.5 Modelling Impacts of Future Discharge Scenarios

Once observed hydro- and thermopeaking events were described and modeled, potential impacts of future discharge scenarios were tested. These scenarios were created in accordance with the proposed large scale development of wind power in northern Europe (Jan De Decker, 2011). Three scenarios were tested based on a record of observed wind speeds collected over regions intended to be developed for wind power (Figure 2-17). Discharge from the Bratsberg power station was estimated from the wind power production record for three distinct operational strategies: two seasonal production approaches and one peaking production approach. River temperature boundary conditions were calculated for the upstream boundary based on the new discharge mixtures from temperature records for the Bratsberg discharge and instream flow from 2010. Meteorological data from the 2010 water year were used to calculate heat fluxes along the study reach. The biological and economic impacts of alterations in river temperature was analyzed for each new discharge scenario

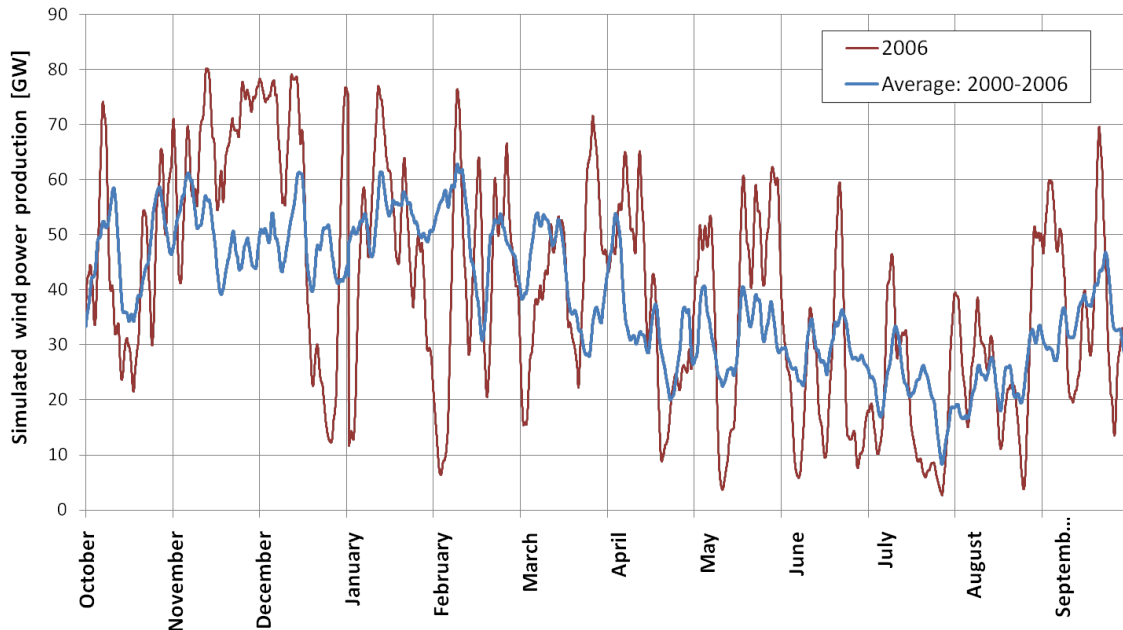


Figure 2-17: Time series of potential wind power production for the calendar year 2006 (red) and hourly averaged potential power production from 2000 through 2006 (blue). In both cases, a three day moving average was used to smooth the data. Data source: TradeWind EU-IEE project, 2009 www.trade-wind.eu

through the Crisp model for salmon development, and the ice production potential model.

2.5.1 Generating Discharge Records

The three future discharge scenarios used in this work were based on wind power production potential reported by the Norwegian research group, SINTEF. The three simplified operational strategies employed were: FullSpring, FullSummer, and Dynamic2006. FullSpring and FullSummer were generated from the long term trends observed in the six years of averaged data, while Dynamic2006 was produced in response to short term wind power production fluctuations observed for a single year of this period. For all three discharge scenarios, diurnal hydropeaking was removed. The total amount of water in Selbusjøen available for discharge, 2.43 billion cubic meters, was used to determine the termination of these two seasonal scenarios. The amount of water available for withdrawal from the reservoir was estimated as the sum of the minimum required flow for the reach between Leirfoss and the reservoir, and the annual discharge through Bratsberg observed in the 2010 water

year.

FullSpring and FullSummer Scenarios

In the FullSpring scenario, production through Bratsberg is held at zero during periods of high wind production (October through March) and raised to full production capacity in April when a drop in wind power production occurs (Figure 2-18). Full production is maintained as long as possible until there is only enough water in the reservoir to meet minimum flow requirements ($40 \text{ m}^3/\text{sec}$) for the rest of the year. At this point Bratsberg production is dropped to zero, allowing minimum flow requirements for the entire river from the reservoir to the fjord to be met through discharge along the river pathway. The discharge arriving through the river pathway (the aggregated discharge through Nedre-Leirfoss, over the Leirfoss water fall, and through Leirfossene) is kept the same as had been observed for the 2010 water year and is not allowed to fall below $30 \text{ m}^3/\text{sec}$. The total discharge record, used for the upstream boundary condition for the hydrodynamic model runs, is calculated as the sum of the observed discharge along the river pathway and the synthetic Bratsberg discharge records. The flow through Bratsberg was reduced for periods of high discharge to avoid any discharge above $300 \text{ m}^3/\text{sec}$.

The FullSummer scenario is identical to FullSpring, with the exception that full production does not start until the beginning of June (Figure 2-18). This strategy conserves production water until the period where the wind power production is historically at its lowest level in order to maximize the hydropower production when electricity prices are at their highest. This approach of waiting for a period of consistently high energy prices assumes an operational risk that hydropower operators might miss the opportunity to empty their reservoirs during peak energy prices. If the summer brings substantial precipitation, or the seasonal wind patterns increase earlier than expected, hydropower operators may be left at the end of the year with a reservoir full of unused production water as the price of energy drops.

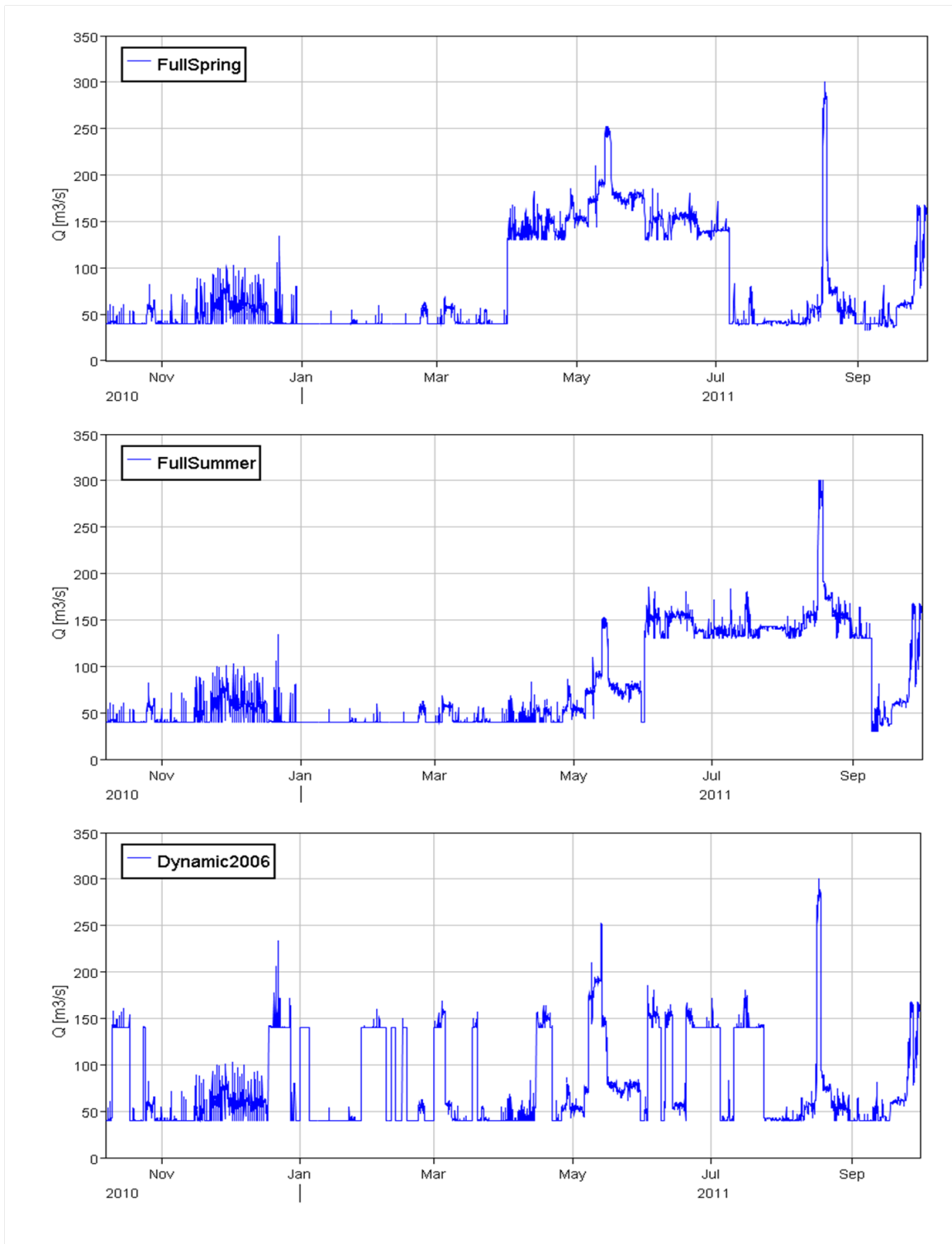


Figure 2-18: Discharge record at Rathe used to run the FullSpring (top), FullSummer (middle), Dynamic2006 (bottom) scenarios.

Dynamic2006

The third scenario, Dynamic2006, posits that Bratsberg will be used as a short-term balancing power station and should produce power in accordance with real-time wind power production. This scenario utilized a single year of wind power production observations from the North Sea to capture the weekly scale of production fluctuation (Figure 2-17). Wind production was seen to decrease for periods of several days at a time, and Bratsberg production was modeled to offset these periods as shown in Figure 2-18. As with the previous two scenarios, discharge at the Rathe gauge was held between 40 and 300 m³/s, and the total discharge was not allowed to exceed the total discharge observed for the 2010 water year.

2.5.2 Generating Temperature Records

Temperature records were computed for the upstream boundary under each proposed discharge scenario as a discharge-weighted average for heat (Equation 2.16).

$$T_{upstream_i} = \frac{Q_{Bratsberg_i} * T_{bratsberg_i} + Q_{headwater_i} * T_{headwater_i}}{Q_{upstream_i}} \quad (2.16)$$

Where Q and T represent discharge and temperature and the subscripts referred to the Upstream, Bratsberg, and Headwater locations at timestep i .

This relationship was utilized to create a time series of temperature entering the study reach for the three proposed discharge scenarios. However, temperature records were not available the Bratsberg and headwater constituents of flow for the 2010 water year, presenting the need to separate out two temperature signals from a single record. Data extraction was performed on the upstream temperature series to calculate the reservoir temperature based on the thermal response to hydropeaking events. For periods of no discharge through Bratsberg, the temperature recorded at the Upstream logger was taken as the headwater temperature. The headwater temperature is assumed to remain constant as discharge is ramped up through Bratsberg and the temperature at the Upstream logger is altered. The alteration in temperature at the upstream logger is attributed to the newly introduced discharge through Bratsberg, and the temperature of this new constituent is calculated

as the weighted average of discharges ($Q_{upstream_i}$, $Q_{bratsberg_i}$, $Q_{headwater_i}$), the observed upstream temperature ($T_{upstream_i}$), and the assumed continuation of the river temperature ($T_{headwater_i} = T_{upstream_{i+1}}$). Equation 2.16 was rearranged to solve for the Bratsberg water temperature for the commencement of every hydropeaking event (Equation 2.17).

$$T_{bratsberg_i} = \left[\frac{Q_{upstream_i} * T_{upstream_i} - Q_{headwater_i} * T_{upstream_{i-1}}}{Q_{bratsberg_i}} \right] \quad (2.17)$$

This produced a series of 507 observations for the temperature of the Selbusjøen reservoir as represented in the study reach as discharge through Bratsberg power station (Figure 2-19). The observations of epilimnion temperatures taken in the Selbusjøen reservoir on August 31st and October 31st 2012 are consistent with the temperature record generated in 2010 for the same dates. A smoothing of the calculated reservoir temperature was used to parse out the temperature of water arriving through the river pathway following Equation 2.18 (Figure 2-20).

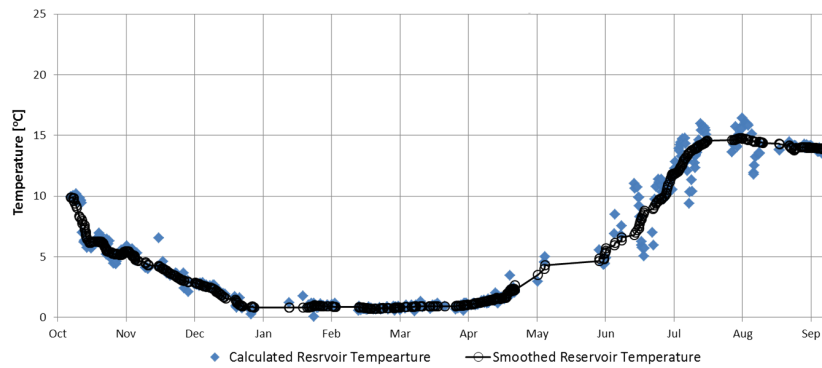


Figure 2-19: Calculated temperature of the water in the reservoir epilimnion $T_{Bratsberg}$ in Equation 2.17.

$$T_{headwater_i} = \left[\frac{Q_{upstream_i} * T_{upstream_i} - Q_{bratsberg_i} * T_{bratsberg_i}}{Q_{headwater_i}} \right] \quad (2.18)$$

Using the back calculated temperature time series for Bratsberg and the bypass reach, temperature records for each of the discharge scenarios were calculated through the con-

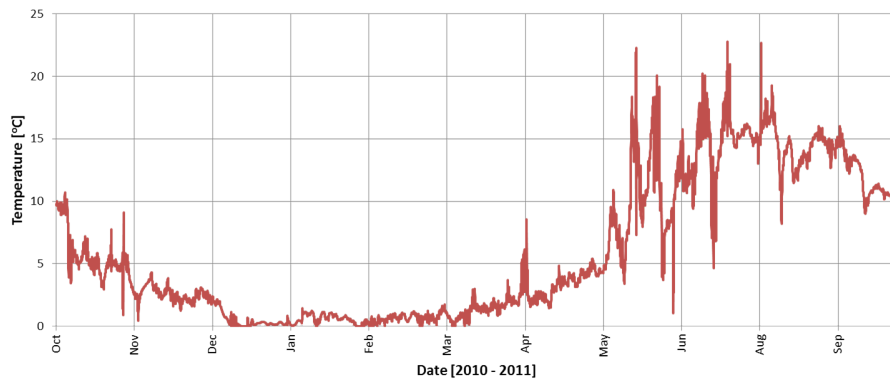


Figure 2-20: Calculated temperature of the water flowing through the river pathway to the Lerifoss complex, $T_{Headwater}$ in Equation 2.18.

servation of energy (Equation 2.16). To ensure that this approach accurately reflects the hydraulic and thermal routing of the system, the 2010 temperature record at Rathe was reconstructed using the constituent flows and calculated temperatures. The model output is compared with observed river temperature shown in Figure 2-21.

The accuracy of this method was examined during the verification period, when observations of temperature at the Bratsberg and headwater locations were measured. The same approach was used to generate reservoir and bypass reach temperature records from the temperature record at Rathe. There were 50 events of no-flow through Bratsberg that were used to generate a temperature record for the reservoir. This record agrees with the

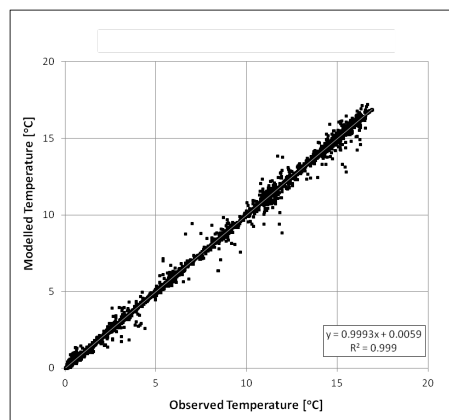


Figure 2-21: Scatter plot of observed and recreated temperature for the upstream boundary condition.

epilimnion temperatures measured in the Selbusjøen reservoir at the end of August, and the end of October. The periods of no flow through Bratsberg were used to generate a temperature record for the river. The two decomposed signals were compared against the observed temperature records at the Bratsberg and headwater locations and the comparisons are presenting in Figures 2-22 and 2-23. The reconstructed temperature at Rathe (fitting to the observed temperature record with a coefficient of determination of 0.996) for this period and is compared against the observed temperature in Figures 2-25 and 2-25.



Figure 2-22: Time series of observed (blue line) and modeled (red line) temperatures for the Bratsberg location during the validation period.

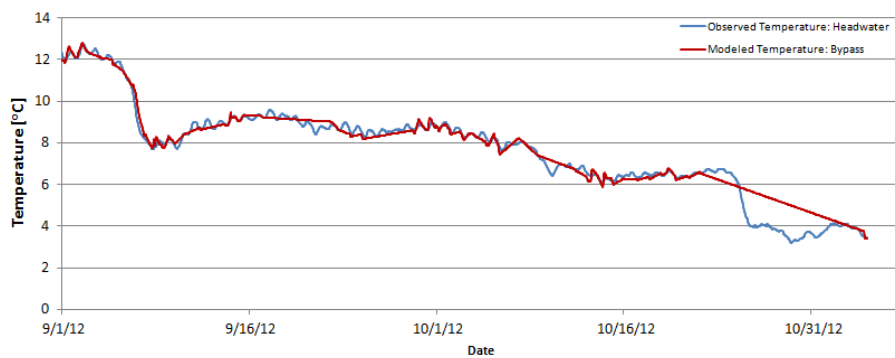


Figure 2-23: Time series of observed (blue line) and modeled (red line) temperatures for the headwater location during the validation period.



Figure 2-24: Time series of observed (blue line) and modeled (red line) temperatures for Rathe during the validation period.

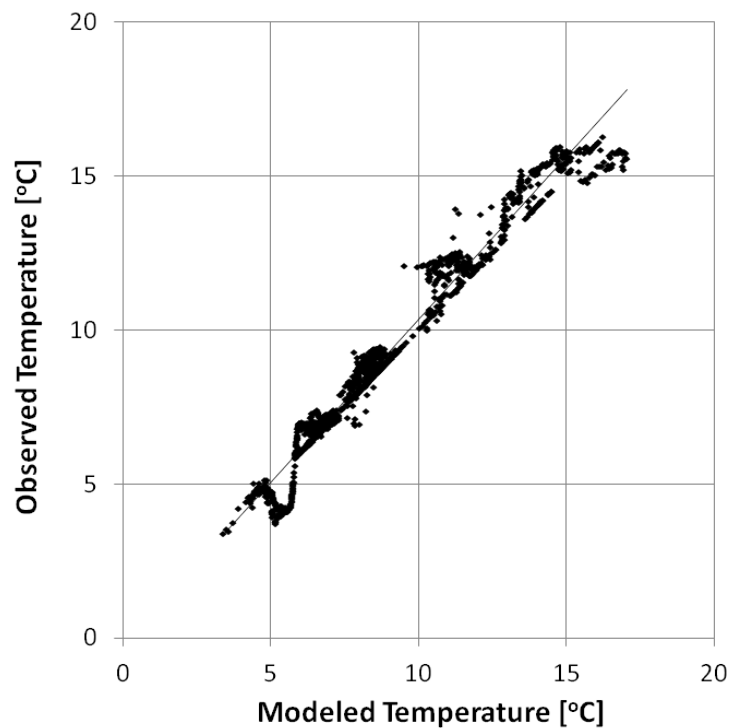


Figure 2-25: Scatter plot of observed and recreated temperature for the upstream boundary condition.

2.6 Simulating a Deepwater Intake

The Bratsberg intake is located in the epilimnion of the Selbusjøen reservoir, keeping the magnitude of observed thermopeaks rather low. The regulated minimum water level for the Selbusjøen reservoir allows the Bratsberg intake to be located fairly close to the surface

(Engebretsen, 2010). Efforts to mitigate thermopeaking (often termed thermal pollution) tend to focus on intake structure designs that incorporate water from the epilimnion (Sherman, 2000). Figure 1-5 displays some intake structure modification used to mitigate thermal pollution.

As the Bratsberg intake is already drawing water from the epilimnion, an experiment was run to estimate temperature in the River Nidelva if the Bratsberg intake were lowered to below the thermocline and into the hypolimnion. The upstream boundary condition temperatures were recalculated for the Deepwater simulations using Equation 2.19.

$$T_{upstream_i} = \frac{Q_{bratsberg_i} * T_{hypolimnion_i} + Q_{headwater_i} * T_{headwater_i}}{Q_{upstream_i}} \quad (2.19)$$

Where:

$T_{hypolimnion_i}$ = the temperature of the hypolimnion in the Selbusjøen reservoir.

As there are no actual time series of temperature in Selbusjøen's hypolimnion, an estimation was produced with an annual high of 4.68 °C taken from the August 2012 sounding, and an annual low of 4.0 degrees assumed to exist in February. This schedule follows the accepted dynamics of reservoir and lake overturn as outlined by Ryan (1968) and observed by Taner et al. (2011).

The resulting upstream boundary condition temperatures were modeled for discharge that was observed in 2010 as well as for the proposed future scenarios. The Crisp and ice development models were applied to the model output to quantify the impact these scenarios might have in a system designed with a deepwater intake.

CHAPTER 3

RESULTS

3.1 Observed Conditions

Figure 3-1 displays a year long record of discharge and temperature recorded at the upstream boundary of the study reach. Hydropeaking and the accompanying thermopeaking are observed in every month of the year. Figure 3-2 presents a closer look at a representative discharge record in the river as well as in the Bratsberg Power station from October 2010. Note the strongly peaked nature of the discharge record, and the direct connection between discharge through Bratsberg and in Nidelva. Discharge at Rathe is consistently 30-40 m³/s greater than through Bratsberg; this is indicative of the minimum flow requirements for the reach above the Lerifossen complex. Figure 3-3 illustrates this point further with discharge at Rathe peaking at 40, 80, and 150 m³/s while the Bratsberg discharges focus on 50 and 100 m³/s. The observed distribution for Rathe agrees well with the discrete discharges produced from various hydropower production schemes presented in Table 2.1.

The peaks in production are seen to coincide with fluctuations in electricity price as shown in Figures 3-4 and 3-5. These data indicate that Bratsberg is used to produce power based on short-term fluctuations in electricity price, and that discharge through this plant is likely to change with future development of wind power through alterations in the price of power.

3.1.1 Observations of Hydropeaking

The hydropeaking threshold, set to 20 m³/s/hr, produced 506 events over the 366 day study period, or 1.3 events per day. There were 375 events on weekdays and 131 events on weekend days resulting in 1.43 events per weekday and 1.25 events per weekend day on average. There were 162 days with no active hydropeaking, and when these days are removed from the calculation, the daily average occurrence of hydropeaking rises to 2.5 events per active day

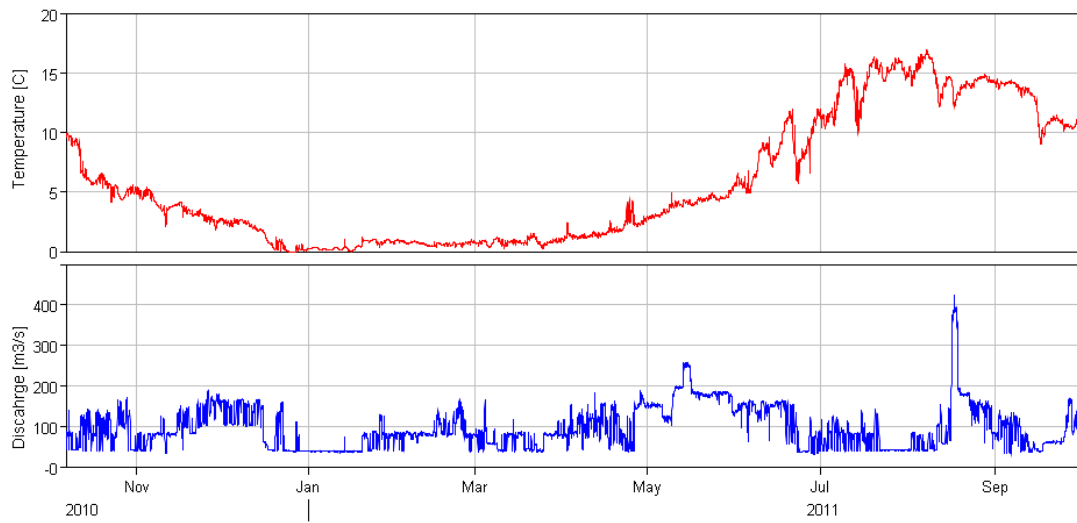


Figure 3-1: Discharge and temperature record at Rathe gauging station for the study period October 2010 through October 2011.

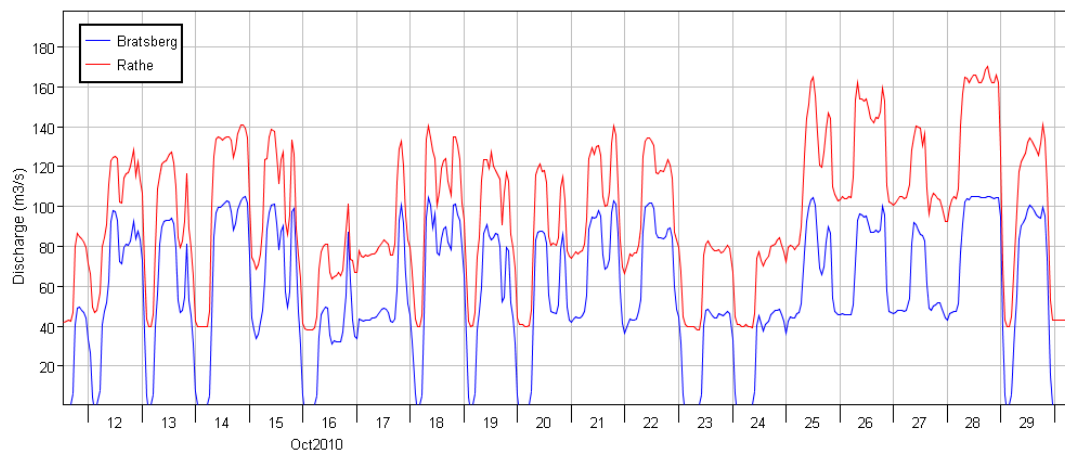


Figure 3-2: Seventeen day example period of discharge through Bratsberg power station (blue) and past the Rathe gauging station (red). Note that major changes in discharge at Rathe are driven by changes in discharge through Bratsberg.

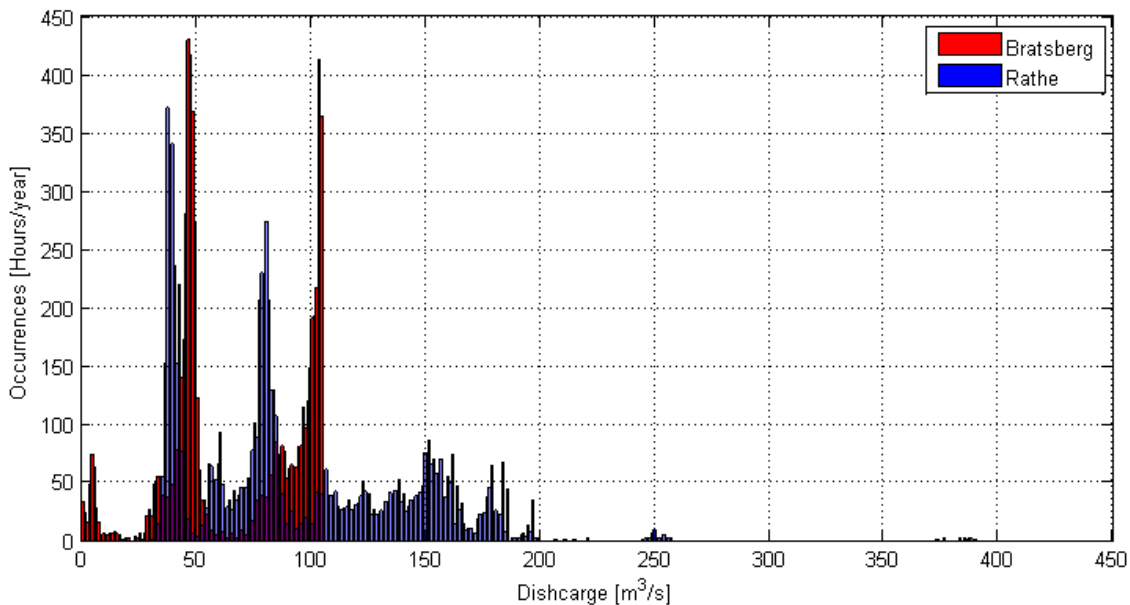


Figure 3-3: Distribution of discharge from the Rathe gauging station and Bratsberg powerstation over one year.

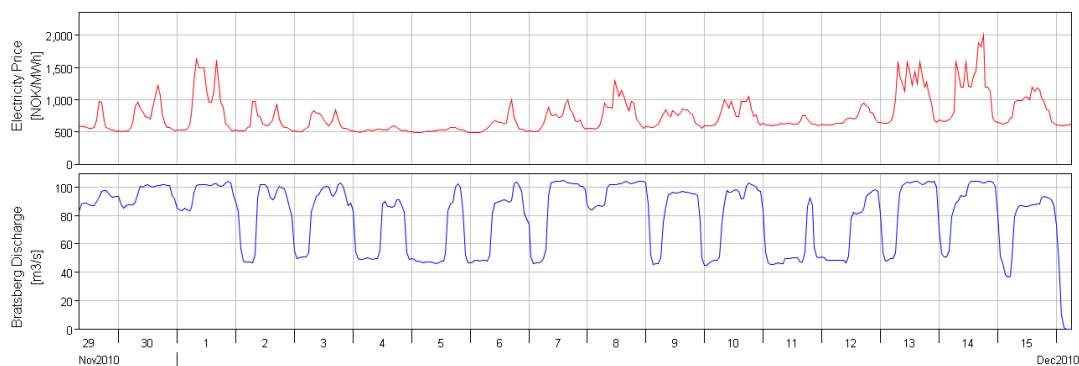


Figure 3-4: Time series of electricity price (Top) in the Trondheim region (Data source: nordpoolspot) and discharge through Bratsberg (Bottom) during October 2010.

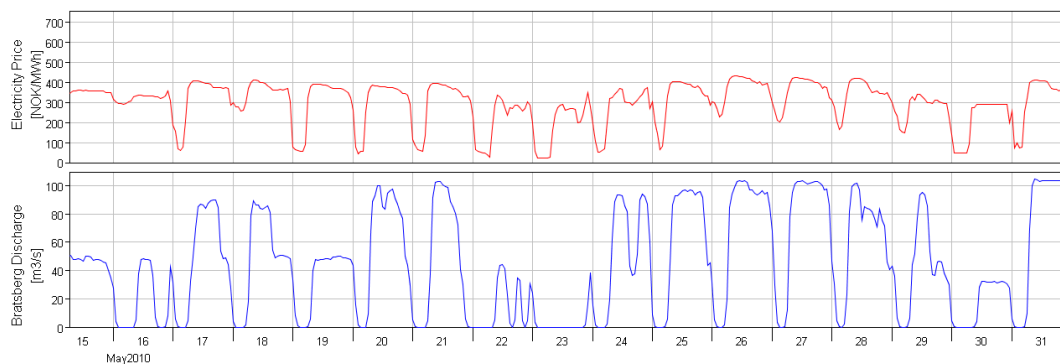


Figure 3-5: Time series of electricity price (Top) in the Trondheim region (Data source: nordpoolspot) and discharge through Bratsberg (Bottom) during May 2011.

with 2.8 and 2.4 events per active weekday and weekend day respectively. The hydropeaking events during the study period have mean, median, and mode values of 34 m³/s, 30 m³/s, and 27 m³/s respectively (Figure 3-6).

Hydropeaking events were further categorized based on hour of occurrence for temporal analysis. Hourly distribution of both rising and falling hydropeaking events occurred with statistically significant bimodal distributions (two tailed, paired sample, t-Test with a null hypothesis of zero difference produced $p < 0.01$) as shown in Figure 3-7. Rising peaks were grouped into two clusters: one in the morning centered on 07:00 and a second, smaller, occurrence in the afternoon centered around 17:00. Falling peaks clustered around 12:00 and 22:00. The events were also classified by weekday or weekend status to explore possible effects that socially driven power demand may have on hydropeaking activity. The statistically significant bimodal distribution persisted in rising and falling hydropeaks for both weekend and weekday events ($p < 0.01$). Rising hydropeaks occurred on average at 6:00 on weekday mornings and 8:00 on weekend mornings, and the difference was significant ($p < 0.01$). There were no significant differences between weekday and weekend rising hydropeaks that centered on 17:00 ($p = 0.53$). The distribution of falling hydropeaking events were not statistically significantly different between weekdays and weekends ($p = 0.52$).

3.1.2 Observations of Thermo peaking

The record of river temperature ranged between 0 and 16 degrees centigrade over the study period (Figure 3-1). Thermo peaks were investigated as event based alterations in river temperature associated with hydropeaking events. Not every hydropeak event produced a severe thermo peaking event, and Figure 3-8 presents the normal distribution of thermal responses to the identified hydropeaking events. Of the 506 identified hydropeaking events, 23% produced thermo peaks with magnitudes less than 0.1 °C, and 65% had magnitudes less than 0.2 °C. Figure 3-9 provides a seasonal context for the thermo peaking responses, by displaying the distribution of thermo peaking responses by season. The 506 hydropeaking events are divided into 231 wintertime, 92 summertime, and 183 combined spring and fall events. Spring and fall events have the smallest magnitudes, and are grouped together as the “shoulder” seasons. The winter and summer events have larger magnitudes, and

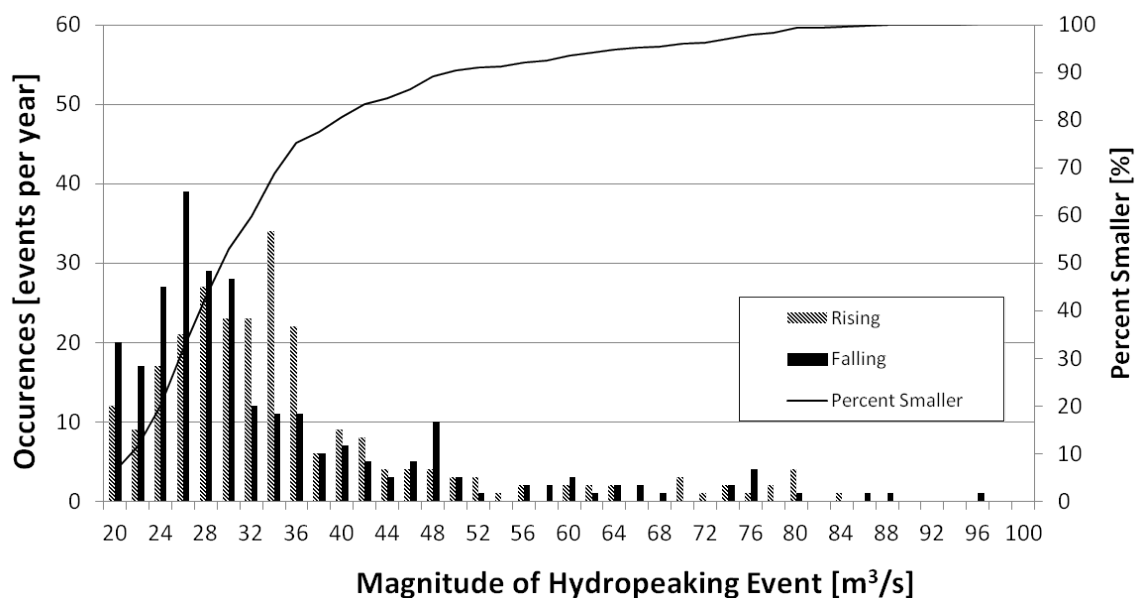


Figure 3-6: Stacked distribution of hydropeaking event magnitude in Bratsberg discharge record over the study period. Average: $34 \text{ m}^3/\text{s}$. Median: $30 \text{ m}^3/\text{s}$. Mode: $27 \text{ m}^3/\text{s}$.

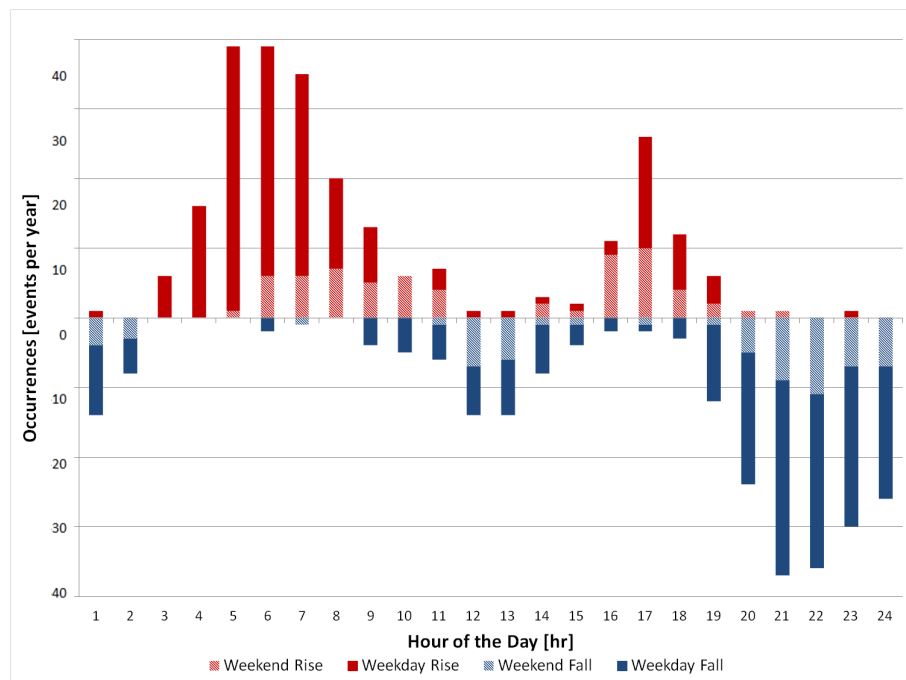


Figure 3-7: Stacked hourly distribution of rising (red) and falling (blue) hydropeaking events greater than $20 \text{ m}^3/\text{s}/\text{hr}$ over the study period. Solid segments indicate weekday events, and hatched segments represents weekend events.

opposite signs in thermo peaking, with winter thermo peaking events warming, and summer events cooling the river downstream of the Bratsberg discharge point.

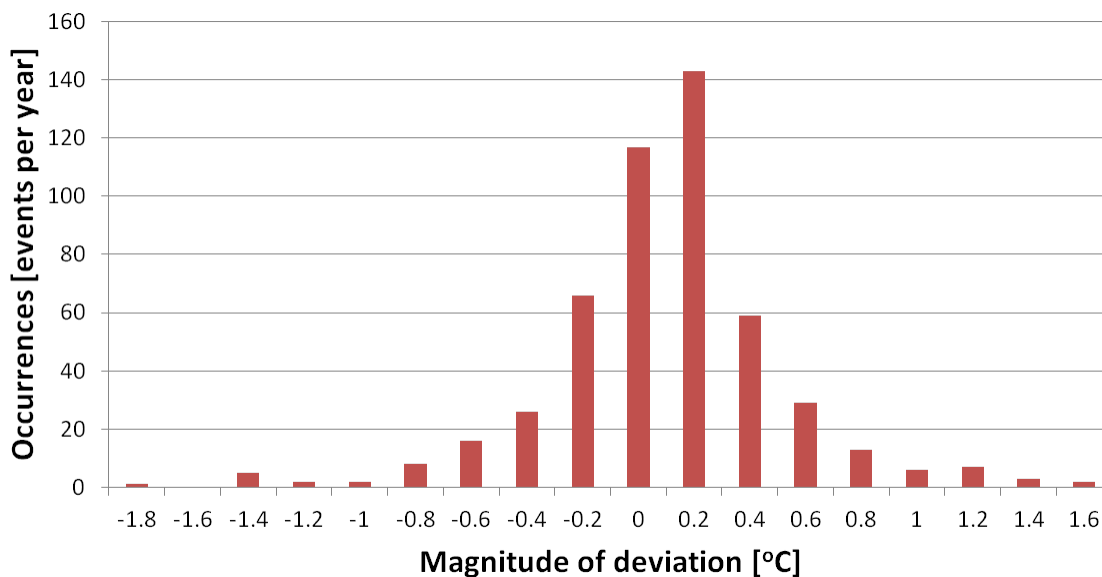


Figure 3-8: Distribution of river temperature changes associated with the 506 observed hydropeaking events.

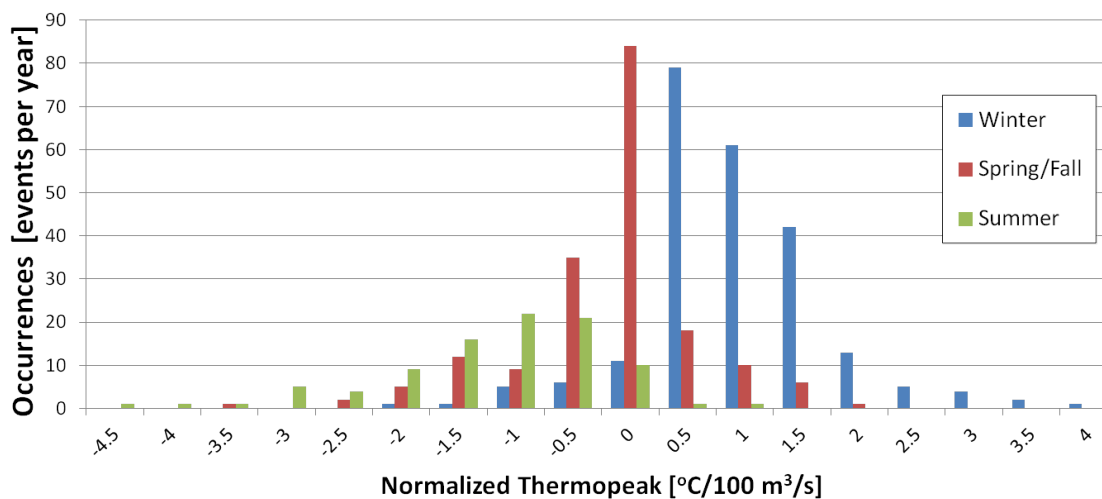


Figure 3-9: Distribution of river temperature changes associated with the 506 observed hydropeaking events separated by season.

The sensitivity of the river to thermo peaking is calculated as the change in temperature

(°C) per 100 unit change in discharge (100 m³/s). This normalized view of thermopeaking highlights the seasonality of thermopeaking, as temperature changes vary directly with discharge in the winter time and inversely in the summertime. Figure 3-10 and Table 3.1 present the findings of the seasonality of thermopeaking. These observations of seasonality concur with other work performed on rivers regulated by reservoirs where thermopeaking seasonality was observed in response to hydropeaking activity (Ward and Stanford, 1979; Zolezzi et al., 2011; Toffolon et al., 2010).

Table 3.1: Seasonality of Thermopeaking in Nidelva, over the hydrologic year 2010.

Year	2010			2011									
Month	Oct	Nov	Dec	Jan	Feb	Mar	Apr	May	Jun	Jul	Aug	Sep	Oct
Normalized Deviation [°C/100 m ³]	0.5	1.3	0.7	0.4	0.4	0.1	-0.8	-0.9	-1.5	-1.4	-0.7	0.1	0.6

As expected, the amplitude of thermopeaking activity observed in Nidelva (Figure 3-8) is small when compared with the thermopeaks of deepwater intake systems, which typically show changes of multiple degrees (Sherman, 2000; Sherman et al., 2007; Toffolon et al., 2010; Carolli et al., 2012). Figure 3-11 shows that there is not an especially high incidence of temperatures at 4 °C at Rathe, as might be expected for a system with a deepwater intake. However, thermopeaking does show itself in this system, illuminating that a deep water intake is not necessary to produce thermopeaking events. The disparate heat fluxes encountered by water in the tunneled and bypass pathways are responsible for the differences in temperature at their confluence.

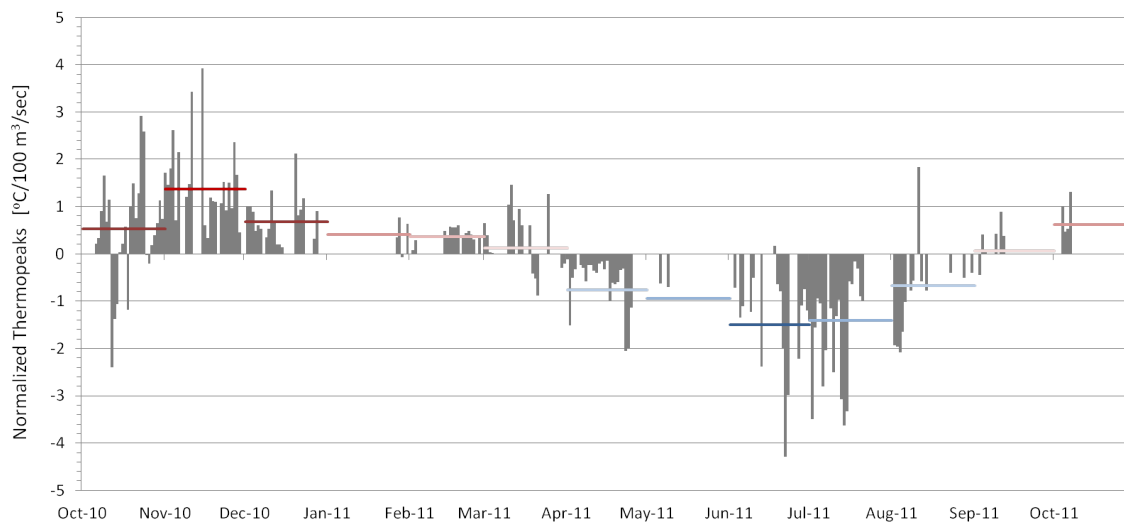


Figure 3-10: Thermoveak magnitude normalized by hydropeak magnitude to present the change in temperature for every one-hundred cubic meter change in discharge. Horizontal bars represent monthly averages, with the color representing the value of the average bars.

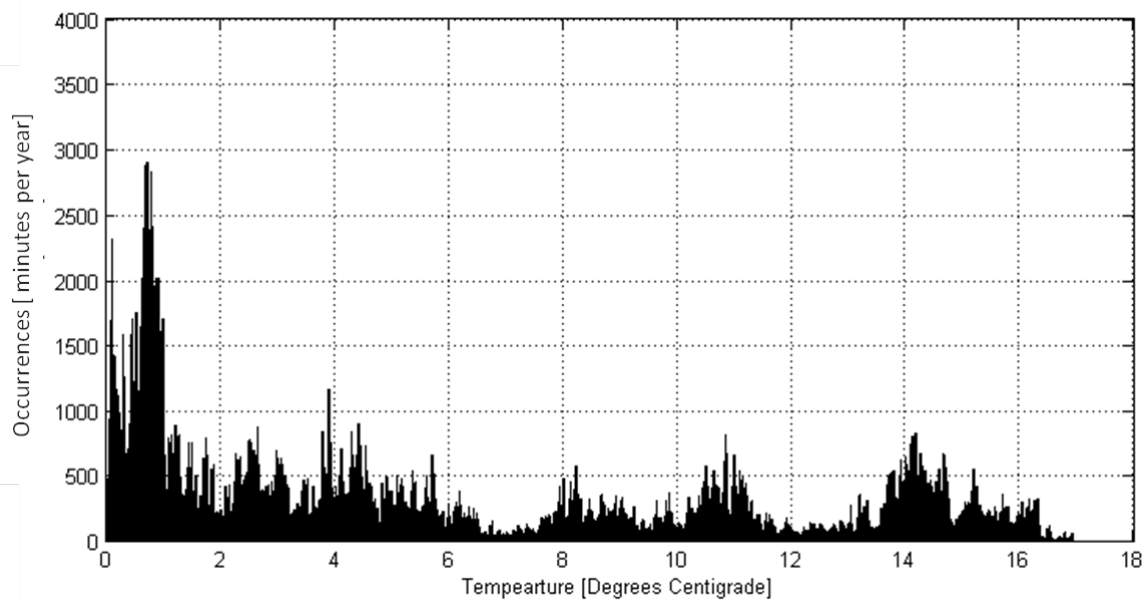


Figure 3-11: Distribution of river temperature over one year.

3.2 HEC-RAS Model Development

3.2.1 Hydrodynamic Calibration

Water lines measured at 43 m³/sec, 90 m³/sec, and 140 m³/sec were used to calibrate Manning roughness coefficients in the hydrodynamic model (Figure 3-12).

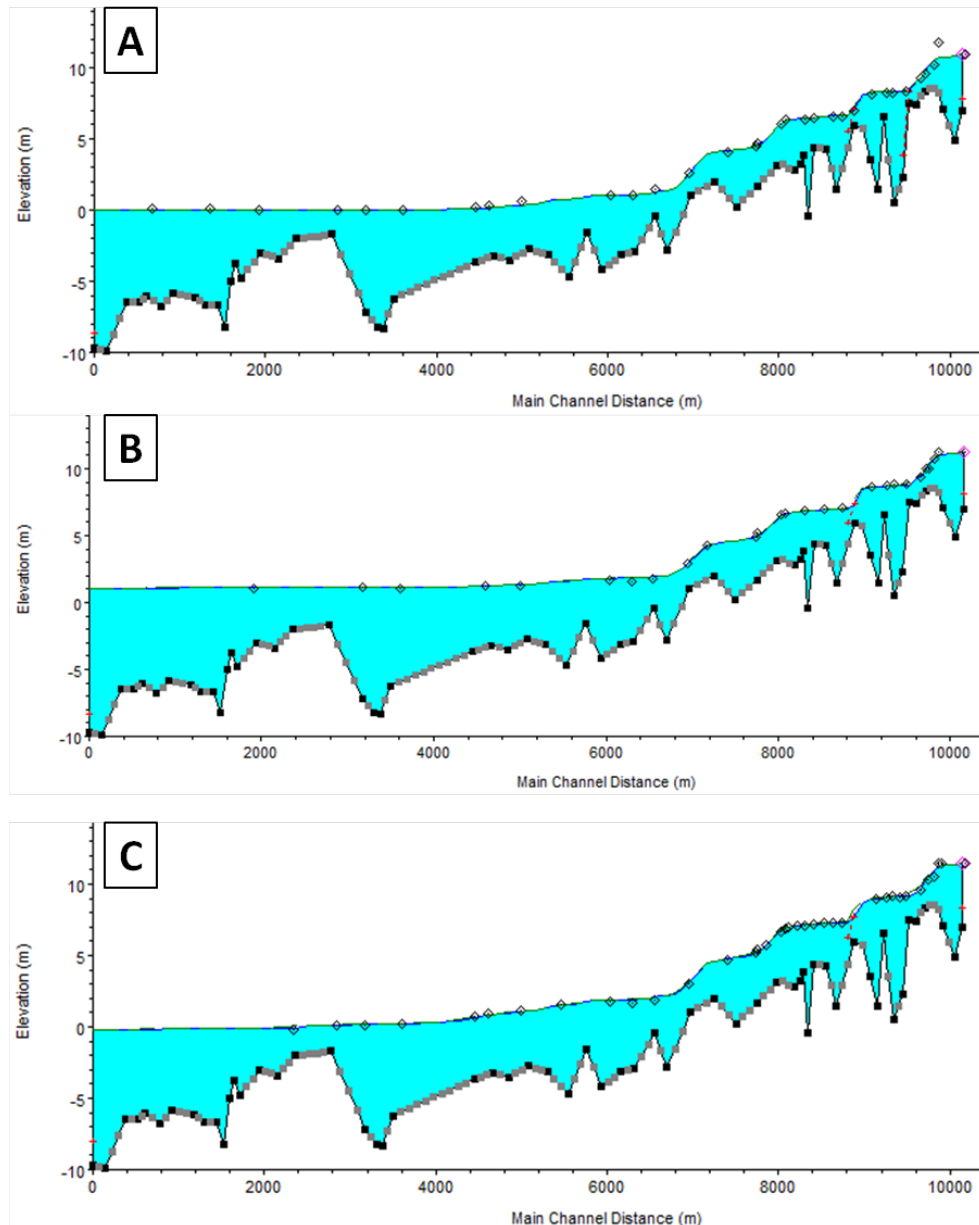


Figure 3-12: Observed (o) and modeled (-) water levels in meters over sea-level [moh] for discharges of 43 m³/sec (A), 90 m³/sec (B), and 140 m³/sec (C).

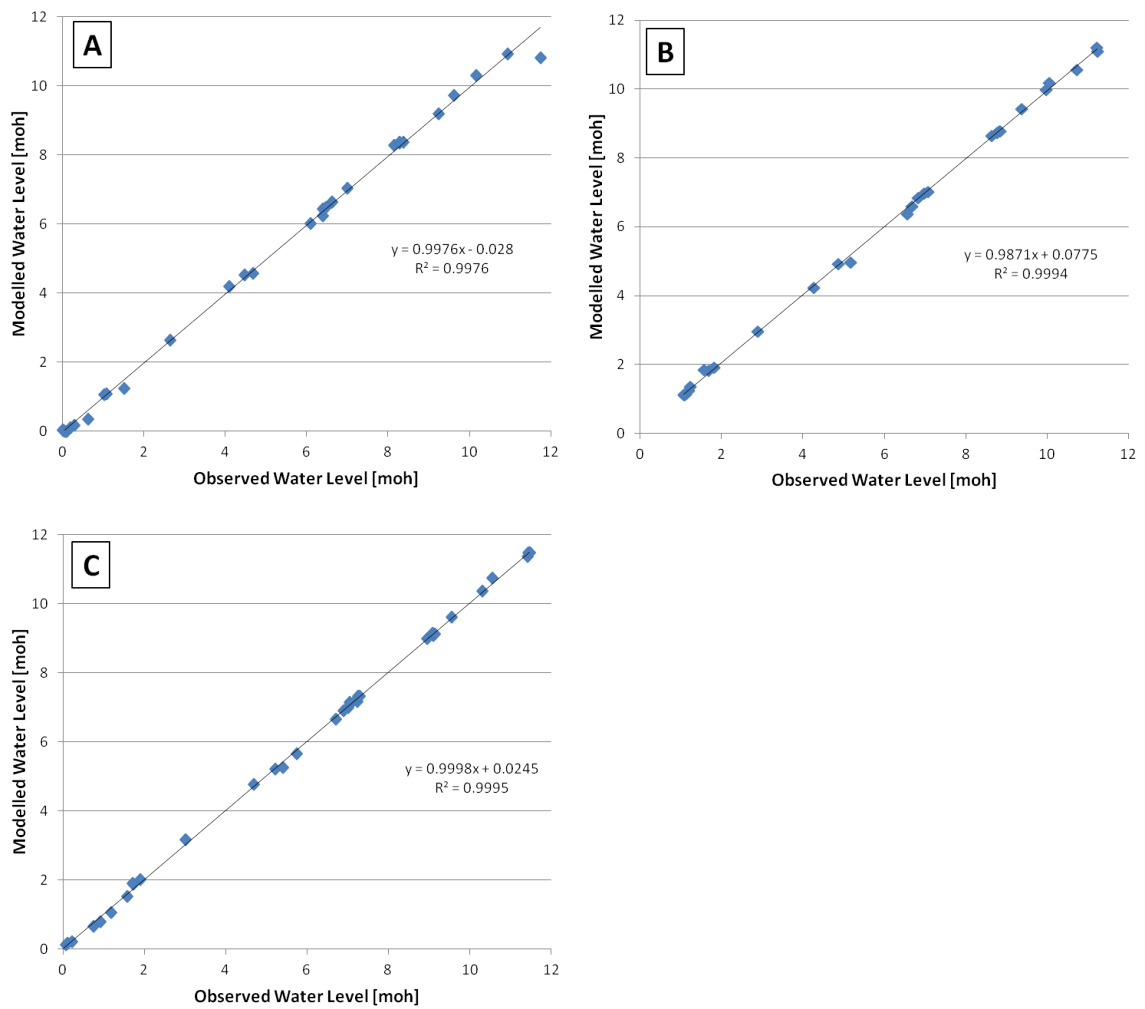


Figure 3-13: Observed and modeled water levels in meters over sea-level [moh] for discharges of 43 m³/sec (A), 90 m³/sec (B), and 140 m³/sec (C).

A single set of roughness coefficients was not sufficient to fully calibrate the hydrodynamic model over the three observed discharge levels and as a result, the decision had to be made to either take a set of roughness coefficients that fit best on average, or to allow the roughness coefficients to scale with flow. The latter approach was adopted and a linear scaling was applied to all the roughness coefficients as shown in Table 3.2.

A comparison between observed and modeled water levels is presented as a series of longitudinal profiles in Figure 3-12 and as a series of scatter plots in Figure 3-13. Roughness coefficients are used to incorporate all energy losses including bridges, vegetation, and boulders. Because obstructions like bridges are not included in the geometric data, and energy losses around these structures are incorporated in the roughness coefficient, roughness coefficients can fall outside the expected natural range of around 0.01. Figures 3-14 and 3-15 display the calibrated Manning roughness coefficients distributed along the study reach. Note that rapids and bridges required high roughness values, while pools were calibrated to have lower roughness coefficients.

Table 3.2: Discharge based scaling parameters applied to roughness coefficients.

Discharge	Roughness Factor
30	2
90	1.3
150	1
200	1

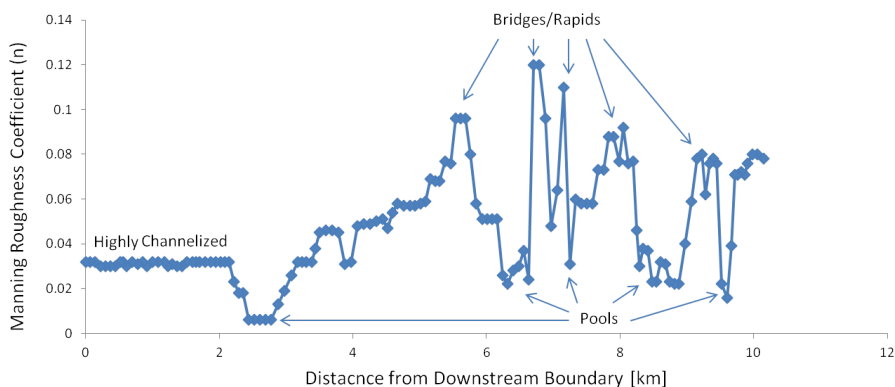


Figure 3-14: Calibrated Manning roughness coefficient values along the study reach.

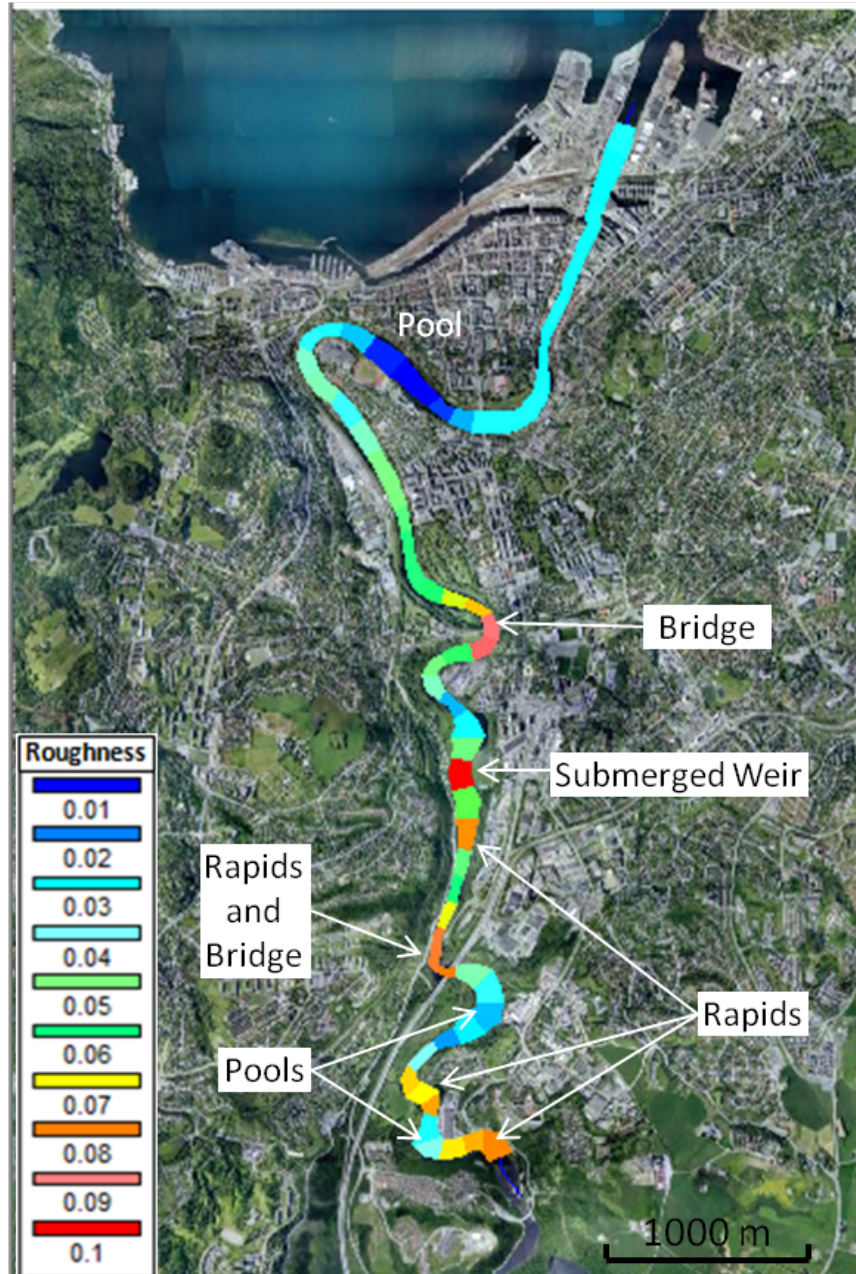


Figure 3-15: Overview map of calibrated Manning roughness coefficient values along the study reach.

For the highly channelized section of the model with steep banks of sheet pilings and building foundations, some modeled water levels rose past the vertical extent of the measured cross sections. In this section of the river, geometry was only taken for the river bed and HEC-RAS vertically extended the outermost points in the cross sections to keep the water column entirely above the reported riverbed (Figure A.4 in Appendix A).

3.2.2 Energy Balance Calibration

Calibration of the energy balance model produced values reported in Table 3.3.

Table 3.3: Energy balance model parameters. Ranges provided by HEC-RAS user manual.

Parameter	Applicable Equation	Suggested Range	Calibrated Value
Dust Coefficient	A.1	0.0 - 0.2	0.0
Diffusivity Ratio	A.5	0.9 - 1.1	1.5
Wind Function	<i>a</i>	$\sim 10^{-6}$	0
	<i>b</i>	$\sim 10^{-6}$	10^{-6}
	<i>c</i>	~ 1	0.5

The calibrated model produced temperatures with a coefficient of determination of 0.9969 between observed and modeled temperatures at the midstream and downstream locations (Figures 3-16 and 3-17). Calculated model residuals are reported in Table 3.4 and displayed in Figure 3-18. The model error was positively biased from the upstream to the midstream locations, and slightly negatively biased from the midstream to the downstream locations. The total observed accumulations of heat over the calibration period was 530 and 526 degree days at the midstream and downstream locations respectively. The model output for these two locations was 532 and 516 degree days, resulting in cumulative deviations of +2 degree days for the midstream location, and -10 degree days for the downstream location (Figure 3-16).

The calibration period had an minimum, average, and maximum residual of -0.85 °C, -0.089 °C, and +1.26 °C for the midstream location, and -1.01 °C, -0.039 °C, and +1.69 °C for the downstream location as presented in Table 3.4 and Figure 3-18.

Table 3.4: Calibration and verification residuals from the energy balance model at the midstream and downstream locations.

Location	Calibration Residuals [°C]				Verification Residuals [°C]			
	Min.	Mean	Max.	St. Dev.	Min.	Mean	Max.	St. Dev.
Downstream	-1.01	-0.039	1.69	0.12	-0.66	0.05	0.69	0.14
Midstream	-0.85	0.089	1.26	0.10	-0.49	-0.026	0.51	0.11

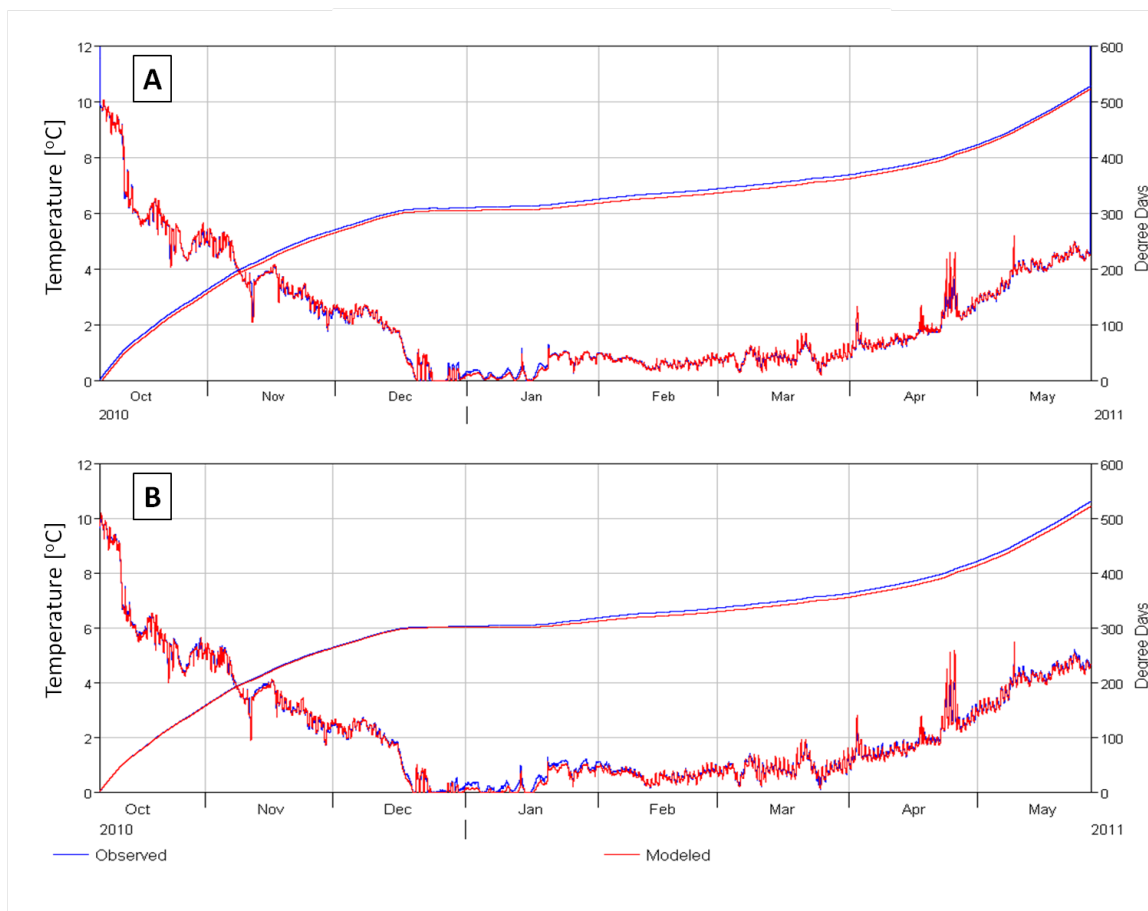


Figure 3-16: Observed (blue) and modeled (red) temperature records (left axis) and degree day accumulation curves (right axis) for midstream (window A) and downstream (window B) locations for the calibration period October 2010 through September 2011.

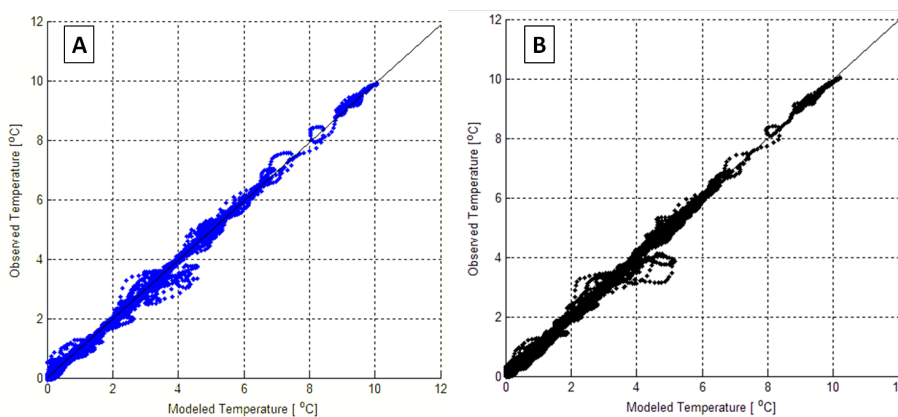


Figure 3-17: Results of the calibration process at the midstream (A) and downstream (B) locations.

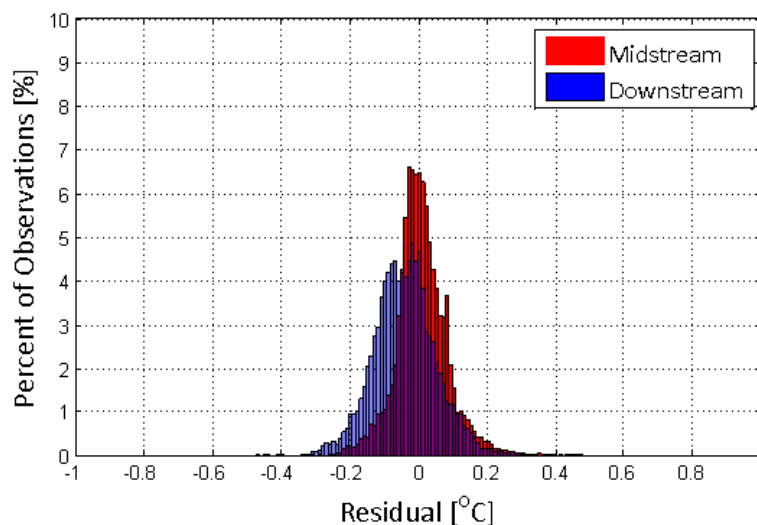


Figure 3-18: Overlaid histograms of model residuals for the midstream (red) and downstream (blue) locations for the calibration period of 7 October 2010 through 27 May 2011.

3.2.3 HEC-RAS Model Verification

The verification model runs produced temperatures with a coefficient of determination of 0.9960 between observed and modeled temperatures at the midstream and downstream locations (Figures 3-19 and 3-20). Calculated model residuals are reported in Table 3.4 and displayed in Figure 3-21 as presented in Table 3.4 and Figure 3-21. The model error during the verification period was negatively biased from the upstream to the midstream locations (-0.03), and positively biased from the midstream to the downstream locations (+0.05). The total observed accumulations of heat over the verification period was 500 and 496 degree days at the midstream and downstream locations respectively. The model output for these two locations was 499 and 498 degree days, resulting in cumulative deviations of -1 degree days for the midstream location, and -2 degree days for the downstream location over the two month long verification period (Figure 3-19). The performance of the model under the verification process is bolstered by the differences in season, and climatic conditions for which the model was calibrated and verified. The calibration process was performed for winter, spring, summer, and early fall for a year with record cold air temperatures and record low precipitation (Figure A.4), while the verification process was performed on a record from the fall of a warm, especially wet year (Figure 1-2).

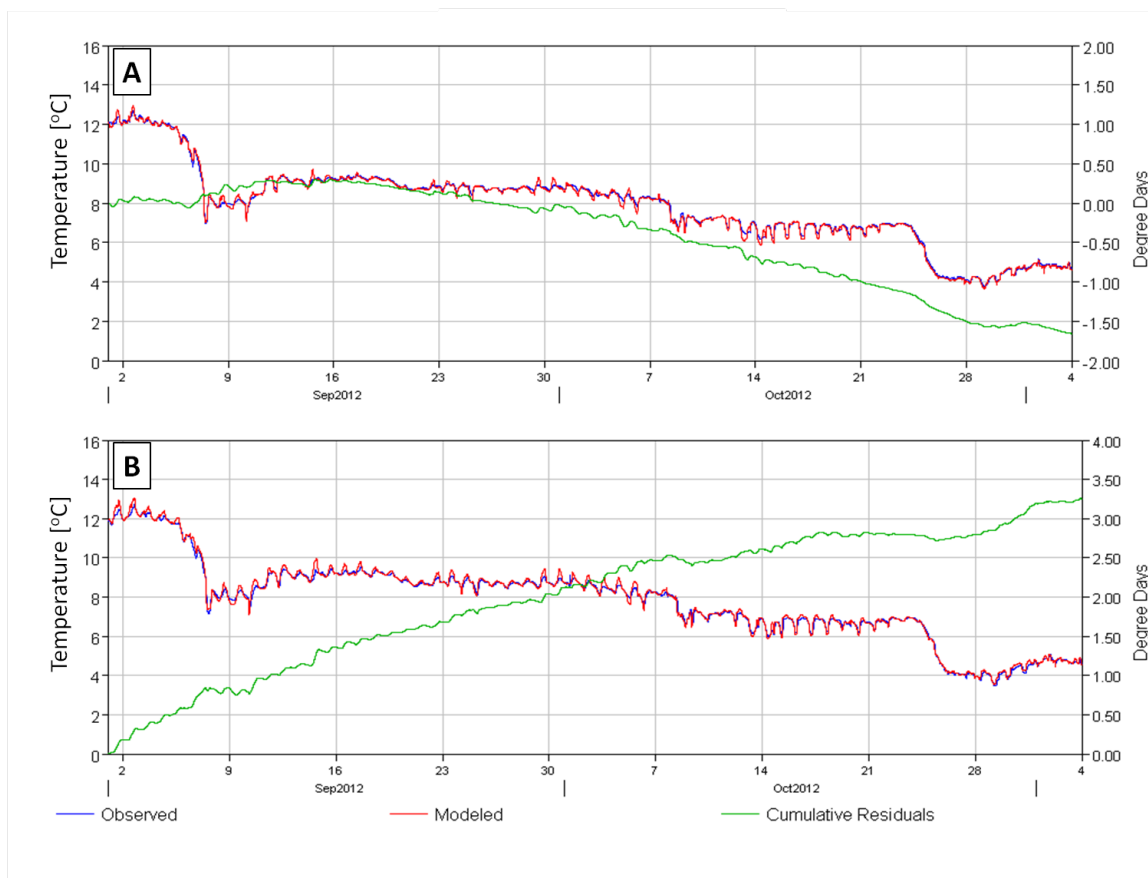


Figure 3-19: Time series of modeled (red line) and observed (blue line) temperatures and cumulative deviation (green line) at the midstream (window A) and downstream (window B) locations for the verification period, September through October 2012. Temperatures are plotted against primary y-axis, and cumulative deviations against the secondary y-axis on the right.

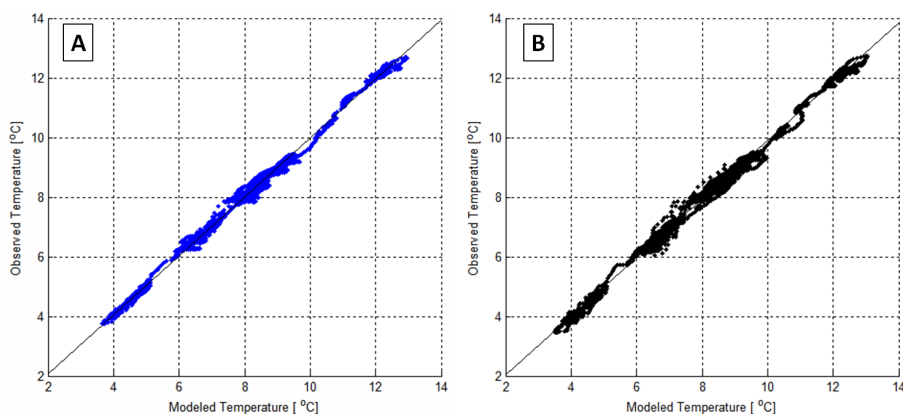


Figure 3-20: Results of the verification process at the midstream (A) and downstream (B) locations.

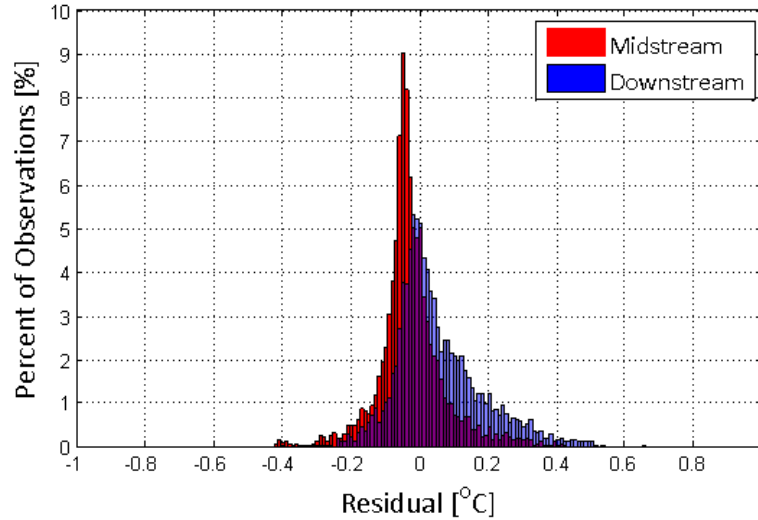


Figure 3-21: Overlaid histograms of model residuals for the midstream (red) and downstream (blue) locations for the calibration period of 7 October 2010 through 27 May 2011.

3.2.4 Parameter Sensitivity

Results from the parameter sensitivity process are reported in Table 3.5.

Table 3.5: Relative sensitivity of energy balance model to each model parameter across the observed range of parameter values.

Driving Parameter [units]	Min.	Mean-1 σ	Mean	Mean+1 σ	Max.	Relative Sensitivity
Air Pressure [mb]	961	996	1008	1020	1036	1.8E-3
Air Temperature [°C]	-17.0	-2.6	5.2	13.0	26.8	4.5E-2
Relative Humidity [%]	23	60	75	90	100	2.1E-2
Solar Radiation [W/m ²]	0.0	31.5	63	191	704	4.7E-2
Cloud Cover [0-1]	0.0	0.34	0.66	0.98	1.0	2.6E-2
Wind Speed [m/s]	0.0	0.91	2.68	4.45	13.8	4.5E-3
Discharge [m ³ /s]	40	48	96	143	257	-1.8E-2
Sea Level [m]	-1.86	-0.74	0.0	0.74	2.3	0.0
Calibration Parameter	Min.	25%	Mean	75%	Max.	Relative Sensitivity
Dispersion Coefficient	0.01	1.03	2.05	3.07	4.09	1.3E-5
Wind Parameter a	0.0	0.75	1.5	2.25	3.0	2.5E-3
Wind Parameter b	0.0	0.75	1.5	2.25	3.0	6.8E-3
Wind Parameter c	0.0	0.5	1.0	1.5	2.0	5.0E-3
Kh/Kw	0.5	0.75	1.0	1.25	1.5	8.1E-3

Air temperature and solar radiation are the two most influential driving parameters. This dominant relationship is displayed in Figure 3-22 as the data sets with the largest change in water temperature over the observed range of parameter values. The calibration parameters are seen to have much smaller relative and absolute sensitivity, as seen in Table

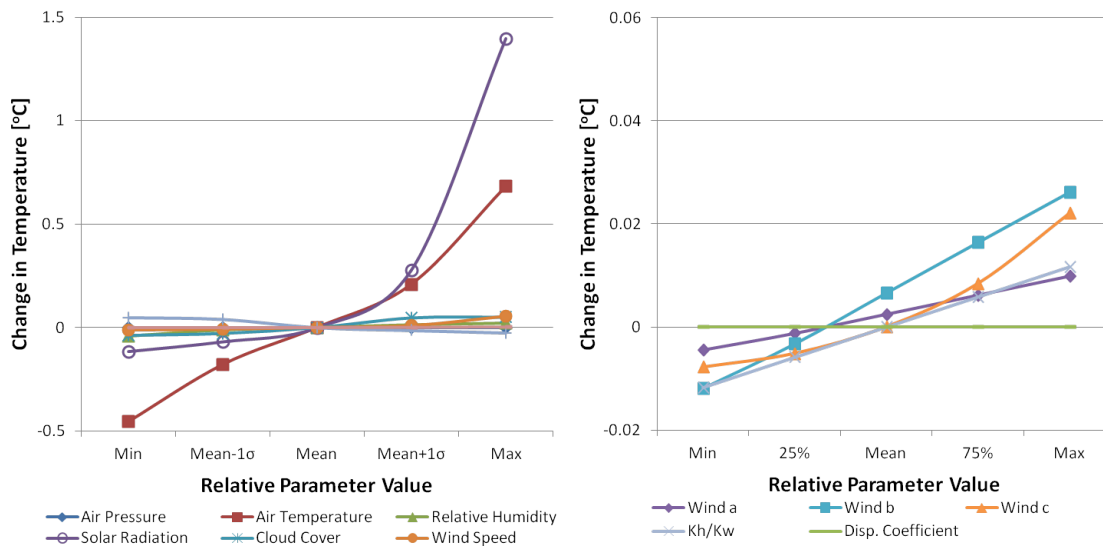


Figure 3-22: Change in temperature for each relative parameter value. Left: Driving parameters. Right: Calibration parameters. Note the different scales.

3.5, and Figure 3-22 when compared to the driving parameters, with wind parameter b and the diffusivity ratio having the greatest influence of the five calibration parameters.

The energy balance model was calibrated using the available parameters, yet there were periods when model results were different from observations. A compromise was struck between over-fitting the model to reproduce the observations for the study period, and keeping the model broad enough to accurately forecast future scenarios. Some potential reasons for deviations between observed and modeled temperatures are: unmodeled overland or tributary flow, unmodeled heat flux through precipitation, wind patterns at the river surface that differ from those reported at the meteorologic station, atmospheric inversion in the river valley that affect the lapse rate near river level, topographic shading, and any thermal interaction with the river bed. Within the bounds of the energy balance model, all possible parameters were calibrated to fit the model to observed temperature records.

3.3 Transport of Thermopeaks

The calibrated hydrodynamic and thermodynamic model were able to simulate downstream transport of thermopeaks, as shown in Figure 3-23. The arrival times of thermopeaking events at the downstream location, six kilometers downstream of the upstream location,

are used to demonstrate that the hydrodynamic model is well calibrated, while the magnitude of the thermopeak attenuation demonstrates that the energy balance model is well calibrated. The duration of thermopeaks changes little between the upstream and downstream locations, indicating that thermopeaks are transported conservatively, and that there is little longitudinal dispersion of heat.

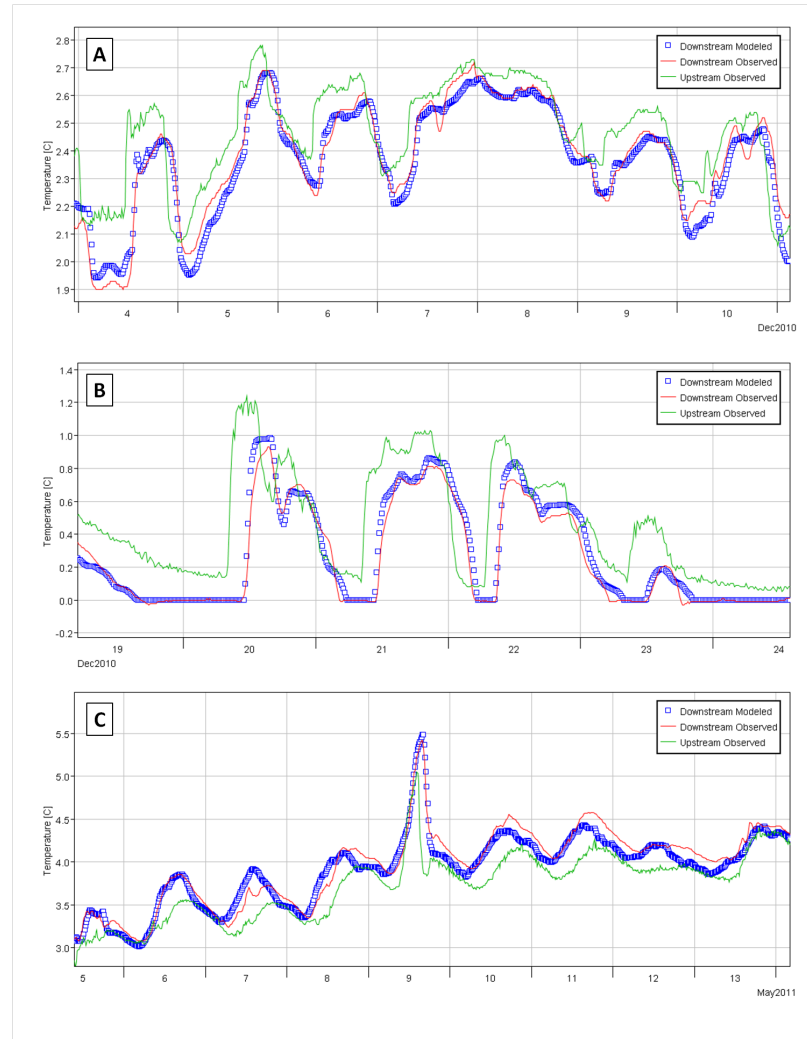


Figure 3-23: Observed temperature records at the upstream (green line) and downstream locations (red line) and modeled temperature results for the downstream location (blue boxes) from the calibration period. A: December 4th through 10th 2010. B: December 19th through 24th 2010. C: May 5th through 13th 2011.

3.4 Future Discharge Scenarios

3.4.1 HEC-RAS Model Results

Modeled temperature records for the Downstream location under the three proposed scenarios are presented in Figure 3-24. Values are reported for the downstream temperature logger location as this is the greatest distance downstream free from tidal influences. Degree days were used to represent the integral of temperature with respect to time.

The FullSpring and FullSummer discharge scenarios produce similar temperature records, accumulating heat on nearly identical schedules. The Dynamic2006 discharge scenario produced a peaking temperature record, evidence of low flows in the early summer only experienced by the dynamic strategy as the seasonal strategies were both discharging at full capacity. Deviations from the downstream base case temperature record are presented in Figure 3-25 as temperature deviation on the primary y-axis, and cumulative difference in degree days on the secondary y-axis. All three discharge scenarios are similar for the first three months of the study period, but in the end of December the Dynamic2006 scenario begins to introduce more heat to the system than the other scenarios as warmer water from the reservoir was released in pulses that corresponded with periods of low wind power production. This trend continued through the winter. In spring the discharge was raised to maximum capacity under the FullSpring scenario, and the resulting temperature record continued to be lower than observed as reservoir water was routed directly to the study reach, missing warming heat fluxes along the bypass reach. Alternatively, the water in the bypass reach under the FullSummer scenario between April 1 and May 1 experienced warming from increased air temperature. The low flows in Nidelva allowed this heating to continue in the study reach, and heat accumulated at the downstream site more rapidly than under observed conditions. At the beginning of June the discharge from the reservoir picked up and river temperatures decreased, accumulating heat at the same rate as the FullSpring scenario until July 7th when the FullSpring scenario is simulated to have emptied the reservoir. The Dynamic2006 scenario is the only one that allows for minimum flow from the beginning of June through the 7th of July, allowing for much higher temperatures to exist in the temperature record for this scenario for this period. The FullSummer sce-

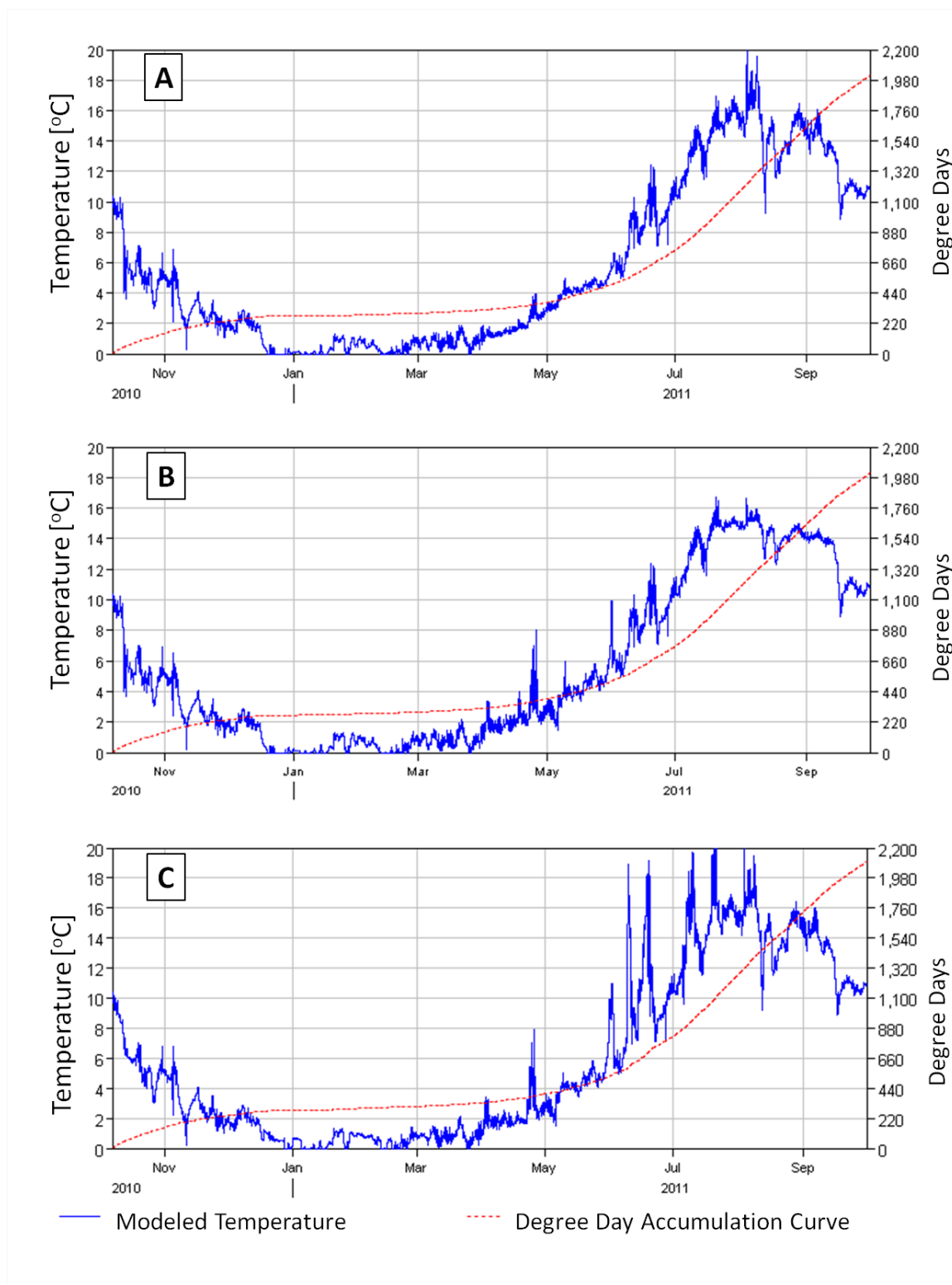


Figure 3-24: Modeled downstream temperature (blue solid line) for FullSpring (A), Full-Summer (B), and Dynamic2006 (C) scenarios. Degree day curves (red dashed line) are plotted against the secondary y-axes.

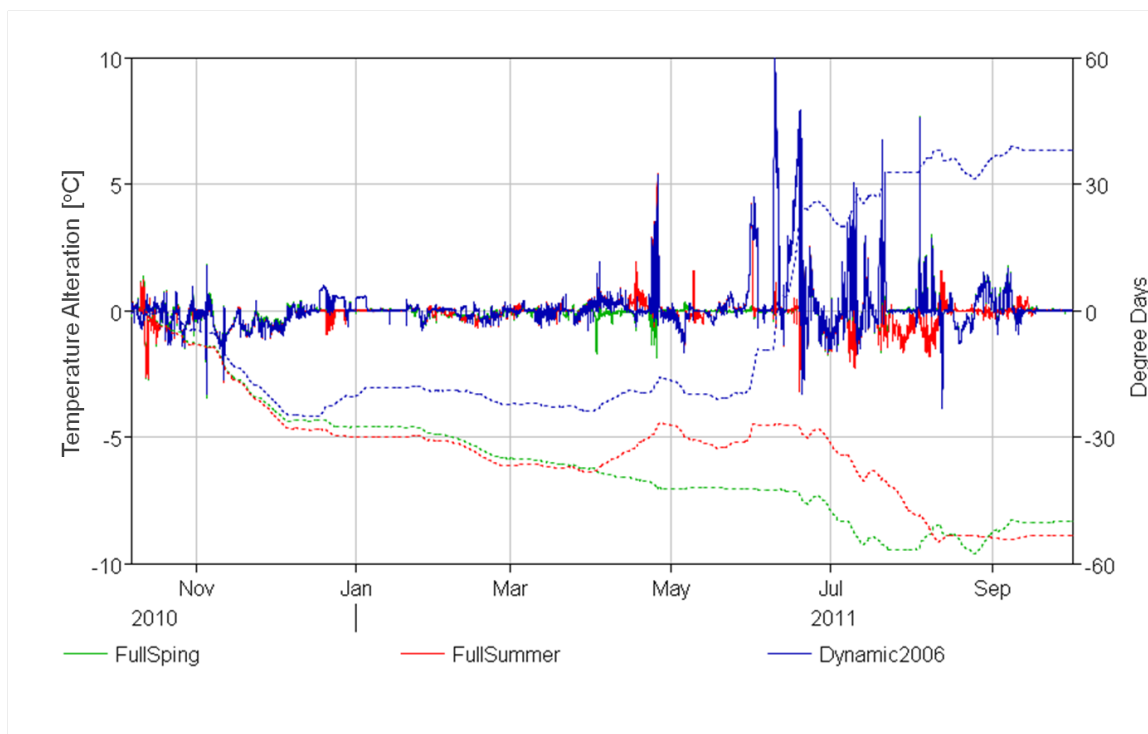


Figure 3-25: Difference between observed and modeled temperature at the downstream location for the FullSpring (green solid line), FullSummer (red solid line), and Dynamic2006 (blue solid line) scenarios. Cumulative deviations (dashed lines) are plotted against the secondary y-axes.

nario is simulated to decrease to minimum flow on the 9th of September, at which point the temperature accumulation of heat is the same as for the FullSpring scenario and the degree days curves are parallel.

3.4.2 Potential Impacts

The impacts of these new temperature records were estimated with two considerations: fish development and potential for ice formation. The first was approximated with the Crisp model, and the latter assessed from the output of the energy balance model. The results from the proposed scenarios were compared to baseline analysis performed on observations from the 2010 hydrologic year.

Crisp Model Results

The Crisp model, using water temperature as its only driving parameter, was fed the output from the energy balance model to calculate hatching dates associated with each discharge scenario. In each case the spawning date was held at November 5th. The resulting development curves are shown in Figure 3-26, and the alterations to hatching and swim-up dates are presented in Table 3.6. As the Crisp model is essentially a transformed version of degree-day accumulation, it is informative to look at the various degree-day accumulation curves produced for the various discharge scenarios (Figure 3-25).

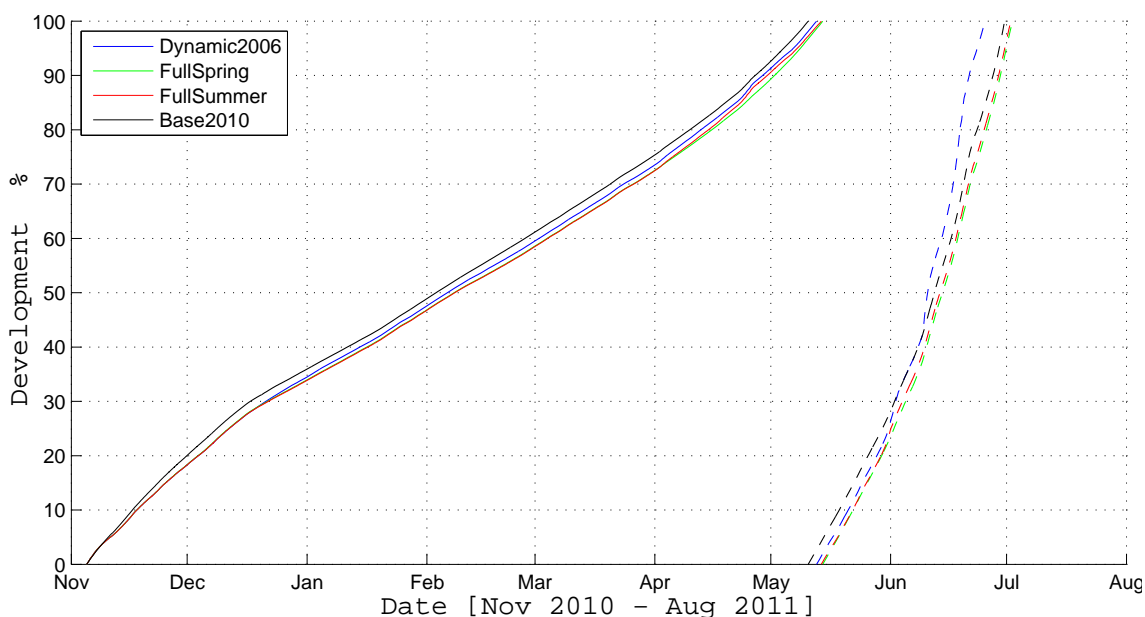


Figure 3-26: Egg (solid lines) and alevin (dashed lines) development for the Base2010 (black), FullSpring (green), FullSummer (red), and Dynamic2006 (blue) scenarios.

Table 3.6: Crisp model results: impact of discharge scenarios on salmon development.

Scenario	Hatch Date	Alteration in Hatch Date	Swimup Date	Alteration in Swimup Date
Base2010	10 May	-	30 Jun	-
FullSpring	14 May	+4 Days	2 Jul	+2 Days
FullSummer	14 May	+4 Day	2 Jul	+2 Days
Dynamic2006	12 May	+2 Days	25 Jun	-5 Days

Modeled egg development was seen to vary by four days between scenarios from the 10th of May in the base case through the 14th of May in the FullSpring and FullSummer scenarios. For the FullSpring and FullSummer scenarios, flows were reduced in the winter months, leaving Nidelva vulnerable to heat fluxes during the coldest time of the year. The river temperatures dropped to equilibrate with the atmosphere during egg development, producing a four day delay in the hatch date. In the Dynamic 2006 scenario, flows were periodically raised above the minimum flow requirement. This kept river temperatures between the base case and the other model scenarios and resulted in only a two day delay in the hatching date.

Swim-up development was seen to vary by eight days between scenarios from the 25th of June in the Dynamic2006 scenario through the 2nd of July in the FullSpring and FullSummer scenarios. The accelerated alevin development seen for the Dynamic2006 scenario is attributable to three warming events that occurred in late May, early June, and late June seen in Figure 3-25 as the rapid rise in degree day accumulation for the Dynamic2006 scenario. These three periods of warming coincide with periods of high wind-power production as seen in Figure 2-17 and the corresponding low discharge from the Bratsberg power station as seen in Figure 2-18. With discharge lowered to the minimum flow requirement of 40 m³/s for these summertime periods, the river was susceptible to heat fluxes and the temperature rose to equilibrate with the atmosphere.

Ice Formation Potential

Ice formation is problematic for Nidelva as ice breakup could cause damage to boats and docks anchored in the lowest few kilometers of the river (Fremstad and Thingstad, 2007). The water quality component of HEC-RAS is limited to positive water temperatures and does not simulate ice formation due to the stratified nature of ice formation, and HEC-RAS's assumption of homogeneity within a water quality cell (Brunner, 2010). The potential for ice formation was estimated with simple criteria of super cooled water (0 °C), air temperatures less than -6 °C, and a negative heat flux greater than -100 Watts/m² (Daly, 1991). These criteria were met between the 19th of December and the 24th of February, when the FullSpring and FullSummer are identical, and therefore the ice formation potential is also

identical. The Base2010 discharge scenario met the ice formation potential criteria for a total of 5.8 days over a series of 9 events ranging from 1.75 hours to 3.6 days in duration. The FullSpring and FullSummer scenarios increased the total duration to about 10 days, over a series of 19 events ranging from 1.0 hour to 4.4 days in duration. The Dynamic2006 scenario decreased the total to 2.6 days over a series of 10 events ranging from 1.5 hours to 19 hours. Table 3.7 presents the results from the ice formation potential estimates.

Table 3.7: Ice formation potential for observed and simulated discharge scenarios.

Event	Base 2010	FullSpring and FullSummer	Dynamic2006
Count [num.]	9	19	10
Latest Event	4 Jan.	24 Feb.	24 Feb.
Duration	Min. [hrs]	1	1.5
	Max. [hrs]	86	19
	Mean [hrs]	15	6
	Median [hrs]	5	5
Sum [days]	5.8	10.3	2.6
Change [days]	-	+4.5	-3.2

3.5 Simulating a Deepwater Intake

The same discharge scenarios were simulated with an upstream boundary condition that reflects the input heatflux that would be expected if the Bratsberg intake were located below the thermocline in Selbusjøen. The resulting simulated temperature as well as degree day accumulation are shown for the downstream location in Figure 3-27. The observed degree day accumulation curve is included in each plot to demonstrate the impact each simulation has on annual temperature trends. The simulations performed with the current intake structure are referred to as the original simulation series. The impact that the Deepwater intake has on river temperature is analyzed by comparing the original and Deepwater temperature records generated with the Base2010 discharge scenario (Figure 3-28). The influences of the various discharge scenarios within the Deepwater scenario are shown in Figure 3-29.

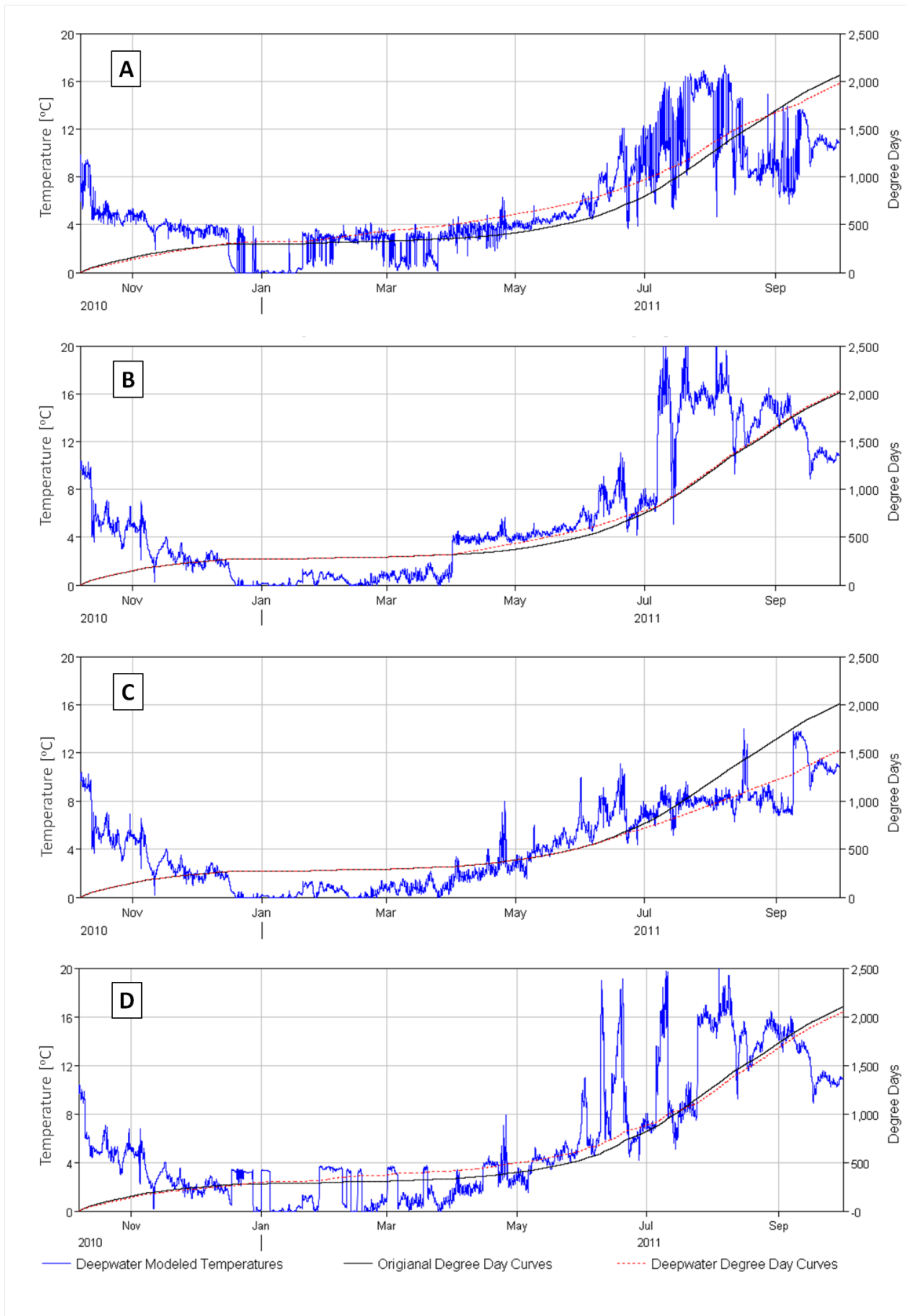


Figure 3-27: Modeled downstream temperature (blue solid line) for Base2010 (top) Full-Spring (upper middle), FullSummer (lower middle), and Dynamic2006 (bottom) scenarios. Degree day curves for the Deepwater simulations (red dashed line) and original simulations (solid black line) are plotted against the secondary y-axes.

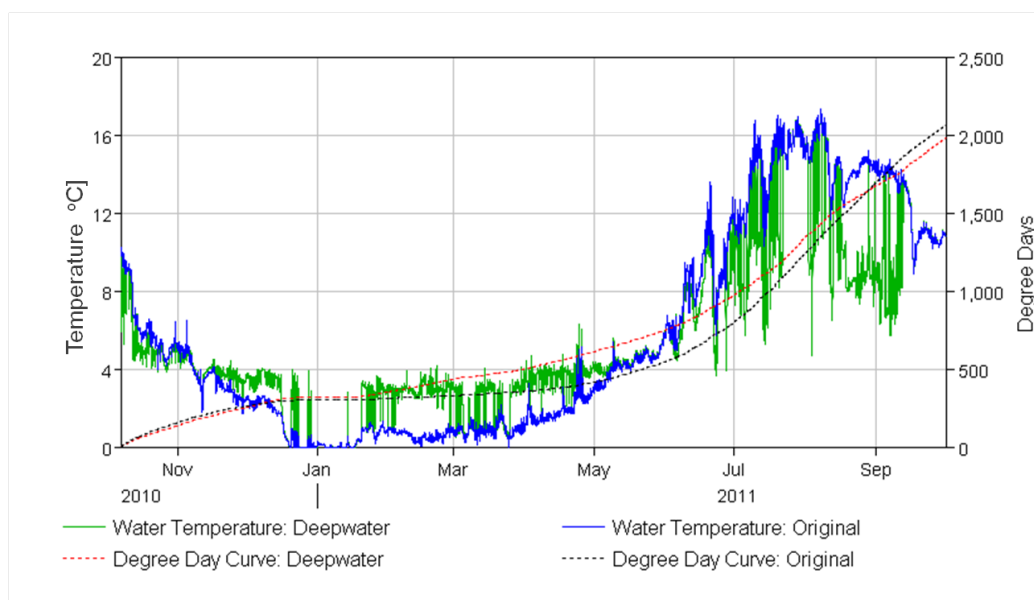


Figure 3-28: Modeled downstream temperature under original (blue solid line) and Deepwater (green solid line) simulations. Degree day curves for the Deepwater simulations (red dashed line) and original simulations (solid black line) are plotted against the secondary y-axes.

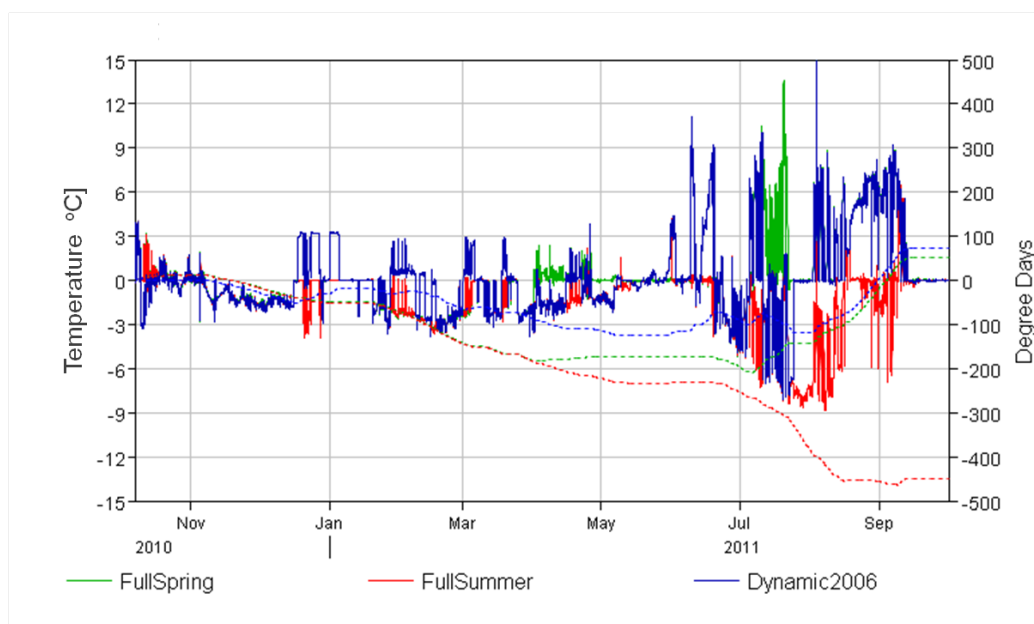


Figure 3-29: Alterations in temperature at the downstream location under the Deepwater scenario for the FullSpring (green solid line), FullSummer (red solid line), and Dynamic2006 (blue solid line) scenarios. Cumulative deviations (dashed lines) are plotted against the secondary y-axes.

3.5.1 Crisp Model Results: Deepwater

The biological implications of these Deepwater scenario temperature records are estimated with the Crisp model. The results are presented in Table 3.8 and Figure 3-30.

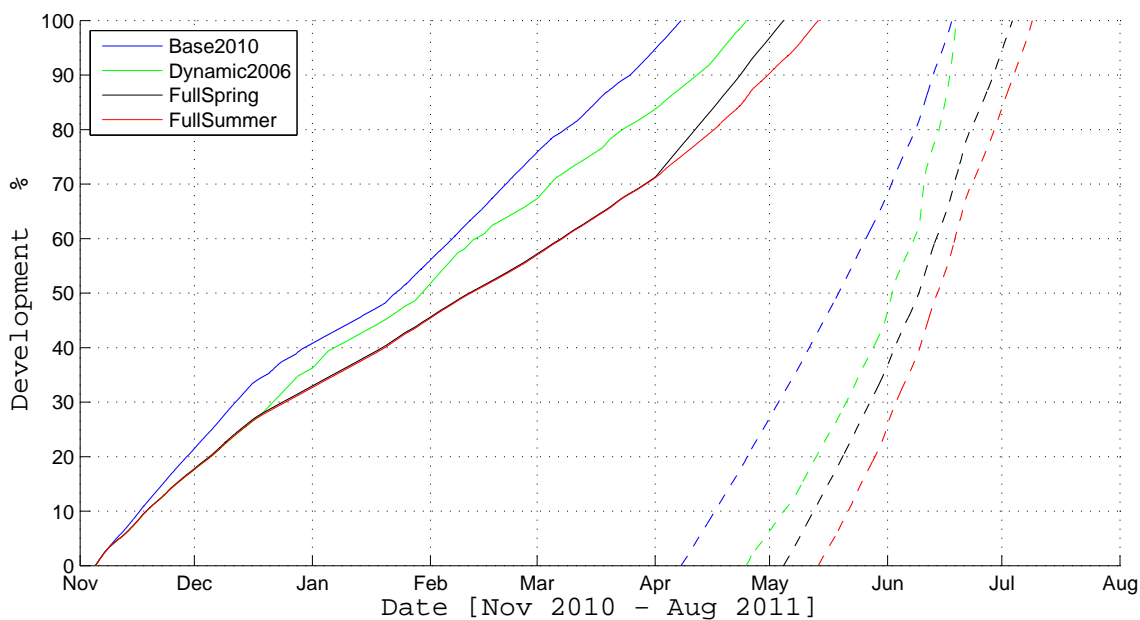


Figure 3-30: Egg (solid lines) and alevin (dashed lines) development for the Base2010 (black), FullSpring (green), FullSummer (red), and Dynamic2006 (blue) scenarios under the Deepwater simulation.

Table 3.8: Crisp model results: impact of discharge scenarios on salmon development under simulation of a deepwater intake.

Scenario	Hatch Date	Alteration in Hatch Date	Change From Original	Swimup Date	Alteration in Swimup Date	Change From Original
Base2010	7 Apr	-	-33 Days	17 Jun	-	-13 Days
FullSpring	4 May	+27 Days	-10 Days	3 Jul	+16 Days	+1 Day
FullSummer	13 May	+36 Days	-1 Day	9 Jul	+22 Days	+7 Days
Dynamic2006	24 Apr	+17 Days	-20 Days	19 Jun	+2 Days	-16 Days

3.5.2 Ice Formation Potential: Deepwater

Ice development potential was estimated with the same criteria as for the original simulations and the results are presented in Table 3.9. The influence of the various discharge scenarios is analyzed as the total ice development potential compared with that of the base flow scenario. The influence of the intake depth was analyzed as the difference in total ice development potential between the original and Deepwater intake simulations for each of the discharge scenarios. The same pattern of ice development emerges across the various discharge scenarios for the Deepwater and original simulations. The least development occurs for the Dynamic 2006 scenario, followed by the Base2010, and finally the FullSpring and FullSummer. For all of the discharge scenarios, the total ice development potential drops for the Deepwater intake simulations, with the greatest change (-0.5 days) occurring for the Base2010 discharge scenario. This decrease in potential ice formation reflects the increased temperature of the upstream boundary condition for the winter time. Because Bratsberg is simulated to draw water from the hypolimnion of Selbusjøen in the Deepwater simulations, this water is significantly warmer in the winter than that which was observed to actually occur in the winter of 2010 when water was drawn from within the top few meters of the reservoir. The Dynamic2006 scenario introduces more warm hypolimnion water than the other discharge scenarios, leading to the least ice formation potential. The Base2010 discharge scenario sees the greatest decrease in ice formation potential from the original scenarios as discharge through Bratsberg during the ice formation period is highest for the Base2010 discharge scenario.

Table 3.9: Ice formation potential under Deepwater intake scenario.

Event	Base2010	FullSpring and FullSummer	Dynamic2006	
Count [num.]	9	21	10	
Latest Event	4 Jan.	4 Jan.	29 Dec.	
Duration	Min. [hrs]	0.25	1	1.5
	Max. [hrs]	86	103	18
	Mean [hrs]	14	11	6
	Median [hrs]	3	5	4
Sum [days]	5.3	9.9	2.4	
Deviation	From Base2010 [days]	-	+4.4	-2.9
	From Original [days]	-0.5	-0.4	-0.2

CHAPTER 4

CONCLUSION

4.1 Observations of Hydropeaking and Thermopeakings

In the river Nidelva, anthropogenic hydropeaking with accompanying thermopeakings responses were observed for the water year 2010. Hydropeaking was defined as a change of $20 \text{ m}^3/\text{sec}$ or more over one hour for this system to separate the anthropogenic and natural signals. The average hydropeaking event magnitude at Rathe $34 \text{ m}^3/\text{sec}$ (st. dev $17 \text{ m}^3/\text{sec}$), and the average rate of change of $28 \text{ m}^3/\text{sec}/\text{hr}$ (st.dev $8 \text{ m}^3/\text{sec}/\text{hr}$). All but two hydropeaking events were a result of load balancing being through the Bratsberg powerstation, with the two outliers being associated with an emptying of the intake ponds in the Leirfoss complex in response to snow-melt in May and heavy precipitation in August. Discharge was seen to vary in coincidence with fluctuations in market price of electricity, on seasonal, daily, and sub-daily time scales.

Thermopeakings in the study reach had a distinctly seasonal trend, warming with increased discharge in the winter, and cooling with increased discharge in the summer. The transition between seasonal regimes occurred in March and September, while the maximum thermopeakings responses were observed in November and June. The intake geometry of the Bratsberg powerstation buffered the receiving reach from the full magnitude of conventional thermal pollution by taking water from the epilimnion, and the difference in heat fluxes between the bypass tunneled pathway are indicated as the cause of thermopeakings in this system.

4.2 Modeling Thermopeakings

One of the tasks presented in this work is to model thermopeakings events in an arctic setting with limited data. Simple river geometry, regional meteorological data, and hourly discharge data were used to simulate heat fluxes into and out of a 10 kilometer long river reach.

While there are assumptions inherent in the simplified nature of the modeling approach, these simplifications allow the modeling approach to be applied to a wide range of rivers with limited data collection. The verification process, conducted on a period with different climatic conditions than the calibration process, demonstrates that successful calibration of the thermodynamic processes is possible with less than a full year of data. The transport of thermopeaks was seen to be conservative, with minimal longitudinal dispersion, leaving the routing to be described as advective, reactive transport.

4.3 Influence of Discharge Scenarios

The proposed discharge scenarios redistributed the accumulation of heat in the River Nidelva, but had little effect on the total heat accumulation which varied by less than 80 degree days (3 %) from the base discharge scenario observed to occur in 2010 (Figure 3-25). These impacts on pre-parr salmon development and ice formation potential are described below.

4.3.1 Potential Biological Impacts

The impact of the proposed discharge scenarios on the schedule of salmon egg and alevin development was minimal, with a maximum deviation in hatching date of modeled with the four days, and a maximum deviation in swim-up date of five days. These deviations are within natural variability, suggested by Danie et al. (1984) to be around two weeks. This thesis work illuminates that there may be little change in the development rates of salmon eggs and alevin, but their survival is dependent emerging into an ecosystem that is suitable for their further development. With the development schedule predicting that alevin would in the beginning of July, this would have them emerging into high discharge under the FullSummer, and low discharge conditions under the FullSpring scenarios. Under the first condition, there is danger that alevin will swim-up into a current that is too strong for them to have access to the reaches of the river that they need for successful development. Young fry may not be able to navigate the strong current, and risk being washed downstream. In the second scenario, the high discharge prior to alevin swim-up may lead to benthic

and planktonic drift, leaving the river bare when salmon fry emerge in search of food. Concurrently, low discharge levels could leave fry more vulnerable to predation. Total ecosystem impacts should be considered when deciding on the environmental consequences of discharge regimes.

4.3.2 Potential Ice Formation Impacts

Estimated ice production potential varied by 7.7 days under the proposed future scenarios. FullSpring and FullSummer discharge scenarios allow flow to remain very low in Nidelva during the winter months providing opportunity for the river temperature to drop when exposed to winter conditions. The Dynamic2006 scenario kept the river from reaching freezing conditions by periodically introducing high discharge between mid December and late February. These releases were not possible under the observed condition as reservoir levels were too low to permit full scale production (Figure 1-2). The FullSpring and FullSummer scenarios would have the same difficulty as they aim to empty reservoirs during the spring and summer months and would be empty by ice forming season. With this analysis, the Dynamic 2006 scenario appears to lead to the least potential for ice formation.

4.4 Influence of Intake Depth

The elevation of Bratsberg's intake provides a buffer for the Nidelva from thermopeaking. Systems with deepwater intakes are known to produce thermopeaks with larger magnitudes than were observed in Nidelva. Because deepwater intakes are also found in the Norwegian hydropower network, the Nidelva system was modeled with a simulation of a deepwater intake in Selbusjøen and the impacts on the pre-fry salmon development schedule and ice formation potential were estimated. In a comparison of Base2010 discharge scenarios, the total collection of heat in Nidelva dropped by less than 10% under the Deepwater intake scheme. However, the schedule of heat collection was significantly modified with excess degree day accumulation in the winter and spring, and deficient degree day accumulation in the summer and fall (Figure 3-28).

The various future discharge scenarios were analyzed within the Deepwater intake scheme.

The range of annual heat accumulation rose substantially to 521 degree days between the three discharge scenarios. The FullSummer scenario has the largest deviation under the Deepwater intake scheme, with 450 fewer degree days than was simulated for the Base2010 discharge scenario while the Dynamic2006 and FullSpring discharge scenarios produced 71 and 50 excess degree days, respectively. The alteration in total heat accumulation for the FullSpring scenario switched from negative to positive, while the other two discharge scenarios only increased in the magnitude of alterations. Accumulated heat for the FullSpring scenario under the Deepwater intake scheme begins to rise at the beginning of April as the discharge through Bratsberg is ramped up. The temperatures in Selbsjøen's epilimnion and hypolimnion begin to equilibrate in June and July, just as production through Bratsberg is reduced. This leaves low flows in Nidelva susceptible to warming in the summer months.

4.4.1 Deepwater: Potential Biological Impacts

The alteration in the schedule of heat accumulation in Nidelva had a more significant impact on the development schedule of pre-fry salmon than under the observed conditions. Under the Deepwater intake scheme, hatching was simulated to occur 33 days earlier than was modeled for the discharges, meteorologic conditions, and intake structure present in 2010. The alevin development process was accelerated, and swimup was modeled to occur 13 days earlier than under the original simulation.

Changes in discharge were more influential in pre-fry salmon development under the Deepwater scheme than the original simulations. Seasonal shifts in production, modeled with the FullSpring and FullSummer scenarios, had the most dramatic impact on the schedule of salmon development schedules with swimup dates delayed by 16 and 22 days respectively. Egg development was delayed by 17 days under the Dynamic2006 discharge scenario, but alevin development was accelerated, producing a swim-up date only two days after that simulated for the Base2010 discharge scenario. This indicates that the schedule of salmon development in systems with deep intakes may be more susceptible to seasonal shifts in discharge than to short term peaks distributed throughout the year.

4.4.2 Deepwater: Potential Ice Development

Ice formation potential under the Deepwater intake scenario was lower for all discharge scenarios, reflecting the elevated temperature of water discharged through Bratsberg for the winter months. The same pattern of total ice formation potential presented itself as in the original simulations, with Dynamic2006 having the least ice formation potential, followed by Base2010 and the FullSpring and FullSummer scenarios.

4.5 Recommendations

This work has demonstrated that the reservoir fed hydropower facilities in Norway are subject to alterations in river temperature regimes under the development and integration of large-scale wind power into the energy grid. Systems with deepwater intakes are more susceptible to thermopeaking events and seasonal shifts than systems with intakes located in the epilimnion. This difference in construction style could be exploited to negate the severity of thermopeaking events.

For both epilimnion and hypolimnion fed hydropower facilities, seasonal discharge strategies (FullSpring and FullSummer) produce the greatest likelihood of ice production and present the greatest challenges to ecosystems for juvenile fish to emerge into. The dynamic response strategy reduces the risk of ice production, and has the least impact on the schedule of pre-parr salmon development for systems with deepwater intakes. The alterations in fish development schedules are within natural ranges for all three scenarios for an epilimnion fed system. These insights lead the dynamic response strategy to be identified as the discharge strategy that will produce the least biological disturbance within the parameters investigated in this thesis work, while also minimizing the potential for ice formation.

Thermopeaks rates are driven by the ramping rate used to raise and lower water levels in response to the price of electricity. These rates, as well as thermopeaking magnitudes, were observed and modeled to attenuate during transport. When physiologically significant thermopeaking characteristics are developed for key species in the receiving reach, it will be important to evaluate ramping rates of peaking operations. The HEC-RAS model has demonstrated its utility in modeling the longitudinal attenuation of thermopeaking,

and given physiologically important thermopeaking rate and magnitude thresholds, this approach could be used to determine the areal extent of impacted areas downstream of outlets from hydropeaking hydropower plants.

LIST OF REFERENCES

- Aas, Ø., Einum, S., Klemetsen, A., Skurdal, J., 2010. Atlantic Salmon Ecology. Atlantic Salmon Ecology. Wiley-Blackwell.
- Anagnostopoulos, J.S., Papantonis, D.E., 2007. Pumping station design for a pumped-storage wind-hydro power plant. *Energy Conversion and Management* 48 (11), 3009–3017.
- Armstrong, J.D., Kemp, P.S., Kennedy, G.J.A., Ladle, M., Milner, N.J., 2003. Habitat requirements of Atlantic salmon and brown trout in rivers and streams. *Fisheries Research* 62 (2), 143–170.
- Berland, G., Nickelsen, T., Heggenes, J., Okland, F., Thorstad, E.B., Halleraker, J., 2004. Movements of wild Atlantic salmon parr in relation to peaking flows below a hydropower station. *River Research and Applications* 20 (8), 957–966.
- Borsanyi, P., 1998. Physical habitat modeling in nidelva, norway. Tech. rep., Institutt for vassbygging.
- Bradford, M.J., 1997. An experimental study of stranding of juvenile salmonids on gravel bars and in sidechannels during rapid flow decreases. *Regulated Rivers: Research and Management* 13 (5), 395–401.
- Brunner, G.W., 2002. Theoretical basis for one-dimensional flow calculations. In HEC-RAS. River Analysis System Hydraulic Reference Manual. US Army Corps of Engineers Hydrologic Engineering Center, Davis. CA.
- Brunner, G.W., 2010. HEC-RAS River Analysis System User's Manual Version 4.1. US Army Corps of Engineers Institute for Water Resources Hydrologic Engineering Center, Davis, CA.
- Bruno, M.C., Siviglia, A., Carolli, M., Maiolini, B., 2012. Multiple drift responses of benthic invertebrates to interacting hydropeaking and thermopeaking waves. *Ecohydrology* .
- Bunt, C.M., Cooke, S.J., Katopodis, C., McKinley, R.S., 1999. Movement and summer habitat of brown trout (*Salmo trutta*) below a pulsed discharge hydroelectric generating station. *Regulated Rivers: Research and Management* 15 (5), 395–403.
- Caissie, D., 2006. The thermal regime of rivers: a review. *Freshwater Biology* 51 (8), 1389–1406.
- Carolli, M., Bruno, M.C., Siviglia, A., Maiolini, B., 2012. Responses of benthic invertebrates to abrupt changes of temperature in flume simulations. *River Research and Applications* 28 (6), 678–691.
- Carpenter, S.R., Fisher, S.G., Grimm, N.B., Kitchell, J.F., 1992. Global change and freshwater ecosystems. *Annual Review of Ecology and Systematics* 23, 119–139.

- Casas-Mulet, R., Alfredsen, K., Ruther, N., Killingveit, A., Bakken, T.H., 2010. Methodologies to predict stranding potential during hydropeaking operations. Tech. rep., Institut for vann og-miljøteknikk, NTNU.
- Coutant, C.C., 1999. Perspective on temperature in the Pacific Northwest's fresh water. Tech. rep., Environmental Sciences Division, Oak Ridge National Laboratory.
- Crisp, D.T., 1981. A desk study of the relationship between temperature and hatching time for the eggs of five species of salmonid fishes. *Freshwater Biology* 11 (4), 361–368.
- Crisp, D.T., 1988. Prediction, from temperature, of eyeing, hatching and swim-up times for salmonid embryos. *Freshwater Biology* 19 (1), 41–48.
- Cristina Bruno, M., Maiolini, B., Carolli, M., Silveri, L., 2010. Short time-scale impacts of hydropeaking on benthic invertebrates in an alpine stream (Trentino, Italy). *Limnologica - Ecology and Management of Inland Waters* 40 (4), 281–290.
- Cushman, R.M., 1985. Review of ecological effects of rapidly varying flows downstream from hydroelectric facilities. *North American Journal of Fisheries Management* 5 (3A), 9.
- Daly, S.F., 1991. Frazil ice blockage of intake trash racks. Tech. rep., Cold Regions Research and Engineering Laboratory.
- Danie, D., Trial, J., Stanley, J., 1984. Species profiles: Life histories and environmental requirements of coastal fish and invertebrates(North Atlantic) – Atlantic salmon. Tech. rep., U.S. Army Corps of Engineers.
- Deas, M., 2000. Water Temperature Modeling Review: Central Valley. California Water Modeling Forum.
- Drake, J., Bradford, A., Joy, D., 2010. Application of HEC-RAS 4.0 temperature model to estimate groundwater contributions to Swan Creek, Ontario, Canada. *Journal of Hydrology* 389 (34), 390–398.
- Engbrethsen, T., 2010. Melding om oppstart av planleggingsarbeidet for nye svean kraftverk. Tech. rep., Statkraft.
- Fremstad, E., Thingstad, P., 2007. Nidelva, Trondheims hjerte. Tech. rep., NTNU Vitenskapsmuseet: Seksjon for naturhistorie.
- Frutiger, A., 2004. Ecological impacts of hydroelectric power production on the river Ticino. part 1: Thermal effects. *Archiv fr Hydrobiologie - Hauptbnde* 159 (1), 43–56.
- Hannah, D.M., Webb, B.W., Nobilis, F., 2008. River and stream temperature: dynamics, processes, models and implications. *Hydrological Processes* 22 (7), 899–901.
- Higgins, P. S., M.J.B., 1996. Evaluation of a large-scale fish salvage to reduce the impacts of controlled flow reduction in a regulated river. *North American Journal of Fisheries Management* 16 (3), 7.
- Holland, S.P., Mansur, E.T., 2008. Is real-time pricing green? the environmental impacts of electricity demand variance. *Review of Economics and Statistics* 90 (3), 550–561.

- Hunter, M.A., 1992. Hydropower flow fluctuations and salmonids: A review of the biological effects, mechanical causes, and options for mitigation. Tech. rep., State of Washington Department of Fisheries: Habitat Management Division.
- Hvidsten, N.A., 1985. Mortality of pre-smolt Atlantic salmon, *Salmo salar* L., and brown trout, *Salmo trutta* L., caused by fluctuating water levels in the regulated river Nidelva, central Norway. *Journal of Fish Biology* 27 (6), 711–718.
- Jan De Decker, P.K., 2011. Offshore electricity grid infrastructure in Europe: A techno-economic assessment. Tech. rep., 3E, Wenergy Econnect, SINTEF, dena, ForWind, IEO, NTUA.
- Jensen, M.C.L., 2004. Temperature modeling with HEC-RAS. Tech. rep., ASCE.
- Johnsen, B.O., Arnekleiv, J.V., Asplin, L., Barlaup, B.T., Næsje, T.F., Rossleland, B.O., Saltveit, S.J., 2010. Effekter av Vassdrags-Regulering på Villaks. Kunnskapscenter for Laks og Vannmiljø.
- Killingtveit, A., 2012. Omlegging til fornybar energi i Europa - Hvordan kan Norge bidra? Presentation, Norwegian University of Science and Technology.
- Leonhard, W., Grobe, E.M., 2004. Sustainable electrical energy supply with wind and pumped storage - a realistic long-term strategy or utopia? In *Power Engineering Society General Meeting, 2004. IEEE, 1221–1225 Vol.2*.
- Locher, H., 2004. Environmental issues and management for hydropower peaking operations. Tech. rep., United Nations Department of Economic and Social Affairs: Division for Sustainable Development.
- McCullough, D., 1999. A review and synthesis of effects of alterations to the water temperature regime on freshwater life stages of salmonids, with special reference to Chinook salmon. Review, U.S. Environmental Protection Agency.
- Neuheimer, A. B., T.C.T., 2007. The growing degree-day and fish size-at-age: the overlooked metric. *Canadian Journal of Fisheries and Aquatic Sciences* 64 (2), 375–385.
- Olden, J.D., Naiman, R.J., 2010. Incorporating thermal regimes into environmental flows assessments: modifying dam operations to restore freshwater ecosystem integrity. *Freshwater Biology* 55 (1), 86–107.
- Petts, G.E., Gurnell, A.M., 2005. Dams and geomorphology: Research progress and future directions. *Geomorphology* 71 (12), 27–47.
- Ramos, H., Borga, A., 1999. Pumps as turbines: an unconventional solution to energy production. *Urban Water* 1 (3), 261–263.
- Randle, T.J., Samad, M.A., 2008. Platte River in central Nebraska modeling of pulse-flow release. Tech. rep., U.S. Department of the Interior Bureau of Reclamation.
- Richmond, M.C., Perkins, W.A., 2009. Efficient calculation of dewatered and entrapped areas using hydrodynamic modeling and GIS. *Environmental Modelling and Software* 24 (12), 1447–1456.

- Ryan, P., 1968. Thermal Stratification and Overturn in Lakes and Reservoirs. University of Melbourne.
- Schlosser, I.J., Johnson, J.D., Knotek, W.L., Lapinska, M., 2000. Climate variability and size-structured interactions among juvenile fish along a lake-stream gradient. *Ecology* 81 (4), 1046–1057.
- Scruton, D., Pennell, C., Ollerhead, L., Alfredsen, K., Stickler, M., Harby, A., Robertson, M., Clarke, K., LeDrew, L., 2008. A synopsis of hydropeaking studies on the response of juvenile Atlantic salmon to experimental flow alteration. *Hydrobiologia* 609 (1), 263–275.
- Sherman, B., 2000. Scoping options for mitigating cold water discharges from dams. Tech. rep., CSIRO, Agriculture, Fisheries and Forestry - Australia, NSW, Fisheries, CRC for Freshwater Ecology, and NSW.
- Sherman, B., Todd, C.R., Koehn, J.D., Ryan, T., 2007. Modelling the impact and potential mitigation of cold water pollution on murray cod populations downstream of Hume Dam, Australia. *River Research and Applications* 23 (4), 377–389.
- Siviglia, A., Toro, E., 2009. WAF method and splitting procedure for simulating hydro- and thermal-peaking waves in open-channel flows. *Journal of Hydraulic Engineering* 135 (8), 651–662.
- Song, C.R., Voyiadjis, G.Z., Tumay, M.T., Abousleiman, Y., Bai, M., Cheng, A.H.D., Zaman, M., 1999. Determination of permeability of soils using the multiple piezo-element penetrometer. *International Journal for Numerical and Analytical Methods in Geomechanics* 23 (13), 1609–1629.
- Steel, E.A., Lange, I.A., 2007. Using wavelet analysis to detect changes in water temperature regimes at multiple scales: effects of multi-purpose dams in the Willamette River basin. *River Research and Applications* 23 (4), 351–359.
- Sundt, H., 1984. Modeller for simulering av miljøkonsekvenser av vannkraft. Tech. rep., NTNU, LFI, NIVA.
- Taner, M.U., Carleton, J.N., Wellman, M., 2011. Integrated model projections of climate change impacts on a North American lake. *Ecological Modelling* 222 (18), 3380–3393.
- Toffolon, M., Siviglia, A., Zolezzi, G., 2010. Thermal wave dynamics in rivers affected by hydropeaking. *Water Resour. Res.* 46 (8).
- Valentin, S., Lauters, F., Sabaton, C., Breil, P., Souchon, Y., 1996. Modelling temporal variations of physical habitat for brown trout (*Salmo trutta*) in hydropeaking conditions. *Regulated Rivers: Research and Management* 12 (2-3), 317–330.
- Vehanen, T., Bjerke, P.L., Heggenes, J., Huusko, A., Mäki-Petäys, A., 2000. Effect of fluctuating flow and temperature on cover type selection and behaviour by juvenile brown trout in artificial flumes. *Journal of Fish Biology* 56 (4), 923–937.
- VEMCO, 2011. Minilog-ii-T Datasheet 4769-04, 1.
- Vinson, M.R., 2001. Long-term dynamics of an invertebrate assemblage downstream from a large dam. *Ecological Applications* 11 (3), 711–730.

- Ward, J.V., Stanford, J.A., 1979. Ecological factors controlling stream zoobenthos with emphasis on thermal modification of regulated streams. In *The ecology of regulated streams : [proceedings of the first International Symposium on Regulated Streams held in Erie, Pa., April 18-20, 1979]*, xi, 398 p. Plenum Press, New York.
- Webb, B.W., Hannah, D.M., Moore, R.D., Brown, L.E., Nobilis, F., 2008. Recent advances in stream and river temperature research. *Hydrological Processes* 22 (7), 902–918.
- Winther, T.U., Olafsen, K.T., 2007. Akvakultur av torsk i Trondheimsfjorden - Konsekvensutredning. Tech. rep., SINTEF Fiskeri og havbruk AS.
- Zolezzi, G., Siviglia, A., Toffolon, M., Maiolini, B., 2011. Thermopeaking in alpine streams: event characterization and time scales. *Ecohydrology* 4 (4), 564–576.

CHAPTER A

APPENDIX

A.1 Heat Flux Equations: Adapted from Brunner (2010)

A.1.1 Solar Radiation

$$q_{sw} = q_o a_t (1 - R_\omega) (1 - 0.65 Cl^2) \quad (\text{A.1})$$

$$q_o = \frac{Q_o}{r^2} (\sin\theta \sin\delta_l + \cos\theta \cos\delta_l \cosh) \quad (\text{A.2})$$

θ = Latitude [rad]

δ_l = Declination [rad]

h = Local hour angle [rad]

Q_o = Solar constant: 1360 [W m⁻²]

r = Radius vector [unitless]

a_t = Atmospheric attenuation

Function of: cloudiness, elevation, air temperature, vapor pressure, dust coefficient.

R_ω = Reflectivity of the water surface

Computed as function of solar altitude and cloud cover.

Cl = Percent sky covered with clouds

A.1.2 Atmospheric Longwave Radiation

$$q_{atm} = \epsilon_a \sigma T_{ak}^4 \quad (\text{A.3})$$

ϵ_a = Emissivity of air [unitless]

Computed as function of air temperature and cloudiness.

σ = Stefan Boltzman Constant: 5.6704×10^{-8} [W m⁻²K⁻⁴]

T_{ak} = Air temperature [K]

A.1.3 Back Longwave Radiation

$$q_b = \epsilon_w \sigma T_{wk}^4 \quad (\text{A.4})$$

ϵ_w	=	Emissivity of water	[0.97]
σ	=	Stefan Boltzman Constant: 5.6704×10^{-8}	[W m ⁻² K ⁻⁴]
T_{wk}	=	Water temperature	[K]

A.1.4 Sensible Heat

$$q_h = \left(\frac{K_h}{K_w} \right) C_p \rho_w (T_a - T_w) f(U) \quad (\text{A.5})$$

C_p	=	Specific heat of air	[J kg ⁻¹ C ⁻¹]
T_a	=	Air temperature	[C]
T_w	=	Water surface temperature	[C]
$f(U)$	=	Wind function	[m s ⁻¹]
K_h/K_w	=	Diffusivity ratio	[unitless]

The diffusivity ratio is a parameter that allows the user to partition flux between latent and sensible heat. It is generally set to unity but is allowed by the software to range between 0.5 and 1.5. A range between 0.9 and 1.1 is recommended.

A.1.5 Latent Heat

$$q_l = \frac{0.622}{P} L_{vap} \rho_w (e_s - e_a) f(U) \quad (\text{A.6})$$

P	=	Atmospheric pressure	[mb]
L_{vap}	=	Latent heat of vaporization	[J kg ⁻¹]
Computed as a function of water temperature.			
ρ_w	=	Density of water	[kg m ⁻³]
e_s	=	Saturated vapor pressure as water temperature	[mb]
e_a	=	Vapor pressure of overlying air	[mb]
$f(U)$	=	Wind function	[m s ⁻¹]

A.1.6 Wind Function

The wind function is defined as:

$$f(U) = R_m (a + bU^c) \quad (\text{A.7})$$

with user specified calibration coefficients on the order of:

$$a = 10^{-6}$$

$$b = 10^{-6}$$

$$c = 1$$

$$R_m = 1$$

a, b, and c are calibration parameters that are held constant through the simulation, while R_m (the so called Richardson multiplier) is allowed to fluctuate between 0.03 and 12.3. The value of the Richardson multiplier is based on the computed value of the Richardson number R_i which is found for each time step with the following equation:

$$R_i = \frac{g(\rho_{air} - \rho_{sat})z}{\rho_{air}u_a^2} \quad (\text{A.8})$$

g	=	ravitational constant	[9.81 m/s ²]
ρ_{air}	=	Density of moist air	[kg/m ³]
ρ_{sat}	=	Density of saturated air	[kg/m ³]
z	=	Elevation of recording station	[m]
u_a	=	Wind speed	[m/s]

The Richardson multiplier (R_m) is calculated from the Richardson number (R_i) with a series of stepwise functions based on atmospheric conditions.

For unstable atmospheric conditions with $\rho_{air} > \rho_{sat}$:

$$R_m = 12.3 \quad \text{For } -1 \geq R_i$$

$$R_m = (1-22R_i)^{0.8} \quad \text{For } -0.01 \geq R_i \geq -1$$

For neutral atmospheric conditions with $\rho_{air} = \rho_{sat}$:

$$R_m = 1 \quad \text{For } -0.01 \geq R_i \geq 0.01$$

For stable atmospheric conditions with $\rho_{air} < \rho_{sat}$:

$$R_m = (1-34R_i)^{-0.8} \quad \text{For } 0.01 \leq R_i \leq 2$$

$$R_m = 0.03 \quad \text{For } 2 \leq R_i$$

A.2 Representative Heat Fluxes

The heat flux for upstream boundary during the 2010 water year is broken down into its respective components in the Figure A-1. Longwave radiation was calculated as the sum of atmospheric (downwelling) and back (upwelling) radiation. The daily net heat flux values were computed as a moving average.

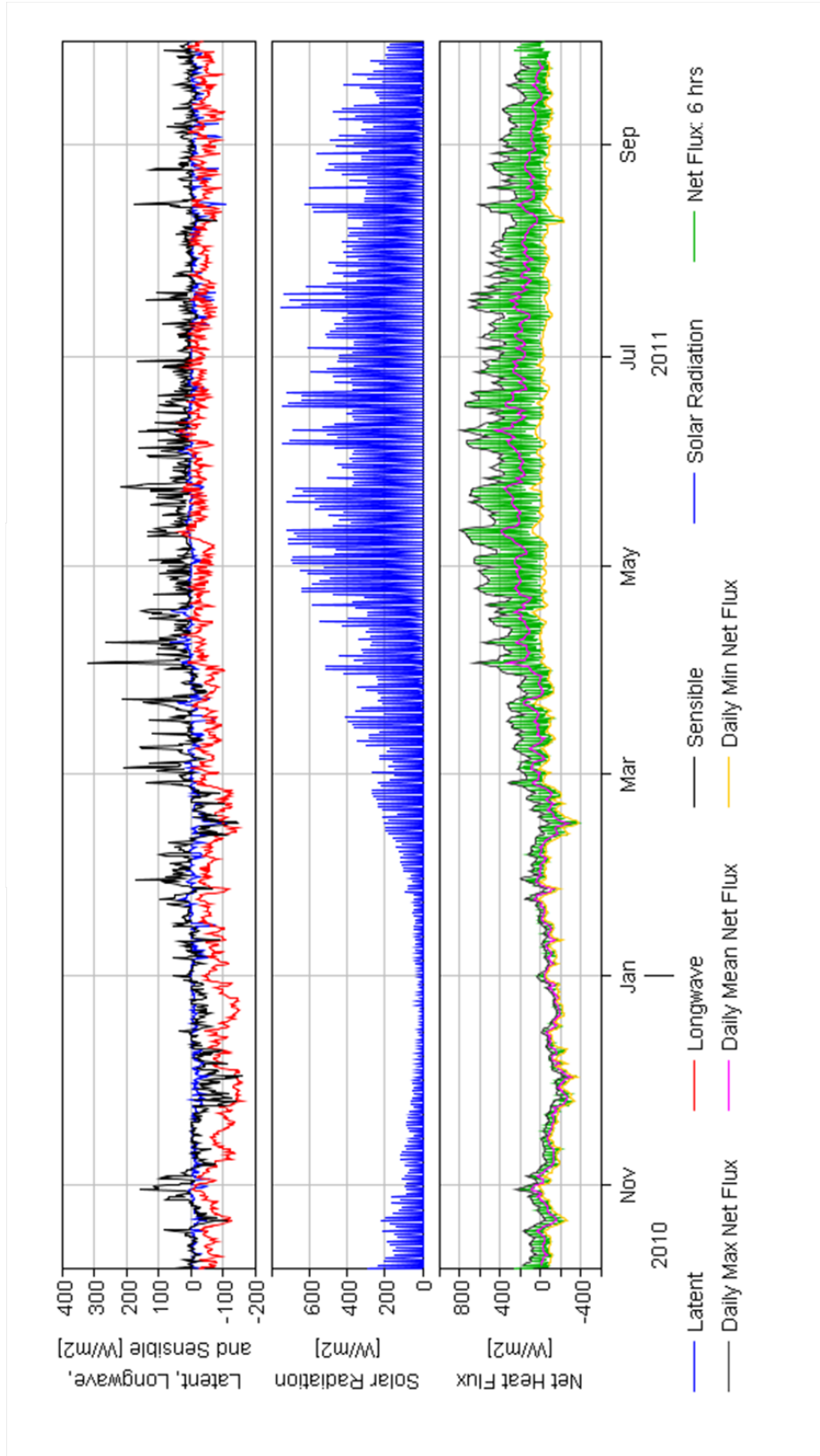


Figure A-1: Heat fluxes across the air-water interface for 2010 using the basecase discharge scenario.

A.3 Observed Meteorologic Parameters

The durations of the six driving meteorologic conditions used in the water quality component of the HEC-RAS model are shown in the Figure A-2. Duration analysis was performed for reported values from October 2010 to October 2011. Monthly minimum, mean, and maximum values were compared with six years of observations form 2005 through 2011. The results are displayed in Figure A-3 where the monthly minimum, mean, and maximum observed values are shown as solid blue, green, and red lines. The minimum, mean, and maximum average values over the six year comparison period are shown as dashed black lines with one standard deviation above and below these values represented with solid light grey lines.

A.4 Cross Sections

All 58 measured cross sections are presented in Figure A-4. Note that the horizontal scale is adjusted for the range of each cross section, meaning that scaling varies between images. The cross sections are displayed with wetted areas for a discharge $40 \text{ m}^3/\text{s}$, with water levels for 90 and $140 \text{ m}^3/\text{s}$ shown in red and green lines respectively.

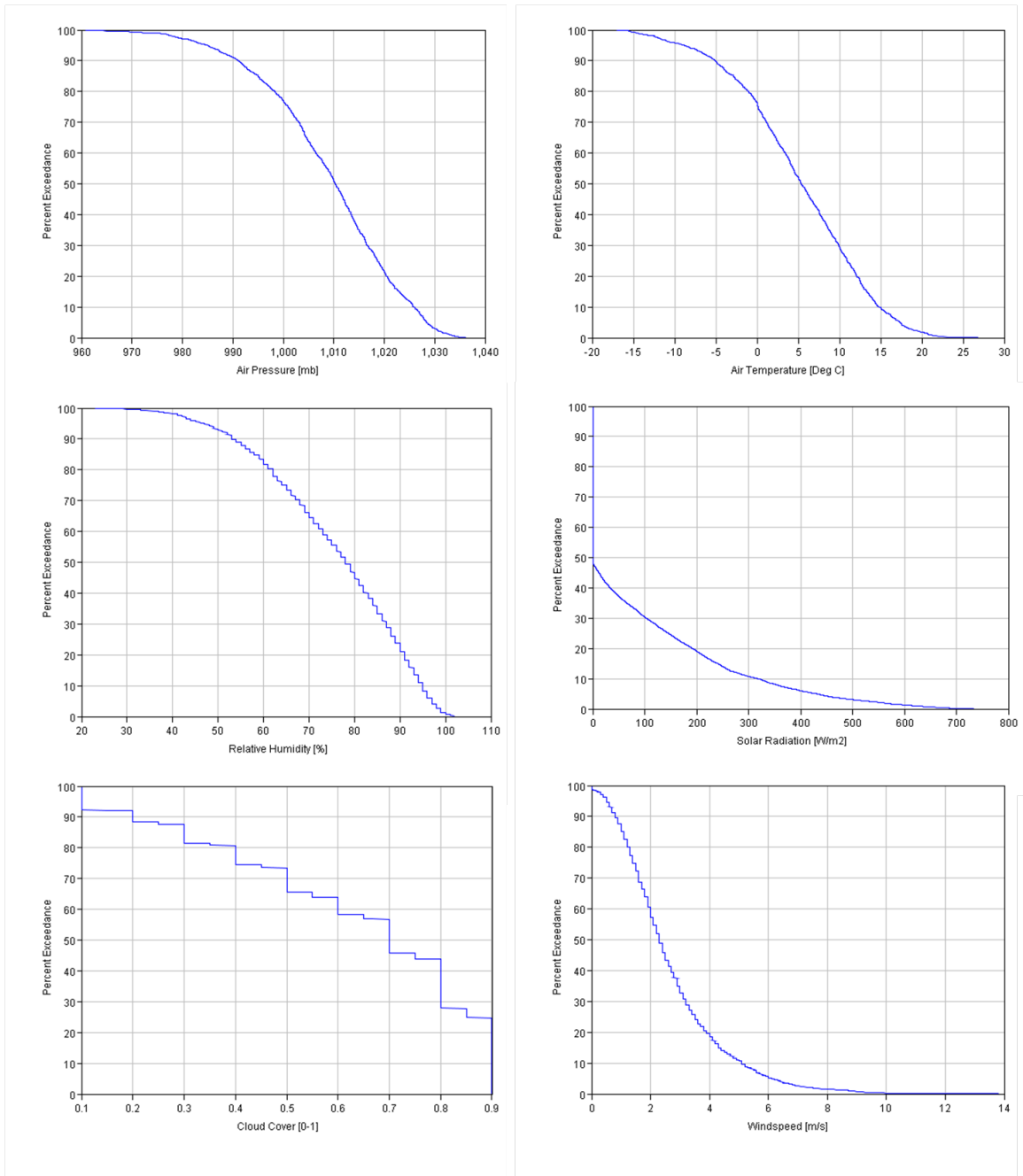
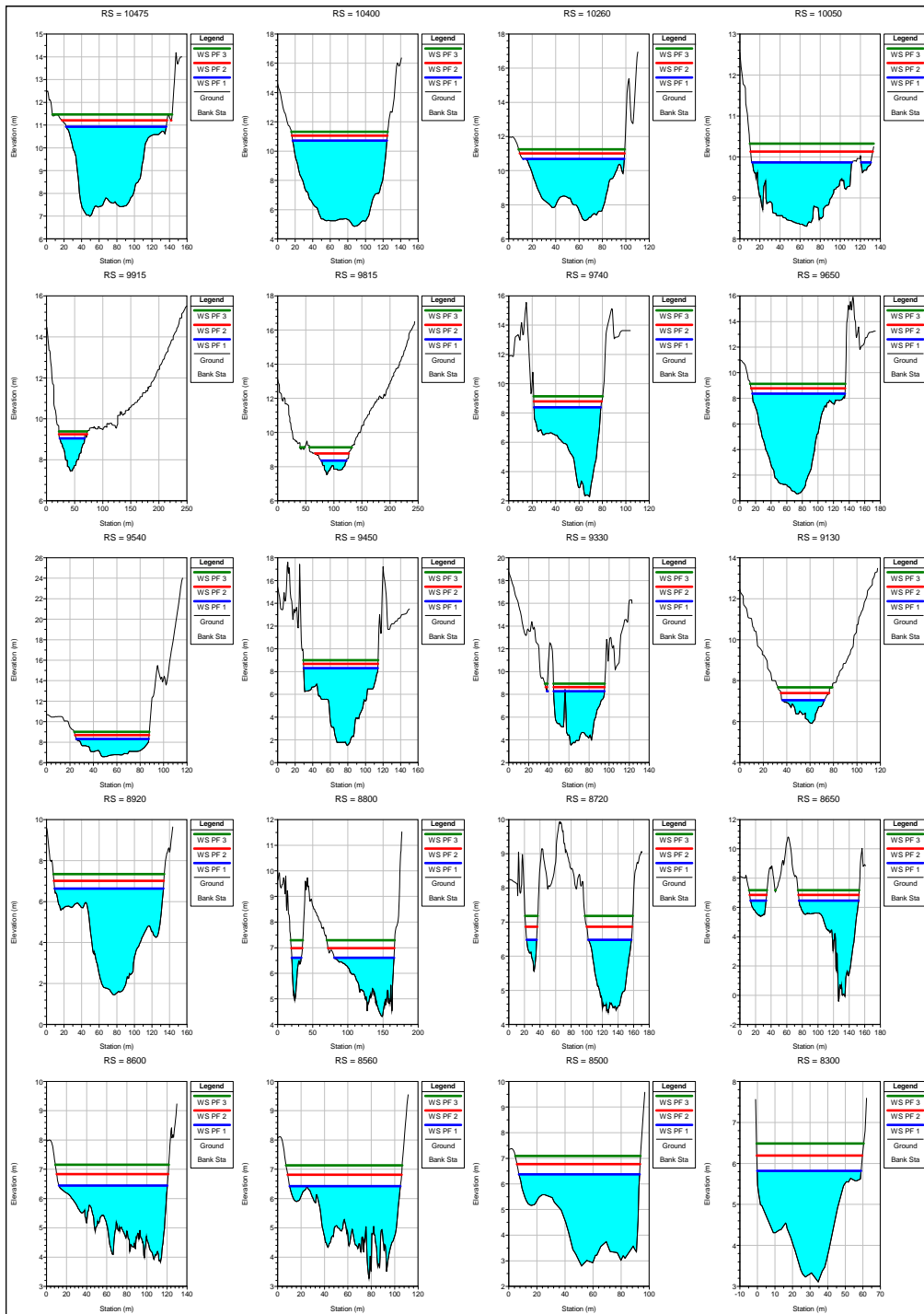
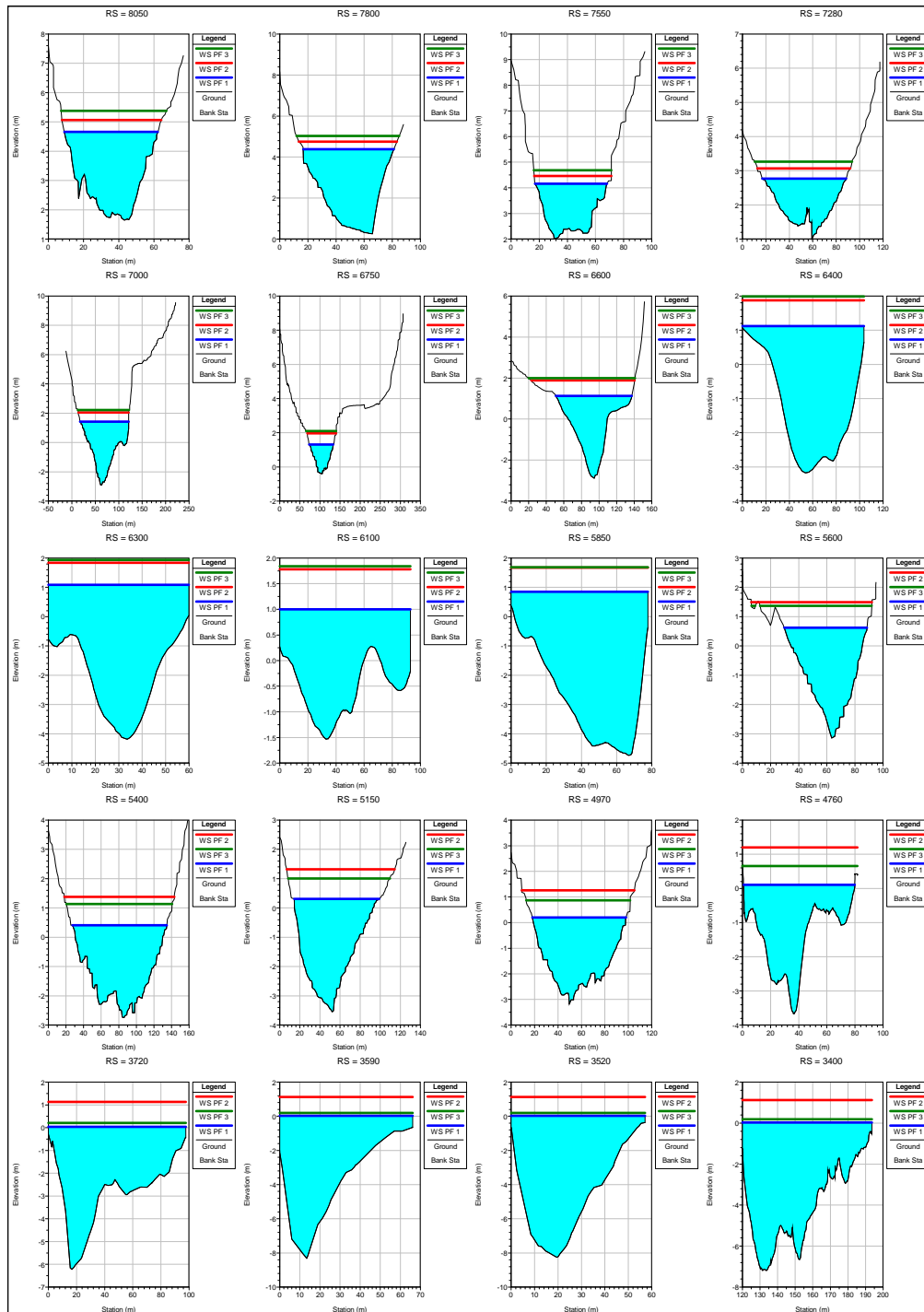


Figure A-2: Duration curves for air pressure (top left), air temperature (top right), relative humidity (middle left), solar radiation (middle right), cloud cover (lower left), and wind speed (lower right).



Figure A-3: Average monthly maximum, mean, and minimum meteorologic values observed in Trondheim for the water years 2005 through 2011.





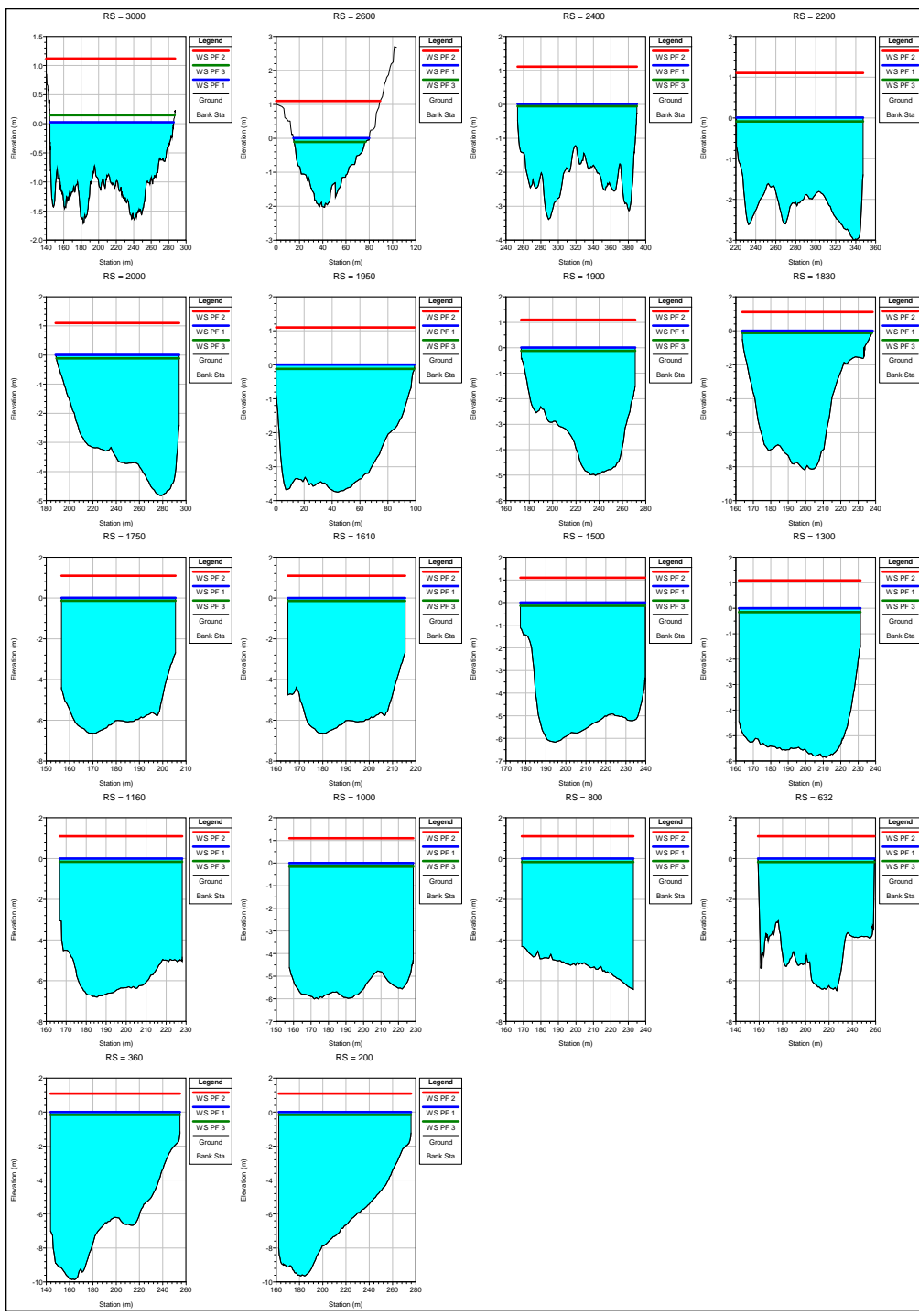


Figure A-4: Cross sections with water levels for 40, 90, and 140 m³/s model runs.